UNIVERSITY OF COPENHAGEN

Optomechanics with soft-clamped silicon nitride membranes and carrier-mediated forces in coupled quantum wells

Ph.D. Thesis

Andreas Barg

Supervisor: Prof. Eugene S. Polzik

This thesis has been submitted to the PhD School of The Faculty of Science, University of Copenhagen.

November 2018

Ph.D. Committee

External:
Prof. Michael R. Vanner (Imperial College London)
Prof. Ivan Favero (Paris Diderot University)

Local:
Prof. Per Hedegård (University of Copenhagen)

Submission date: November 2, 2018
Defense date: December 5, 2018

Abstract

The field of quantum cavity optomechanics is fueled by the development of high-performance micro- and nanofabricated devices. These devices aim to enhance the interaction between optical and mechanical resonators by improving their respective quality factors and exploring new coupling mechanisms. Thanks to recent progress in the field, the dream to efficiently prepare and control quantum states of mechanical motion for quantum information processing is soon to become a reality.

In this thesis, we present ultrahigh-quality-factor silicon nitride membranes with phononic crystal structures for quantum optomechanics. The membranes are periodically patterned, with a defect in the center that hosts localized mechanical modes and enables 'soft clamping': without a rigid silicon frame as a boundary for these modes, the curvature in the membrane remains small during the motion, significantly reducing intrinsic dissipation. Indeed, we measure mechanical quality factors of up to $Q = (214 \pm 2) \times 10^6$ and long coherence times enabling several quantum-coherent oscillations, even at room temperature. This extraordinary performance, alongside their low effective masses of a few nanograms, render our membranes excellent candidates for quantum cavity optomechanics, as well as mass and force sensing applications.

We place a patterned membrane inside a high-finesse optical cavity mounted in a 4-K-liquid-helium cryostat and optically cool a localized defect mode via radiation pressure induced dynamical backaction to the vicinity of the quantum ground state of motion. Raman sideband thermometry reveals the mean phonon occupancy of the mode to be $\bar{n} = 0.55 \pm 0.01$, which is close to the backaction limit. Our setup thereby manifests itself as a quantum-enabled system, allowing for complex protocols such as the heralded generation of one-phonon Fock states by filtering and detecting single scattered photons.

In a parallel line of research, we study carrier-mediated forces in semiconductor nanomembranes. By embedding coupled quantum wells in the membranes, lifetimes of optically generated electron-hole pairs reach up to $\Gamma_\mathrm{I}^{-1} = (749.5 \pm 0.4)\,\mathrm{ns}$, which is comparable to the period of mechanical oscillation. As a result, the strong forces due to the piezoelectric effect and the deformation potential resonantly drive a bending mode of the membrane to an amplitude about three orders of magnitude larger than expected from radiation pressure. The forces are controlled using a bias voltage across the quantum wells that tunes the carrier lifetime. In addition to exploring potentially much more efficient optomechanical coupling mechanisms, this work may provide a new path towards optoelectromechanical hybrid devices.

Sammenfatning

Forskningsfeltet kavitets-kvanteoptomekanik er drevet af udviklingen af højtydende mikro- og nanofabrikerede systemer. Disse systemer sigter mod at forbedre vekselvirkningen mellem optiske og mekaniske resonatorer, ved at forbedre deres respektive kvalitetsfaktorer og udforske nye koblingsmekanismer. På grund af de seneste fremskridt i feltet kan drømmen om at forberede og manipulere mekaniske objekters kvantetilstande til kvanteinformationsbehandling snart blive en realitet.

I denne afhandling præsenterer vi ultrahøj-kvalitetsfaktor siliciumnitrid membraner med fononiske krystalstrukturer til brug i kvanteoptomekanik. Membranerne er periodisk mønstret med en defekt i midten, der har lokaliserede mekaniske tilstande og muliggør 'soft clamping': uden en stiv siliciumramme som rand for disse tilstande, forbliver krumningen i membranen lille under bevægelsen og det reducerer væsentligt indre friktion. Vi måler mekaniske kvalitetsfaktorer på op til $Q = (214 \pm 2) \times 10^6$ og lange kohærenstider, der muliggør adskillige kvantekohærente svingninger, selv ved stuetemperatur. Denne ekstraordinære ydeevne, sammen med deres lave effektive masser på omtrent et par nanogram, gør vores membraner fremragende kandidater til kvanteoptomekanik, samt anvendelser i masse- og kraftsensorer.

Vi placerer en mønstret membran inde i en optisk kavitet med højreflektive spejle, der er placeret i en heliumflow-kryostat, og køler en lokaliseret mekanisk tilstand til i nærheden af kvante-grundtilstanden via lysets strålingstryk. Raman-sidebåndstermometri viser den gennemsnitlige fononokkupans til at være $\bar{n} = 0{,}55 \pm 0{,}01$, hvilket er tæt på kvantetilbagekoblingsgrænsen. Vores opstilling manifesterer sig herved som et kvantesystem, der muliggør komplekse protokoller, såsom generation af en fonontilstand ved at filtrere og detektere enkelte spredte fotoner.

I et separat studie undersøger vi ladningsbærer-medierede kræfter i halvleder-nanomembraner. Ved koblede kvantebrønde i membranerne når levetiderne af optisk genererede elektron-hulpar op til $\Gamma_{\mathrm{I}}^{-1} = (749{,}5 \pm 0{,}4)\,\mathrm{ns}$, der er sammenlignelige med perioden af de mekaniske svingninger. Et resultat heraf er, at de stærke kræfter forårsaget af den piezoelektriske virkning og deformationspotentialet driver bøjningssvingninger af membranen resonant til en amplitude omkring tre størrelsesordener større end forventet fra strålingstrykket. Derudover styres kræfterne ved at anvende en forspænding over kvantebrøndene, hvorved levetiden for ladningsbærerne kan justeres. Udover at udforske potentielt meget mere effektive optomekaniske koblingsmekanismer, kan dette studie vise vejen til nye optoelektromekaniske hybridsystemer.

List of publications

Peer-reviewed papers

[1] A. Barg, Y. Tsaturyan, E. Belhage, W. H. P. Nielsen, C. B. Møller, and A. Schliesser. Measuring and imaging nanomechanical motion with laser light. Applied Physics B, 123, 8 (2016).

[2] T. Capelle, Y. Tsaturyan, A. Barg, and A. Schliesser. Polarimetric analysis of stress anisotropy in nanomechanical silicon nitride resonators. Applied Physics Letters, 110, 181106 (2017).

[3] Y. Tsaturyan, A. Barg, E. S. Polzik, and A. Schliesser. Ultracoherent nanomechanical resonators via soft clamping and dissipation dilution. Nature Nanotechnology, 12, 776–783 (2017).

[4] A. Barg, L. Midolo, G. Kiršanskė, P. Tighineanu, T. Pregnolato, A. İmamoğlu, P. Lodahl, A. Schliesser, S. Stobbe, E. S. Polzik. Carrier-mediated optomechanical forces in semiconductor nanomembranes with coupled quantum wells. Physical Review B, 98, 155316 (2018).

Patent application

[5] A. Schliesser, Y. Tsaturyan, E. S. Polzik, A. Barg. Mechanical resonator device. World Intellectual Property Organization, WO 2018/024713 A1 (2018).

List of abbreviations

AOM	acousto-optic modulator
APD	avalanche photodetector
BS	beam splitter
CQW	coupled quantum well
DBR	distributed Bragg reflector
EHP	electron-hole pair
EOM	electro-optic modulator
ETH	Swiss Federal Institute of Technology
FSR	free spectral range
FWHM	full width at half maximum
GaAs	gallium arsenide
LO	local oscillator
MiM	membrane-in-the-middle
NBI	Niels Bohr Institute
OMIT	optomechanically induced transparency
PBS	polarizing beam splitter
PDH	Pound-Drever-Hall
PL	photoluminescence
PSD	power spectral density
PZT	piezoelectric transducer
Quantop	Danish Center for Quantum Optics
rms	root mean square
SiN	silicon nitride
SLAB	Schliesser Lab
SN	shot noise
SNR	signal-to-noise ratio
TMM	transfer-matrix method

Preface

How does light interact with matter at the most fundamental level? This question is at the heart of quantum optics, a research field which was first motivated more than 100 years ago by the pioneering work of Planck [6] and Einstein [7] about the discovery of quantized light particles, known as photons. Ever since, the field has grown substantially and became part of experimental physics shortly after the advent of the first lasers in the 1960s. Nowadays, researchers are able to control the interplay between light and matter, as evidenced by the development of quantum technologies such as quantum cryptography and quantum computers [8, 9].

My personal journey into the field began six years ago as a master's student at the Danish Center for Quantum Optics (Quantop) at the Niels Bohr Institute (NBI). At that time I was gaining my first hands-on experience in a quantum optics laboratory and soon became fascinated with a subdiscipline called optomechanics. After my master's course I continued as a research assistant to follow through with the sample characterization I had started as part of my master's thesis and expressed my wish to begin a Ph.D. project in the group. In 2015 I was excited to be given this opportunity.

As a Ph.D. student I was involved in three different projects: In the first year, I focused my efforts on carrier-mediated optomechanical forces in nanomembranes with coupled quantum wells, which is presented in Chapter 3 of this thesis. The close collaboration with the Quantum photonics groups at NBI and at the Swiss Federal Institute of Technology (ETH) in Zürich made this a fascinating experience, with which I could broaden my horizon and learn about the rich physics of semiconductors. Combining the knowledge from different research areas proved to be challenging. Yet, our work was concluded in the form of a manuscript that has recently been submitted for publication [4]. During the second year, I contributed to the development of silicon nitride nanomembranes with phononic crystal structures, conducted in the Schliesser Lab (SLAB) here at NBI. Among other things, the project was based on a time-consuming, systematic study of mechanical quality factors, as is summarized in Chapter 1. Our efforts were rewarded with beautiful and convincing results that were later published in a high-impact journal [3]. Finally, my third year was dedicated to cavity optomechanics, more concretely ground-state cooling and Raman sideband thermometry, discussed in Chapter 2. Here I had the chance to work with the previously developed silicon nitride nanomembranes utilizing their remarkable properties. The success of this project was fueled by the years-long experience of our group with experimental cavity optomechanics, in particular with membrane-in-the-middle systems. The setup is currently being

expanded to enable the generation of single mechanical excitations.

This Ph.D. thesis is organized around the three projects mentioned above, each detailed in a somewhat self-contained chapter including a separate introduction and conclusion. I will point out connections between the projects whenever applicable in the text. The focus lies on describing the experiments, developing specific theoretical models and comparing the two. The basic theory used throughout the three chapters is summarized in Appendix A and may be used as a starting point for the unfamiliar reader. The purpose of this thesis is to provide an overview of the different projects closely following our published work.

Before proceeding, I would like to express my deepest gratitude to those who made this work possible and undeniably enjoyable for me: first and foremost, I thank my supervisor Eugene Polzik for giving me the opportunity to contribute to cutting-edge science as a Ph.D. student in his group. He was always supportive, inspiring, professional, and open-minded – an excellent scientific leader who taught me how to become both a better researcher and person. I also appreciate the guidance from Albert Schliesser, whose passion and innovative spirit was critical to this work. I thank Leonardo Midolo for his patience with our lengthy project and his encouragement which helped me immensely. Furthermore, I acknowledge Jürgen Appel, Jörg Müller and Søren Stobbe for always being eager to help and push me into the right directions. Over the years, I spent most of my time with the good people of the 'Dungeon lab', whose friendships I sincerely value. Without their every-day efforts and support, this thesis would not have been possible. I would like to give special thanks to Yeghishe Tsaturyan for fostering team spirit with his enthusiasm, empathy and photoshop artworks; Ivan Galinskiy for always sharing his knowledge and favourite chocolate (Marabou), Rodrigo Thomas for being a real 'bro' with the motivational skills of Shia LaBeouf; Christoffer Møller for his positivity, sick moves and occasional loud clapping to reset all cavity locks; Anders Simonsen for standing up against interferometer misuse; and William Nielsen for the groovy basslines and for teaching me how to become an articulate gentleman. I also thoroughly enjoyed the company of all other present and former Quantop members, who make this one of the best research groups in the world. I am grateful for all the good time spent with the people from SLAB who quickly became part of the family. More thanks go to my helpful office mate Emil Zeuthen; to Gabija Kiršanskė, Petru Tighineanu, and Peter Lodahl from the photonics groups at NBI; as well as Thomas Fink and Ataç İmamoğlu for their warm welcome at ETH. I would like to thank all musicians of 'The Unresolved Sideband' for sharing an incredibly fun hobby. Last but not least, I thank my loving family and friends to whom I dedicate this thesis.

Contents

Chapter 1

Silicon nitride membranes with ultrahigh quality factors

1.1 Introduction

During the past three decades, advances in micro- and nanofabrication have brought on a technological revolution shaping modern-day life and research through miniaturized electronic, mechanical, and optical components. Their broad spectrum of functionality renders these components a vital part of integrated circuits, transducers, and sensors. Remarkably, their size approaches the few-nanometer scale where some of the properties are governed by quantum effects. As a result, studying the quantum behaviour of tiny fabricated devices has become in itself a subject which has most notably lead to considerable progress in the research areas of quantum information processing and quantum metrology.

Among the plethora of different devices, nanomechanical resonators are used in the thriving field of quantum cavity optomechanics [10,11] which focuses on the interaction between electromagnetic radiation and mechanical motion. It is based on the fact that photons reflected from a resonator carry information about the resonator's motional state and moreover exert a radiation pressure force altering its momentum, which can be used to precisely read out and control the motion. As a milestone in the scientific discipline, demonstrated for the first time in [12,13], this control was utilized to optically cool vibrational modes of nanofabricated devices close to the quantum ground state, i.e., the energetically lowest state allowed by the Heisenberg uncertainty principle. Ever since, using the same technique, known as sideband cooling, this goal has been achieved in many different optomechanical systems. Our own implementation is subject of this thesis and presented in Chapter 2.

It is important to note that the radiation pressure force only has a measurable effect if a very large number of photons impinge on the mechanical resonator or if the resonator is particularly susceptible to forces. The small effective masses associated with nanoscale resonators are a key factor in meeting the latter requirement. Another important characteristic is their quality factor, describing the total amount of stored mechanical

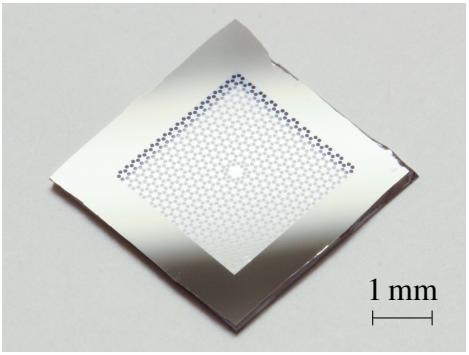

Figure 1.1: Photograph of a SiN membrane with phononic crystal structure. We periodically pattern holes into a stressed SiN film with tens of nanometer thickness, suspended from a rigid silicon frame. The defect in the center of the structure features ultrahigh-Q localized mechanical modes.

energy in relation to dissipated energy. In other words, a resonator with high quality factor can absorb and store much more energy than is dissipated per cycle of oscillation, resulting in a built-up of large mechanical motion as a result of a small force.

There has been great effort to design resonator geometries and find materials, which allow for both low mass and high quality factor; yet the two are difficult to realize simultaneously [14, 15]. One of the most promising platforms to date is based on thin films of silicon nitride (SiN), a material well-known and routinely employed in the world of micro- and nanofabrication. As an essential ingredient the material is highly-stressed during deposition onto the silicon substrate. Once released, the SiN resonator has a higher mechanical eigenfrequency and total stored energy than without the stress, while the energy loss rate is unchanged. This approach is known as dissipation dilution [16] and consistently leads to quality factors of strings [17] and membranes [18] in the millions. At the same time, the sub-micrometer thickness of the SiN films enables small effective masses, even if other dimension are orders of magnitude larger.

The next step towards improved performance of SiN resonators lies in cleverly refining their geometries. Recently, an example of this has been demonstrated in the form of trampoline-shaped SiN membranes [19, 20], in which a central pad is held by thin tethers enduring high levels of stress. Small effective masses of a few nanogram and ultrahigh quality factors as large as $Q \sim 10^8$ of the fundamental mechanical mode for several devices have been reported, as well as Q-frequency products of $Q \times f > 6 \times 10^{12}$ Hz; a requirement for observing a single coherent oscillation within the thermal coherence time (see Appendix A.2.3) at room temperature. A different approach is to engineer a phononic crystal in the silicon frame surrounding the SiN membranes, which suppresses dissipation due to radiation loss, i.e., the tunneling of phonons through the resonator's anchor points into the substrate [21]. This is presented in [22] and our previous work [23], where we found low-order mechanical modes of square SiN membranes with $Q \times f$ similar to those of trampoline resonators.

In our most recent work about nanomechanical resonators [3], conducted in SLAB, we take our approach even further and directly pattern the phononic crystal structure into a SiN membrane (see Figure 1.1). Apart from suppressing phonon-tunneling losses, this

has another dramatic effect; the motion of localized mechanical modes around a defect in the center of the structure evanescently decays into the phononic crystal, reducing internal dissipation through bending motion and exhibiting $Q \times f \approx 10^{14}$ Hz at room temperature. This is more than an order of magnitude larger than we had previously reported.

In this chapter we will discuss these recent findings, focusing primarily on the characterization of our patterned SiN membranes, as well as a theoretical model describing the mechanical dissipation. To start with, in Section 1.2, we will present the experimental tools used to study the membranes and move on to detail the membrane design features in Section 1.3. Next, we will discuss measurements of quality factors and explain their unique scaling in Section 1.4. Finally, in Section 1.5 we will envision applications for our devices and conclude this chapter in Section 1.6. For details about the fabrication process[1] of the device the reader is referred to the methods section of [3].

1.2 Methods of characterization

1.2.1 Michelson interferometer

The first experimental setup used in our lab to characterize SiN membranes is a home-built Michelson interferometer with raster-scan and ringdown functionality. For the description below, we will closely follow our remarks presented in [1, 24].

1.2.1.1 Experimental setup

The optical setup, shown in Figure 1.2, includes a Nd:YAG laser[2] at a wavelength of $\lambda = 1064\,\text{nm}$ from which we derive two beams, i.e., the probe beam and the local oscillator (LO), using a half-wave plate ($\lambda/2$), and a polarizing beam splitter (PBS). The probe beam is guided through a single-mode fiber to the probe head mounted on a 3-axis translation stage with motorized linear actuators. Here the light passes through a quarter-wave plate ($\lambda/4$), a beam splitter (BS), and a microscope objective[3] tightly focusing the light onto the membrane with a spot diameter of $\sim 2\,\mu\text{m}$. To observe at which position the membrane is probed we image it via the objective and a tube lens onto a CMOS camera.

The membrane is placed inside of a liquid-helium flow cryostat[4], maintaining a pressure of $p < 10^{-5}$ mbar to reduce viscous gas damping of the mechanical motion and allowing us to cool the membrane close to the temperature of the cold finger of $T = 4.2\,\text{K}$. As an alternative, we utilize a high vacuum chamber that provides even lower pressures of $p \sim 10^{-7}$ mbar. In each chamber we mount a PZT that can be used to mechanically drive membrane modes (see Section 1.2.1.4).

[1] The device fabrication was carried out by Y. Tsaturyan.
[2] Mephisto Ultra-Narrow Linewidth DPSS Laser from Coherent.
[3] 50X Mitutoyo Plan Apo NIR Infinity Corrected Objective.
[4] Oxford Instruments MICROHR MK2 cryostat.

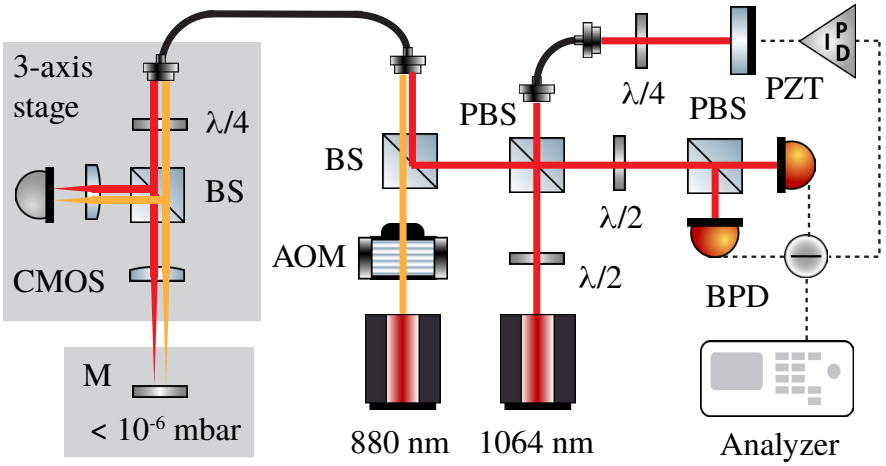

Figure 1.2: Illustration of the interferometer setup. We use a Michelson-interferometer at $\lambda = 1064\,\text{nm}$ with a probe head mounted on a 3-axis translation stage. The reflected light from a membrane (M), placed inside of a vacuum chamber, is detected by a balanced homodyne receiver (BPD) and analyzed. A second laser at $\lambda = 880\,\text{nm}$ is amplitude modulated via an AOM and used to optically excite mechanical motion. The interferometer is stabilized by controlling a mirror on a piezoelectric transducer (PZT) in the reference arm.

The probe beam reflected from the membrane is spatially overlapped with the LO, a bright beam with an optical power of several mW providing a reference with a relative phase $\phi = 4\pi\Delta l/\lambda$, where Δl is the path length difference between the two interferometer arms. Δl can be controlled via a mirror mounted on a PZT in the LO arm. Since the two beams are orthogonally polarized we use a second set of half-wave plate and PBS to enforce interference at the two outputs of the PBS. The outputs are then sent to a balanced photodetector[5] with a bandwidth of 75 MHz.

1.2.1.2 Calibration and sensitivity

Following [25], the difference in photocurrents from the two photodiodes in the balanced photodetector is given by

$$\hat{i}_- = \hat{a}_{\text{LO}}^\dagger \hat{a}_\text{p} + \hat{a}_{\text{LO}} \hat{a}_\text{p}^\dagger, \tag{1.1}$$

where the subscripts of the annihilation and creation operators refer to the LO and the probe beam. We assume the beams to be coherent with real amplitudes α_{LO} and α_p, while allowing for small fluctuations $\delta\hat{a}_\text{p}$ in the probe beam, and transform

$$\hat{a}_{\text{LO}} \rightarrow \alpha_{\text{LO}} e^{i\omega_{\text{LO}} t}, \tag{1.2}$$

$$\hat{a}_\text{p} \rightarrow \left(\alpha_\text{p} + \delta\hat{a}_\text{p}\right) e^{i(\omega_\text{p} t + \phi)}. \tag{1.3}$$

In our setup the optical frequencies of both beams are equal $\omega_{\text{LO}} = \omega_\text{p}$ (homodyne detection) and thus the expression for the photocurrent yields [26]

$$\hat{i}_- = 2\alpha_{\text{LO}}\alpha_\text{p} \cos\phi + \sqrt{2}\alpha_{\text{LO}} \left(\delta\hat{X}_\text{p} \cos\phi + \delta\hat{Y}_\text{p} \sin\phi\right). \tag{1.4}$$

[5] Thorlabs PDB420C-AC balanced detector.

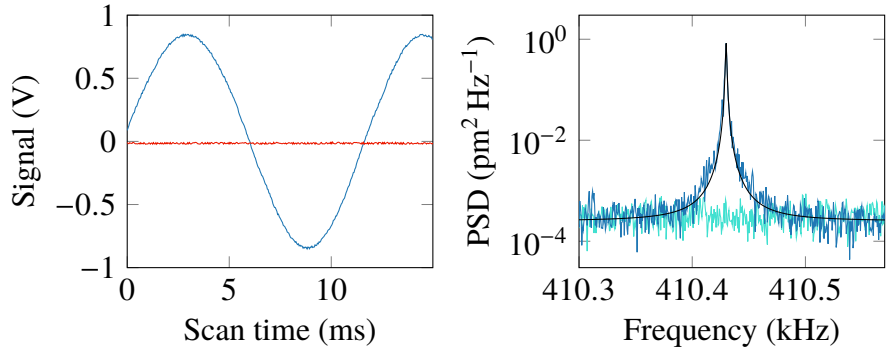

Figure 1.3: Interferometer calibration and sensitivity. Left: Measured signal $V_-(t)$ from the balanced homodyne detection as a function of time while scanning ϕ (blue) to extract the full-fringe amplitude V_{ff}. With this we calibrate small excursions of the locked signal (red) into displacement. Right: Calibrated PSD of thermal motion measured at the center of a square membrane using a probe beam power of 600 µW (blue). The SN background and a Lorentzian fit to the peak are shown in cyan and black, respectively. Redrawn from [1].

Here $\delta\hat{X}_{\mathrm{p}}$ and $\delta\hat{Y}_{\mathrm{p}}$ are the amplitude and phase quadrature fluctuations of the probe beam, respectively, as defined in Equations (A.41) and (A.42). The first term in Equation (1.4) describes the interference between the probe and the LO, which can be seen by sweeping the relative phase ϕ. The resulting interference fringes are shown in Figure 1.3. Indeed, the voltage signal $V_-(t) \propto \langle \hat{i}_- \rangle$ is a sinusoidal function with (full fringe) amplitude $V_{\mathrm{ff}} \propto \mathcal{V}\alpha_{\mathrm{LO}}\alpha_{\mathrm{p}}$, where $\mathcal{V} \approx 92\,\%$ is the typical fringe visibility. We want to detect only the phase $\langle \delta\hat{Y} \rangle \propto q(t)$, where $q(t)$ is the out-of-plane mechanical displacement of the membrane. To this end, we actively stabilize Δl using a proportional-integral controller to the mid-fringe position, i.e., such that $\phi = \pm(2n-1)\pi/2$, where n is an integer. In this case, small voltage signals $V_-(t) \ll V_{\mathrm{ff}}$ are proportional to $q(t)$ and can be calibrated into displacement:

$$q(t) \approx \frac{V_-(t)}{4\pi V_{\mathrm{ff}}}. \tag{1.5}$$

In practice, we extract V_{ff} once and subsequently measure the signal while applying a calibration tone with known frequency and voltage to the PZT in the LO arm. The tone then serves as a reference displacement, independent of power drifts affecting α_{LO} and α_{p} and thus the calibration via V_{ff}.

At the mid-fringe position the incident powers on the two photodiodes are equal and common classical laser noise is rejected. As a result, the background in the (single-sided) power spectral density (PSD) of the calibrated signal is limited by shot noise (SN) and given by [24, 26]

$$S_q^{\mathrm{SN}} = \frac{\lambda c \hbar}{16\pi P_{\mathrm{p}}}, \tag{1.6}$$

where $P_{\mathrm{p}} = \hbar\omega_{\mathrm{p}}|\alpha_{\mathrm{p}}|^2$ is the optical power of the probe beam absorbed by the detector. Figure 1.3 shows such a spectrum demonstrating a sensitivity of $(S_q^{\mathrm{SN}})^{1/2} \approx 10\,\mathrm{fm}/\sqrt{\mathrm{Hz}}$. This corresponds to $P_{\mathrm{p}} \approx 7\,\mu\mathrm{W}$ according to Equation (1.6). Although much smaller

than the incident power on the membrane of $\sim 600\,\mu W$, this value is reasonable considering the membrane reflectance of $|r_m|^2 \approx 19.2\,\%$[6], as well as the estimated total losses from optical elements, the mode matching, and the detector's quantum efficiency that amount to about 85 %.

The sensitivity of the interferometer is sufficient to detect thermal motion of nanomechanical membranes. This is demonstrated using a square SiN membrane with a thickness of $h = 60\,nm$ and side length of $l = 1\,mm$. In Figure 1.3 we show the calibrated PSD for the fundamental mode at $\Omega_m/2\pi = 410.5\,kHz$ and at room temperature probed in the center, where the displacement is maximal. We calculate the membrane's effective mass $m_{eff} \approx 34\,ng$ with a density of $\rho = 2.7\,g\,cm^{-3}$ using Equation (A.10), and moreover find the root mean square (rms) displacement $\sqrt{\langle q^2\rangle} \approx 4.2\,pm$ via Equation (A.52). According to Equation (A.16), this means that the peak value in the spectrum,

$$S_q(\Omega_m) = \frac{4Q\langle q^2\rangle}{\Omega_m}, \tag{1.7}$$

amounts to $S_q^{1/2}(\Omega_m) \approx 1.65\,pm^2\,Hz^{-1}$ assuming $Q = 10^5$, which is in good agreement with the data. The signal-to-noise ratio (SNR) is $S_q(\Omega_m)/S_q^{SN} \approx 40\,dB$.

1.2.1.3 Raster-scan method

Our setup allows us to transversally position the probe beam on the membrane and to raster-scan it across a given area. At each point of the scan, we extract the rms displacement of several eigenmodes by numerically integrating the corresponding peaks in the spectrum $S_q(\Omega)$ (see Appendix A.2.2). From this data we compose displacement maps as shown in Figure 1.4 for the thermally excited modes of the square SiN membrane. The measured displacement patterns are in excellent agreement with those calculated using a symmetrized form of Equation (A.8), that is,

$$w(x, y, t) \propto \sin(nkx)\sin(mky) + \beta\sin(nky)\sin(mkx). \tag{1.8}$$

Here $k = \pi/l$ and $n, m \geq 1$ are the number of antinodes along the in-plane coordinates x and y, respectively. $|\beta| < 1$ denotes the degree of hybridization. With our measurements we find that nearly degenerate modes such as $(n, m) = (1, 2)$ and (2,1) hybridize with $\beta \approx 0.2$. The rms displacements of the modes correctly scale as $\sqrt{\langle q^2\rangle} \propto \Omega_m^{-1} \propto (n^2 + m^2)^{-1/2}$, where we used the expression for the mode frequency in Equation (A.9).

Raster-scans with our interferometer may require long measurement times, depending on the number of points in the grid and the quality factors of the modes to be analyzed. This is because at each measurement point the spectrum $S_q(\Omega)$ must be averaged for much longer than the ringdown time Γ_m^{-1}, since the amplitude of the membrane changes on that timescale. While in Figure 1.4 we used 22×22 points and the total measurement time was only 8 min, a scan with more points and higher quality factors, such as the one presented in Section 1.3, can take several hours. It should be noted,

[6]The reflectance $|r_m|^2$ is calculated via Equation (2.4) with $\lambda = 1064\,nm$, $n = 2.0$, and $h = 60\,nm$.

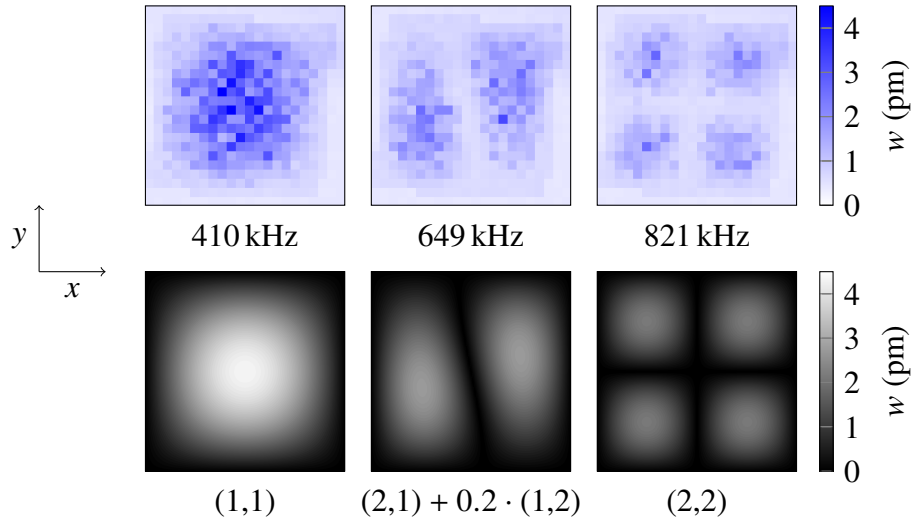

Figure 1.4: Interferometric raster-scan of SiN membrane modes. Top: rms displacement w of thermal motion measured on a 22×22 point grid across the surface of a square SiN membrane with side length of $l = 1$ mm at room temperature. The frequencies of the modes are shown below. Bottom: Calculated mode shapes and corresponding mode indices below. Redrawn from [1].

however, that we could artificially reduce the ringdown time by increasing the pressure in the vacuum chamber and thus increase gas damping of the membrane motion. In Section 3.2.1 we present another way to shorten the measurement time by coherently driving a mode during the raster-scan using the PZT mounted in the vacuum chamber. As an additional benefit, we can thereby compose a displacement map which includes information about the relative phase of motion at different points.

1.2.1.4 Ringdown technique

We are interested in determining the quality factor Q via mechanical ringdown measurements, that is to say, measuring the time constant Γ_m^{-1} which characterizes the duration of the amplitude decay (see Equation (A.12)). To this end, we first have to excite the membrane motion to an amplitude much larger than the thermal motion, then switch off the excitation and subsequently record the displacement $q(t)$ over time. In our setup the excitation is done in one out of two ways: one option is to simply drive the PZT mounted close to the membrane in the vacuum chamber at the frequency of a mechanical mode Ω_m. The PZT can exert large forces, which is why we are not only able to drive eigenmodes of thin SiN membranes with low effective masses but also larger structures such as their silicon frames, as demonstrated in [23].

The other option is to optically excite membrane modes via radiation pressure. For this we employ a diode laser at wavelength of 880 nm, amplitude-modulated using an acousto-optic modulator (AOM) and introduced in the probe arm of the interferometer via a dichroic BS, as shown in Figure 1.2. By periodically switching on and off the drive of the AOM at the mechanical frequency Ω_m, the excitation beam, impinging on the

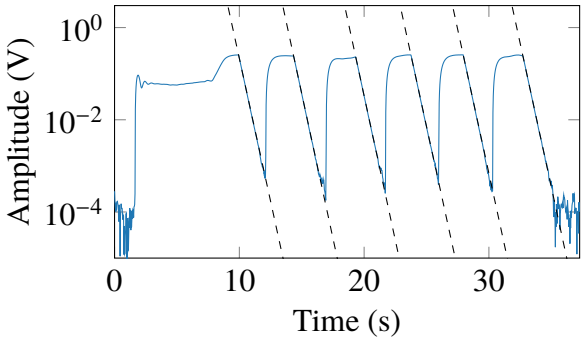

Figure 1.5: Ringdown measurements of a SiN membrane mode. We excite the membrane motion at a frequency of $\Omega_m/2\pi = 610\,\mathrm{kHz}$ and simultaneously detect its amplitude with a lock-in amplifier (blue line). After switching off the drive, the exponential decay is recorded and fit (dashed lines) to extract the quality factor. We repeat the procedure six times and get an average value of $Q = 666(2) \times 10^3$.

membrane at the same spot as the probe beam, exerts the following radiation pressure force, derived from the fact that each photon carries a momentum of $2\pi\hbar/\lambda$:

$$F_{\mathrm{rad}}(t) = \frac{2|r_m|^2 P_0}{c} \left(\mathrm{sgn}\left(\sin\left(\Omega_m t\right)\right) + 1\right), \tag{1.9}$$

where r_m is the amplitude reflection coefficient of the membrane, c is the speed of light in vacuum, and P_0 is the modulation amplitude of the incident power. The factor of two is included because each photon transfers twice its momentum onto the membrane upon reflection. In the frequency domain $F_{\mathrm{rad}}(t)$ has a large component at Ω_m, as well as higher-order harmonics at frequencies $> 2\Omega_m$. Since the latter may drive higher-order mechanical modes that could disturb our signal, we filter the signal in a narrow band around Ω_m. Inserting only the Ω_m-component of the force into the equation of motion, i.e. Equation (A.11) with $F_{\mathrm{th}}(t) \rightarrow F_{\mathrm{rad}}(t)$, and solving for the rms amplitude of the driven motion yields

$$q_{\mathrm{rad}} = \frac{\sqrt{2}|r_m|^2 Q P_0}{m_{\mathrm{eff}}\Omega_m^2 c}. \tag{1.10}$$

For the fundamental mode of the same SiN membrane detailed above, $|r_m|^2 \approx 24.3\,\%$,[7] and a typical power of $P_0 = 1\,\mathrm{mW}$, this amounts to $q_{\mathrm{rad}} \approx 508\,\mathrm{pm}$, which is more than two orders of magnitude larger than the thermal motion.

The signal generated from the excited mechanical motion is analyzed using a lock-in amplifier[8], filtering a single mode with a narrow bandwidth. The bandwidth is chosen to be approximately 10–100 times larger than the expected mechanical linewidth Γ_m depending on the noise found around the peak in the spectrum. We monitor the amplitude while fine-adjusting the drive frequency and switch off the beam modulation when the amplitude is significantly larger than the background noise. Afterwards the exponential decay is recorded. An example of this method is shown in Figure 1.5,

[7] $|r_m|^2$ is calculated via Equation (2.4) with $\lambda = 880\,\mathrm{nm}$, $n = 2.0$, and $h = 60\,\mathrm{nm}$.
[8] Zurich Instruments HF2LI

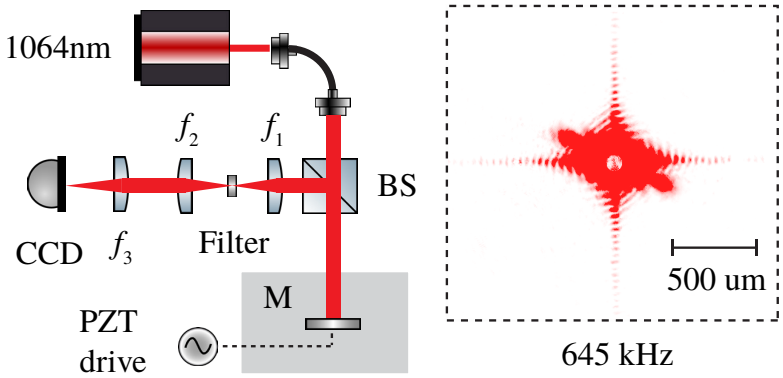

Figure 1.6: Illustration of the darkfield imaging setup. Left: Using laser light at $\lambda = 1064\,\text{nm}$ the membrane (M) is imaged onto a CCD camera and filtered with an opaque disk after the first lens f_1. A dark field image of the displacement is observed while the membrane is resonantly driven with a PZT. Right: Fourier image of a driven membrane while the opaque disc blocks the zero-order diffraction light.

where the described procedure is repeated six times to extract the mean value and the statistical uncertainty of the quality factor $Q = 666(2) \times 10^3$ for a SiN membrane mode at a frequency of $\Omega_m/2\pi = 610\,\text{kHz}$.

1.2.2 Dark field imaging

We now discuss an experimental method known as dark field imaging which allows us to characterize mechanical modes in a much shorter time than with the raster-scan interferometer. Once again our description will closely follow [1].

1.2.2.1 Optical Fourier filtering

Dark field microscopy is a well-known and often employed technique to enhance the contrast of micrographs. It is based on a sample illumination which permits only light scattered from the sample to enter the objective. The result is a high-passed image emphasizing sharp edges of the sample. Our setup shown in Figure 1.6 uses a similar principle, isolating diffracted light from the membrane to directly image the squared displacement pattern of the membrane onto a CCD camera. This interesting method, first employed in [27] within our field, can be understood by recalling simple principles of Fourier optics [28], which we will now elaborate.

In our setup we shine collimated laser light at a wavelength of $\lambda = 1064\,\text{nm}$ perpendicularly onto a sample, here a SiN membrane placed inside a high vacuum chamber. The beam diameter of 2.4 mm is significantly larger than the membrane with side length $l = 1\,\text{mm}$, such that we can assume the incident electric field $E_0 e^{i\omega_l t}$ to be constant across the membrane. At a transverse position (x, y) the membrane is displaced by $w(x, y, t)$ and shifts the phase of the reflected electric field E_r. For $w(x, y, t) \ll \lambda$ we find the following:

$$E_r \approx |r_m| E_0 e^{i\omega_l t}(1 + ikw(x, y, t)), \tag{1.11}$$

where r_m is the reflection coefficient of the membrane, $k = 2\pi/\lambda$, and $\omega_\mathrm{l} = ck$. After reflecting from a BS the light is focused using a lens with a focal length of $f_1 = 75\,\mathrm{mm}$. At the focal (or Fourier) plane of the lens we thereby perform an optical Fourier transform $\mathcal{F}$ with respect to (x, y) resulting in:

$$\mathcal{F}[E_\mathrm{r}] = |r_\mathrm{m}|E_0 e^{i\omega_\mathrm{l} t}(\mathcal{F}[1] + \mathcal{F}[ikw(x, y, t)]). \tag{1.12}$$

The second term on the right hand side of Equation (1.12) describes diffracted light due to the membrane displacement $w(x, y, t)$. The first term refers to tightly focused, unscattered light, which we block by placing an opaque disc in the Fourier plane. The diffracted light is then transformed by another lens with a focal length of $f_2 = 50\,\mathrm{mm}$. Imaged onto a CCD camera we capture an intensity pattern, proportional to the squared membrane displacement and time-averaged over many oscillation cycles of the motion:

$$I(x', y') = I_0|r_\mathrm{m}|^2 k^2 \left\langle w(-x, -y, t)^2 \right\rangle . \tag{1.13}$$

Here $I_0 = |E_0 e^{i\omega_\mathrm{l} t}|^2$ and we used the fact that applying the Fourier transform twice simply flips the sign of the coordinates x and y. In order to magnify the image we place a third lens with $f_3 = 35\,\mathrm{mm}$ before the camera.

Figure 1.6 also shows an image of the Fourier plane which can be observed by positioning the camera in the focal plane of f_3. The cross-shaped diffraction pattern around the center is due to the membrane's sharp edges. Diagonally extending from the center two bright spots can be seen which arise from the displacement of a hybridized mode, mixing (1,2) and (2,1) at a frequency of 645 kHz. In the center of the image a white dot shows the opaque disc, a thin film of aluminum deposited onto a glass wafer. From geometric considerations we estimate that the disc blocks diffraction with angles

$$\alpha \lesssim d/2f_1, \tag{1.14}$$

where $d = 100\,\mu\mathrm{m}$ is the disc diameter. As a result, mechanical modes are visible whose distance between nodes is $\lesssim \lambda/2\alpha \approx 800\,\mu\mathrm{m}$.

1.2.2.2 Results and limitations

In Figure 1.7 we present dark field images of three SiN membrane modes. These images were recorded with an optical power of $\sim 100\,\mu\mathrm{W}$, while sweeping a PZT mounted inside the vacuum chamber in the frequency range 400 kHz...2 MHz with a sweep time of $\sim 1\,\mathrm{min}$ and capturing an image every 10 ms. To clearly image the displacement patterns we had to use a large PZT stroke of $\gtrsim 300\,\mathrm{pm}$ which causes nonlinear behavior such as Duffing-type frequency shifts and strong hybridization of the membrane modes. For example, we find $\beta \approx 1$ for the modes (5, 3) and (3, 5) at a frequency of 1.683 MHz. In order to use a smaller PZT drive and to avoid nonlinearities we have to improve the sensitivity of the setup. According to Equation (1.13), we can simply intensify the light since the signal is proportional to I_0. However, in doing so we also increase the amount of light scattered from optics which currently constitutes our measurement background. To improve the SNR we therefore have to minimize reflections as well as stray light.

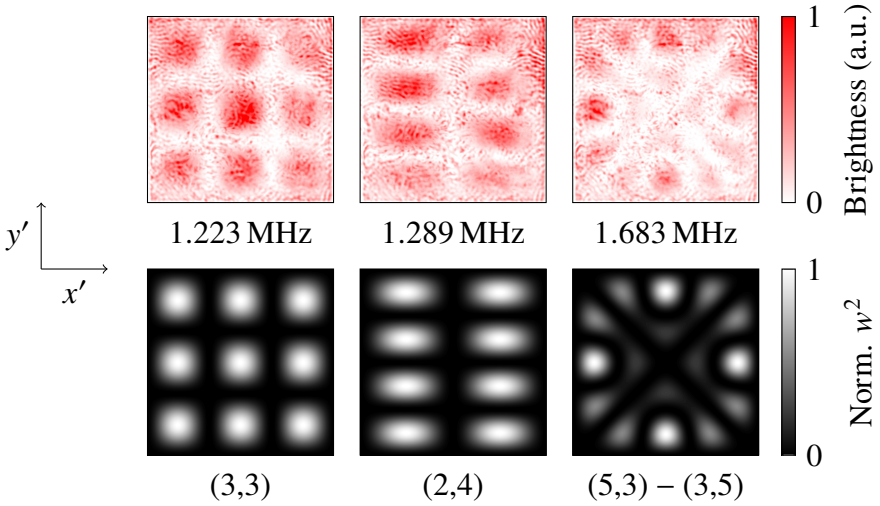

Figure 1.7: Darkfield imaging of SiN membrane modes. Top: Dark field images of mechanical modes of a square SiN membrane with side length of 1 mm. The membrane was driven by a PZT at the frequencies shown below. Bottom: Calculated normalized squared mode displacement and corresponding mode indices below. Redrawn from [1].

It is important to note that the dark field imaging technique is not useful for membranes with sharp, distinct features, such as those found in the patterned SiN membrane presented in Section 1.3. Similarly to the edges of the membrane appearing in the Fourier image in Figure 1.6 the pattern causes diffraction that is much more pronounced than the displacement and therefore obscures the latter.

1.2.3 Polarimetric stress analysis

As mentioned in the introduction, high tensile stress constitutes an important characteristic of SiN resonators used in optomechanics. For the patterned SiN membranes described in Section 1.3, we are particularly interested in studying the stress distribution, whose periodicity contributes to the emergence of a phononic bandgap that enhances mechanical quality factors. For this reason, we implemented a measurement technique known as a gray field polarimetry [29], which analyzes the stress anisotropy of birefringent films based on the photoelastic effect. The work presented here has been published in [2].

1.2.3.1 Gray field polariscope

Figure 1.8 shows an illustration of our gray field polariscope based on bandpass filtered light from a 780 nm high power LED. Before shining it onto a membrane we use a lens to focus the light onto a diffuser plate and collect the transmitted light with another lens in order to get a beam with a smoothend intensity distribution (Köhler illumination). Afterwards, we place a thin film polarizer and a quarter-wave plate to circularly polarize the light. The birefringent sample slightly changes the polarization

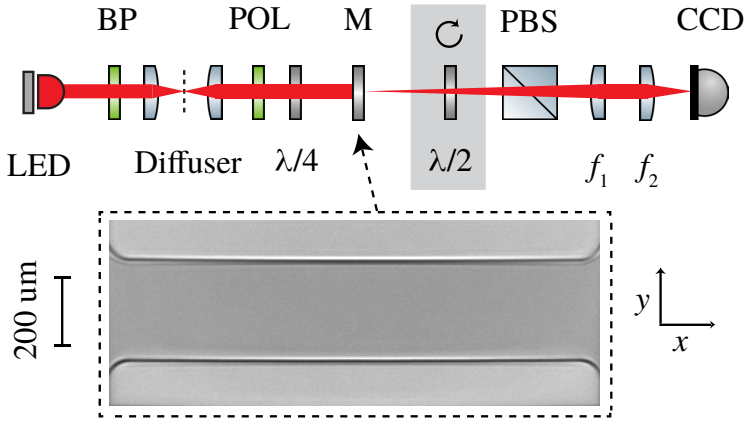

Figure 1.8: Illustration of the gray field polariscope setup. Top: Light from an LED at $\lambda = 780\,\text{nm}$ is bandpass filtered (BP), circularly polarized using a polarizer (POL) and a quarter-wave plate ($\lambda/4$), and then used to illuminate the membrane (M). On the other side of the membrane we place a half-wave plate ($\lambda/2$) and a PBS, and image the membrane onto a CCD camera. The half-wave plate is mounted on a motorized rotation stage. Bottom: A microscope image of a SiN ribbon used in the experiment.

state which is analyzed in transmission using a half-wave plate mounted on a motorized rotation mount, a PBS, and a CCD camera. A microscope objective and a lens in front of the camera are used to image the sample with a magnification of 10.

To calculate the signal detected at a given pixel of the camera we use Jones calculus (see Appendix A.5) and start by defining the input vector $\vec{E}_{\text{in}}$ to be incident at each area element of the birefringent membrane. The latter is described by the Jones matrix of an arbitrarily rotated phase retarder $\mathbf{J}_{\delta,\theta}$, where the retardation δ is proportional to the stress anisotropy $\Delta\sigma$ and the membrane thickness h [29]:

$$\delta = khC\Delta\sigma. \tag{1.15}$$

Here $k = 2\pi/\lambda$, h is the membrane thickness and C is a material parameter known as the photoelastic (or Brewster) coefficient. The direction of the stress anisotropy θ is defined with respect to the optical axis. In a similar fashion, the half-wave plate in our setup, whose fast axis is at an angle α, corresponds to $\mathbf{J}_{\pi,\alpha}$. Finally, the Jones vector at a given pixel of the CCD camera reads

$$\vec{E}_{\text{out}} = \mathbf{P}_{\text{s}}\mathbf{J}_{\pi,\alpha}\mathbf{J}_{\delta,\theta}\vec{E}_{\text{in}}, \tag{1.16}$$

where $\mathbf{P}_{\text{s}}$ describes the polarizer transmitting only s-polarized light. Assuming perfect circular polarization at the input the normalized intensity at each pixel $I_{\text{out}} = |\vec{E}_{\text{out}}|^2$ yields

$$I_{\text{out}} = \frac{1}{2} - \frac{1}{2}\sin(4\alpha - 2\theta)\sin(\delta). \tag{1.17}$$

When $\delta = 0$ the intensity at the CCD is half of that used to illuminate the membrane. For this reason the configuration is known as a gray-field polariscope. Figure 1.9 shows I_{out} for different values of retardation δ and an angle $\theta = 0$ determining the amplitude and the phase of the sinusoidal function, respectively.

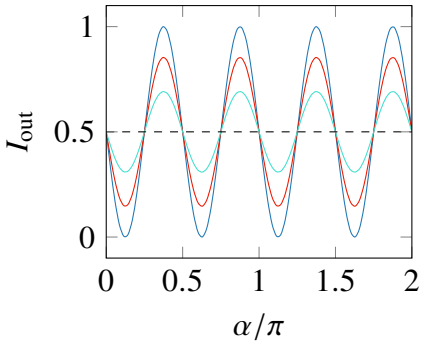

Figure 1.9: Gray field polarimetry signal. Calculated normalized pixel intensity versus rotation angle of the half-wave plate. For the retardation δ we use $\pi/2$ (blue), $\pi/4$ (red), and $\pi/8$ (cyan). For all traces the angle of the principle stress is $\theta = 0$. The dashed black line is the expected signal without a birefringent membrane ($\delta = 0$).

In the experiment we perform a full rotation of the half-waveplate while capturing images of the membrane at ten equally spaced values of α. Then, for each image and at each pixel, we calculate the Fourier transform normalized to the average value of the signal in order to extract the frequency component with a period of $\alpha = \pi/2$. Before extracting δ and θ from the data we subtract background images which are taken without a membrane and transformed in the same way as described above. In particular this procedure removes contributions from imperfect input polarization.

1.2.3.2 Photoelastic coefficient

To demonstrate our gray-field polariscope we now present measurements of a SiN ribbon with a thickness of $h = 210\,\text{nm}$ and a width of $\sim 200\,\mu\text{m}$. A microscope image of the ribbon is shown in Figure 1.8. The ribbon is suspended from the silicon frame on two sides such that tensile stress is expected to be present only along the $x-$direction. As shown in Figure 1.10 we clearly observe over most of the surface of the ribbon this feature, i.e., a large retardation with a constant angle θ, which we set to zero. Close to the silicon frame we find a non-trivial distribution of stress anisotropy that is in agreement with finite-element simulations. In particular, we reproduce a small region with no birefringence in the center. Rounded fillets at the edges of the clamping cause stress to be directed towards the center.

Very close to the silicon frame and at the edges of the SiN film we see lines with large retardation ($> 15\,\text{mrad}$). We attribute these lines to diffraction effects which are also visible in each of the 10 images use to compose the data in Figure 1.10. Rotating the half-wave plate the diffraction pattern slightly changes such that for our algorithm it becomes indistinguishable from features due to photoelasticity.

Equation (1.15) reveals that careful measurements of the retardation, the membrane thickness, and the stress asymmetry let us experimentally determine the photoelastic coefficient C. To this end, we analyze a second ribbon, for which we measure the initial tensile stress $\sigma = 1190(20)\,\text{MPa}$ of the 210-nm-thick SiN film before releasing

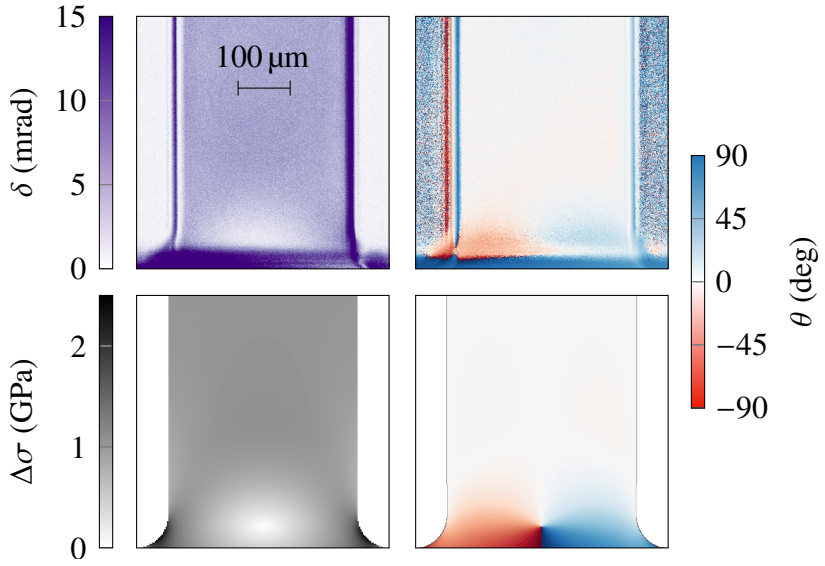

Figure 1.10: Stress analysis of a SiN ribbon. Top: Retardation δ (left) and angle of optical axis (right) measured with our gray field polariscope at one end of a SiN ribbon with a film thickness of 210 nm. Bottom: Simulated stress anisotropy $\Delta\sigma$ (left) and angle of principle stress θ (right) for the same device as above. Redrawn from [2].

the ribbon. The redistribution of the stress after the release can be accounted for by multiplying σ with the factor $1 - \nu$, where $\nu = 0.27$ is Poisson's ratio of SiN. In Figure 1.11 we present the data for this ribbon. Here we average the retardations across a number of pixels in the center of the ribbon, where the values are large and approximately homogenous, which results in $\delta = 6.4(2)$ mrad.

At this point it is important to recall that our measured retardation is slightly overestimated due to multiple reflections in the film. We see this when we calculate the retardation using the transfer-matrix method (TMM) (see Appendix A.4) and compare it with Equation (1.15). Given any small birefringence $\Delta n = C\Delta\sigma$, the value we obtain from the TMM is larger by a factor of $\eta = 1.26$. This means that we can simply rescale our measured result and calculate

$$C = \frac{\delta}{\eta k h \sigma (1 - \nu)} \approx 3.4(1) \times 10^{-6}\,\mathrm{MPa}^{-1}. \tag{1.18}$$

The value compares favourably with that reported for a similar amorphous material such as silicon dioxide with $C \approx 4 \times 10^{-6}\,\mathrm{MPa}^{-1}$ [30]. Remarkably, it differs by two orders of magnitude from the value presented in [31], where the refractive index of SiN films as a function of different fabrication parameters is studied. The linear relation between n and σ used to calculate C in this previous work may not only be due to the photoelastic effect. Our method, on the other hand, infers C directly from birefringence caused by stress anisotropy.

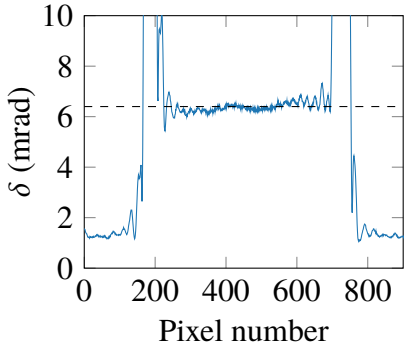

Figure 1.11: Measurement of the photoelastic coefficient in SiN. Retardation δ averaged across 1000 pixels in the center of a SiN ribbon where the values are approximately homogenous. We finally average the central interval between the two large peaks and get $\delta = 6.4(2)$ mrad (dashed line). By comparing this result to the measured stress anisotrophy we find $C = 3.4(1) \times 10^{-6}\,\mathrm{MPa}^{-1}$. Redrawn from [2].

1.3 Device features

In this section we introduce the design of our patterned SiN membranes based on a phononic crystal structure and a defect which hosts localized vibrational modes. A detailed study of their mechanical properties is presented demonstrating in particular extremely high quality factors of $Q > 10^8$ at room temperature. The results revealed in this section have been published in [3]. As mentioned before, the fabrication process is not discussed here but can be found in the Supplementary Information of [3].

1.3.1 Phononic crystal structure

1.3.1.1 Phononic bandgap

Phononic crystals are periodic structures that suppress phonons in a given frequency band. This phenomenon is described by the interference of elastic waves scattered at each unit cell of the structure. A simple example is given by an infinite chain of alternating masses and springs, similar to a diatomic chain employed as a model for crystalline solids [32]. The dispersion relation in such a scenario can be calculated analytically and features a frequency interval, known as a phononic bandgap, where no solution exists.

The first realizations of phononic crystals as part of nanomechanical resonators in the context of optomechanics are found in silicon nanobeams [33]. Here periodically etched holes surround a defect, which localizes tightly confined mechanical modes in the GHz regime. SiN membranes with $\sim$ MHz frequencies and phononic bandgap shields in the silicon substrate have recently been studied in [22, 23], revealing a significant suppression of phonon tunneling losses and consistently enabling high quality factors of $Q > 10^7$ at liquid-helium temperatures [34, 35].

In this work, we directly pattern the stressed SiN membrane with a phononic crystal. Figure 1.12 shows a micrograph of such a structure. The membrane has number of

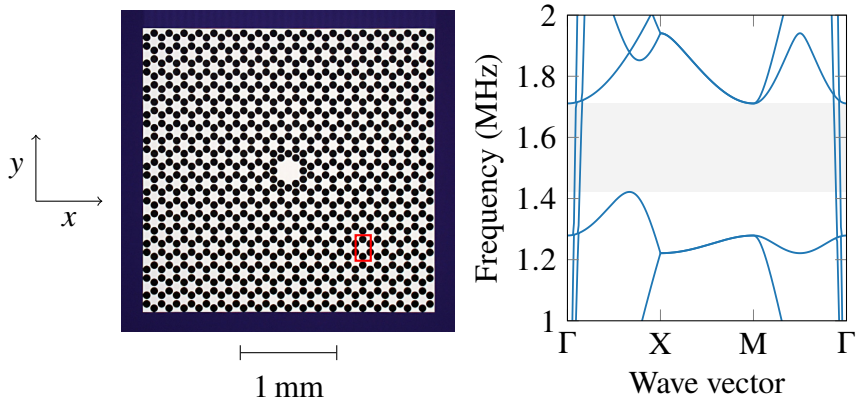

Figure 1.12: Device design. Left: Microscope image of a 66-nm-thick patterned SiN membrane. A single unit cell is indicated with a red rectangle. Right: Simulated band diagram of an infinite arrangement of unit cells showing a large quasi bandgap around 1.6 MHz (gray shaded area). Adapted from [3].

circular holes, arranged in a hexogonal honeycomb structure with a lattice constant of $a = 160\,\mu\text{m}$. By removing and displacing a few holes in the center we define a defect of characteristic size $\sim a$, which hosts localized modes, as discussed below. The simulated band diagram of an infinite arrangement of unit cells is shown on the right hand side of Figure 1.12. In the frequency interval from 1.41 MHz to 1.72 MHz we find a quasi bandgap that suppresses out-of-plane modes, while in-plane-modes with a high phase velocity (visible near the Γ points in Figure 1.12) are permitted by the structure.

1.3.1.2 Stress distribution

There is a crucial difference between phononic crystal structures in silicon and those presented here. While both are based on alternating masses as mentioned above, the pattern in the SiN film periodically modulates the speed of sound. This is due to the presence of tensile stress, redistributing after we introduce the pattern, and is the predominant feature for the emergence of the bandgap.

To understand this better, we employ our gray field polariscope (see Section 1.2.3) and image the stress anisotropy around a thin tether of the structure. As shown in Figure 1.13, we extract the retardation along a certain line across the tether and contrast it with the simulated stress anisotropy in the same section. Without free parameters and using the photoelastic coefficient determined in Section 1.2.3, the data and simulation are in excellent agreement. We find a peak value of $\Delta\sigma = 2.6\,\text{GPa}$ that is more than twice as large as the initial stress of the SiN measured before etching of $\sigma_{\text{init}} \approx 1.27\,\text{GPa}$. In the center of the unit cell, where the retardation is zero, simulations show that the stress is $\sim \sigma_{\text{init}}/2$. To correctly engineer the elastic response of the phononic crystal it is essential to know and incorporate this stress distribution.

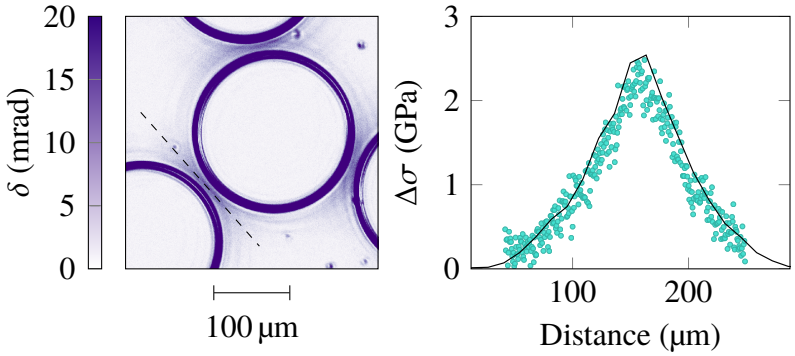

Figure 1.13: Polarimetric stress analysis of a patterned SiN membrane. Left: Retardation δ measured with grey field polariscope around a tether of the patterned SiN membrane. The dashed line indicates the cross section used in the plot to the right. Right: Stress anisotropy $\Delta\sigma$ as a function of distance across the tether as simulated (black line) and extracted from the measured retardation (cyan dots). Adapted from [2].

1.3.2 Defect mode properties

1.3.2.1 Mode shape

Using our raster-scan interferometer (see Section 1.2.1), we probe thermal motion across a small area in the center of the defect and average the calibrated spectra together. As shown in Figure 1.14, we thereby identify a frequency band with a low mode density agreeing to within 2 % with the expected phononic bandgap. While below and above the bandgap an abundance of sharp peaks are found, the window between 1.4 MHz and 1.7 MHz consists of only five individual peaks.

To examine the vibrational mode shapes we zoom in to a 1.2 mm × 1.2 mm area around the defect and measure the displacement pattern of the defect modes using our raster-scan method. In Figure 1.15 we show the result for three different modes. Mode A

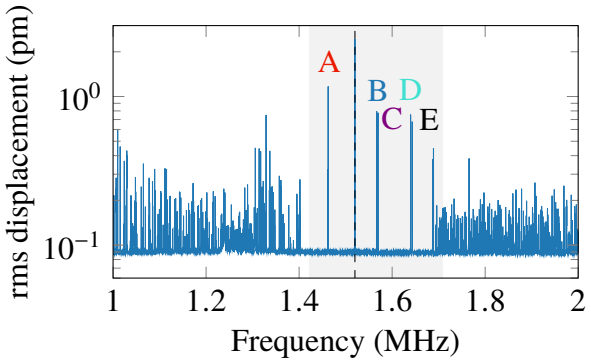

Figure 1.14: Displacement spectrum measured at the defect. Probing the thermal displacement of the central defect with the characteristic dimension a = 160 nm we find five modes (A-E) between 1.41...1.68 MHz. The gray shaded area shows the calculated bandgap and the dashed line indicates the frequency of the calibration tone. The data was acquired with a spectrum analyzer and a resolution bandwidth of 100 Hz. Redrawn from [1].

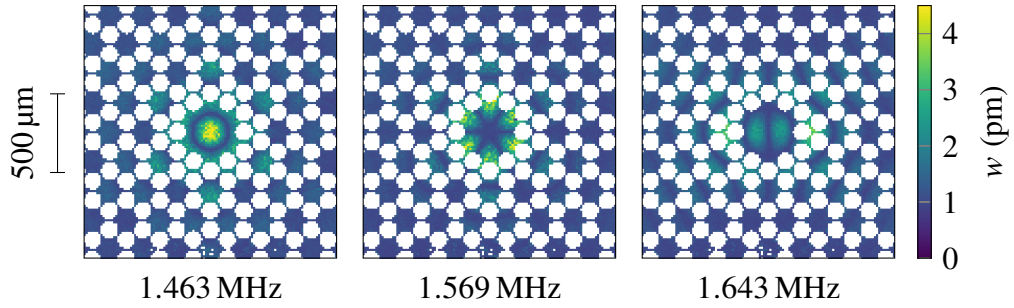

Figure 1.15: Displacement patterns of localized defect modes. Displacement w of thermal motion measured with the raster-scan interferometer at different points across the membrane for modes A, C, E (from left to right). The corresponding mode frequencies are shown below the plots. We detect holes by tracking the amplitude of the calibration peak and show them as white pixels. Redrawn from [1].

can be considered a fundamental mode of the defect since we find only a single antinode at the geometric center. Mode E features a centered nodal line with two anti-nodes on either side – a displacement pattern similar to the first harmonic of a circular membrane. All defect modes penetrate the periodic structure up to a distance of $\sim 500\,\mu\text{m}$ from the center before the mode displacement is too small to be detected by the interferometer. This strong localization is the result of the fact that elastic waves at these frequencies are blocked by the phononic crystal.

1.3.2.2 Effective mass

With a measurement of the mode displacement at a known temperature of $T = 300\,\text{K}$ and frequency Ω_m as demonstrated in Figure 1.15, we can calculate the effective masses using Equation (A.52). To this end, we first extract a background of $\sim 1\,\text{pm}$ from the edges of the displacement map and subtract it from the data. Then, we smoothen and determine the maximum displacement, which is found at a different position for each mode. Uncertainties of $\sim 11\,\%$ are given by the uncertainty of the displacement calibration established by repeating the calibration procedure ten times. Figure 1.16 shows the result of this analysis. Notice that a square SiN membrane without phononic crystal patterning and the same fundamental mode frequency as mode A has a comparable effective mass of $m_\text{eff} \approx 4.9\,\text{ng}$ according to Equation (A.10) and assuming a density of $\rho = 2.7\,\text{g}\,\text{cm}^{-3}$.

1.4 Ultrahigh quality factors

In this section we discuss the dissipation in our device and present a large dataset of quality factors measured for membranes with different thicknesses h and characteristic defect sizes a. For the latter we simply rescale the entire membrane, while leaving h constant. We analyze the scalings of the Q-factors with the geometric parameters a and h, and compare the data to a material loss model. We show that the ultrahigh quality

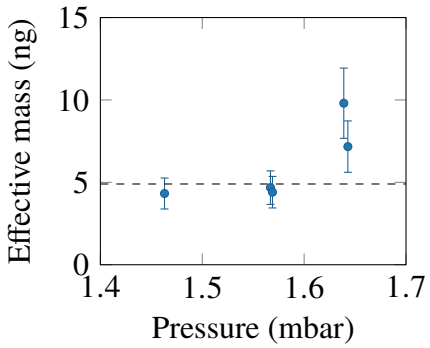

Figure 1.16: Effective masses of defect modes. We determine the effective masses from the maximum of displacement maps shown in Figure 1.15. The dashed line shows the calculated effective mass of a square membrane, whose fundamental mode has the same frequency as mode A.

factors are enabled by significantly reducing bending induced loss in our membranes (soft clamping) and confirm the result by finite-element simulations. As in the previous section, we closely follow our description in [3].

1.4.1 Dissipation mechanisms

In we show ringdown measurements at room temperature of mode A and E performed with the Michelson interferometer (see Section 1.2.1). For this, we use a larger device than before with $a = 346\,\mu\text{m}$ and a thickness of $h = 35\,\text{nm}$. With values well beyond 10^8 the quality factors extracted from these measurements are remarkably large and result in $Qf > 1 \times 10^{14}\,\text{Hz}$. These $Q \times f$ products are among the highest reported so far at room temperature, exceeding those of single crystal silicon and bulk quartz resonators [36], mirror suspensions at the Laser Interferometer Gravitational Observatory [37], as well as SiN trampoline resonators [20].

In order to better understand the extraordinary performance of our devices, we first discuss the microscopic origin of dissipation in SiN membranes. We distinguish three types of effects: gas damping, radiation loss, and material loss [15, 38]. Each of them, respectively, contributes to the total dissipation in the following way:

$$Q^{-1} = Q_{\text{gas}}^{-1} + Q_{\text{rad}}^{-1} + Q_{\text{mat}}^{-1}. \tag{1.19}$$

The first term is due to the membrane interacting with surrounding air molecules. As demonstrated on the right hand side in Figure 1.17, we see that this type of dissipation is proportional to the vacuum pressure $Q_{\text{gas}}^{-1} \propto p$ [39] and reduces our measured quality factor by $\sim 10\,\%$ at $p = 2 \times 10^{-7}\,\text{mbar}$.

Radiation losses are phonon-tunneling processes which are described by the overlap between frame modes of the silicon support and resonator modes [21]. The performance of SiN membranes without a phononic crystal structure suffers from this type of dissipation, since the mode displacement near the membrane edge is substantial [40]. In our device we control radiation losses by virtue of the phononic crystal structure [23]. This is supported by simulations of the residual displacements of the defect modes

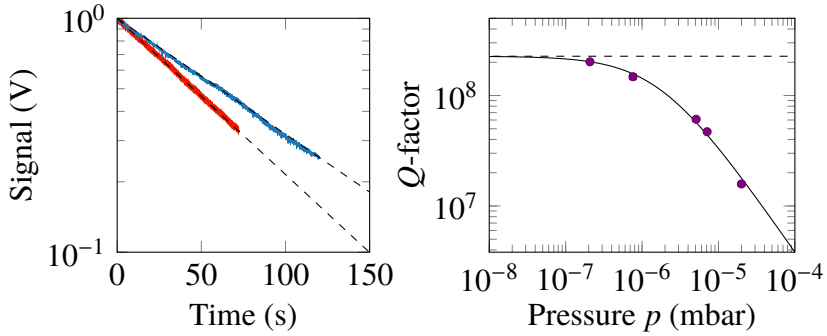

Figure 1.17: Quality factors of defect modes at room temperature. Left: Ringdown measurements of mode A at a frequency of $\Omega_m/2\pi = 690\,\text{kHz}$ (red) and mode E at $\Omega_m/2\pi = 777\,\text{kHz}$ (blue) of two membranes with $a = 346\,\mu\text{m}$ and $h = 35\,\text{nm}$. Dashed lines are exponential fits from which we extract Q-factors of $141(1) \times 10^6$ and $214(2) \times 10^6$, respectively. Adapted from [3]. Right: Vacuum pressure p dependence of quality factor for mode E (purple dots). The black solid line is a fit to $Q^{-1} = Q_0^{-1} + Q_{\text{gas}}^{-1}$, where $Q_{\text{gas}}^{-1} \propto p$ describes gas damping. At a perfect vacuum we would expect $Q_0 = 2.27 \times 10^8$ (dashed line) from which the measurement at $p = 2 \times 10^{-7}$ mbar deviates by about 10 %.

near the silicon frame (see Supplementary Information of [3]) that show a > 100-fold suppression of the motion compared to the displacement at the defect. Furthermore, in the experiment we confirm that the measured quality factors of the defect modes are widely unaffected by the clamping conditions.

Material loss, denoted Q_{mat}^{-1}, refers to mechanical energy lost directly in the resonator material. This includes thermoelastic damping [41] and Akhiezer damping [42], which are due to irreversable heat flow from strain-induced temperature gradients and phonon relaxation, respectively. For highly stressed SiN resonators in the MHz regime it has been estimated that thermoelastic damping allows for $Q > 10^{11}$ [18, 27]. Akhiezer damping limits the qualify factor to about $Q \sim 10^9$, which we estimate by following [43]. Another type of material loss is due to two-level defects coupling to strain fields [44]. Studies of the temperature dependence of Q in SiN resonators have shown clear signatures of the defects [45], suggesting that our devices are also currently limit by the effect. In the following section, we will build upon this assumption and use an analytical model for material loss to predict the scaling of Q with geometric parameters, such as the defect size and membrane thickness.

1.4.2 Geometric parameter dependence

1.4.2.1 Dissipation dilution

We now investigate the geometric parameter dependence of the measured Q-factors. Our data, presented below, is compared to a model for material loss, which has been developed for the case of highly stressed SiN strings [46,47] and square membranes [48]. In this model, known as the Zener model, a phase lag between the oscillating stress and the strain is assumed, as described by a complex Youngs modulus $E = E_1 + iE_2$ [49]. For small displacements it can be shown that mechanical energy is mostly lost through

bending of the thin film. On the other hand, the total energy stored in the resonator is dominated by the large tensile stress σ counteracting the displacement. This feature is referred to as dissipation dilution and explains the high quality factors of $\sim 10^6$ typically found in stressed SiN resonators.

For the fundamental mode of a square membrane the dissipation dilution model reveals the following expression:

$$Q^{-1} = (2\lambda + 2\pi^2\lambda^2)Q_{\text{int}}^{-1}, \tag{1.20}$$

where $Q_{\text{int}}^{-1} = E_2/E_1$ is the intrinsic dissipation influenced only by material parameters. The geometry and tensile stress dependence is described by the dilution factor

$$\lambda \approx \sqrt{\frac{E_1}{12\sigma}}\frac{h}{l}, \tag{1.21}$$

where h is the thickness and l is the side length of the membrane. The first term in Equation (1.20) is due to the bending near the membrane's edges, where the rigid silicon frame enforces clamped boundary conditions. The second term in Equation (1.20) is due to the bending at the antinode of the sinusoidal mode. Typically $\lambda \approx 10^{-4}$ is small, so that the second term can be neglected leaving only the first term and $Q^{-1} \approx 2\lambda Q_{\text{int}}^{-1}$. This means that most of the material loss occurs at the edges of the membrane.

In [50] the model has been extended to account for extra loss in a surface layer with thickness δh and imaginary part of Youngs modulus E_2'. Defining $\beta = E_1/(6\delta h E_2')$ the following equation holds:

$$Q_{\text{int}}^{-1} = Q_{\text{int,bulk}}^{-1} + \frac{1}{\beta h}, \tag{1.22}$$

where $Q_{\text{int,bulk}}^{-1}$ is the intrinsic damping in the bulk. Combining the above-mentioned equations in the case where surface losses dominate (thin membrane), an overall scaling of $Q \propto l/h^0$ is found and confirmed experimentally for a wide variety of stressed SiN strings and square membranes in [50].

1.4.2.2 Soft clamping

In the previous section we learned that bending at the edges of the membrane is the dominating contribution to material loss. Indeed, the fixed silicon frame is responsible for a sharp exponential correction of the sinusoidal membrane mode displacement with a decay length of $\sim \lambda l/4 \approx 37\,\text{nm}$ [48], where we use $E_1 = 270\,\text{GPa}$, $h = 35\,\text{nm}$, and $\sigma \approx 1.27\,\text{GPa}$. In contrast, the displacement pattern of the localized defect modes in our device are characterized by evanescent tails in the phononic crystal structure around the defect with a much larger decay length of $\sim 100\,\mu\text{m}$ and small displacements near the frame, eliminating the 'hard' clamp. The large decay length is similar to the distance between antinodes, which is why we suspect only a small contribution to the bending loss from the evanescent tails. If we eliminate the first term due to the bending at the

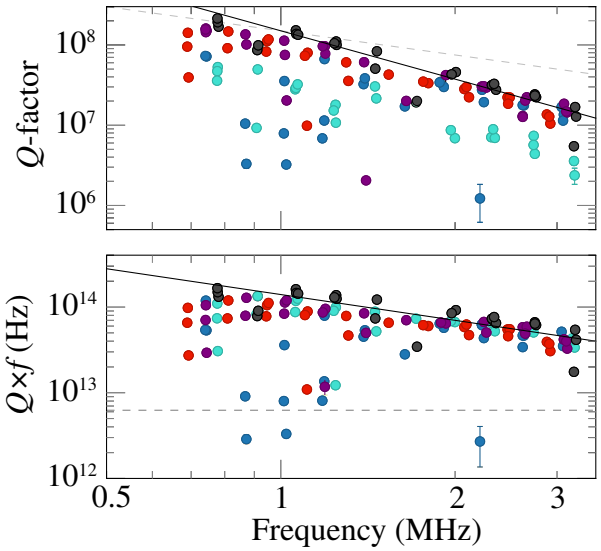

Figure 1.18: Frequency scaling of quality factors. Top: Measured Q for localized defect modes A (red), B (blue), C (purple), D (cyan), and E (black) of 35-nm-thick membranes with different defect sizes $a = 85...346\,\mu\text{m}$ as a function of mode frequency $\Omega_\text{m}/2\pi$. We plot the scalings $Q \propto \Omega_\text{m}^{-2}$ (solid line) and $Q \propto \Omega_\text{m}^{-1}$ (dashed line) as guides to the eye. Bottom: $Q \times f$-products for the same measurements. The dashed line indicates the required value for a single coherent oscillation at room temperature. Adapted from [3].

edges in Equation (1.20), we get a different expression than for the case of a square membrane:

$$Q^{-1} = \zeta \frac{E_1 h^2}{\sigma a^2} Q_\text{int}^{-1}. \tag{1.23}$$

Here the factor ζ depends on the exact shape of our defect modes. Finally, if surface loss are predominant the geometric parameter dependence of the quality factor is $Q \propto a^2/h$.

In order to verify that soft clamping indeed occurs in our device, we want to confront the model with experimental data from a systematic study of more than 80 patterned membranes and 400 defect modes, including membranes with different thicknesses h and characteristic defect dimensions a. As mentioned before, we vary a by rescaling the entire membrane, leaving h constant. In Figure 1.18 we show a subset of the data for $h = 35\,\text{nm}$ and a ranging from 85 µm to 346 µm. The quality factors Q and $Q \times f$ are plotted as a function of mode frequency $\Omega_\text{m}/2\pi \propto a^{-1}$. We see that the majority of defect modes have very high quality factors $Q > 10^7$, similar to those presented above. For all five modes we clearly find a scaling $Q \propto a^2 \propto \Omega_\text{m}^{-2}$ as expected from the soft clamping model in Equation (1.23). With the exception of a few data points, all $Q \times f$-products exceed $6 \times 10^{12}\,\text{Hz}$, a requirement for observing quantum-coherent evolution at a bath temperature of $T = 300\,\text{K}$. This is because the coherence time $\tau \approx \hbar Q/k_\text{B}T$ (see Equation (A.26)) is larger than the period of mechanical oscillation $1/\Omega_\text{m}$. For mode E of our best device with $\Omega_\text{m}/2\pi = 777\,\text{kHz}$ and $Q = 214(2) \times 10^6$ (see Figure 1.17), we expect $\tau\Omega_\text{m} \approx 27$ coherent oscillations at room temperature $T = 300\,\text{K}$. Notice that at a cryogenic temperature of $T = 4.2\,\text{K}$ the performance should improve even further, as

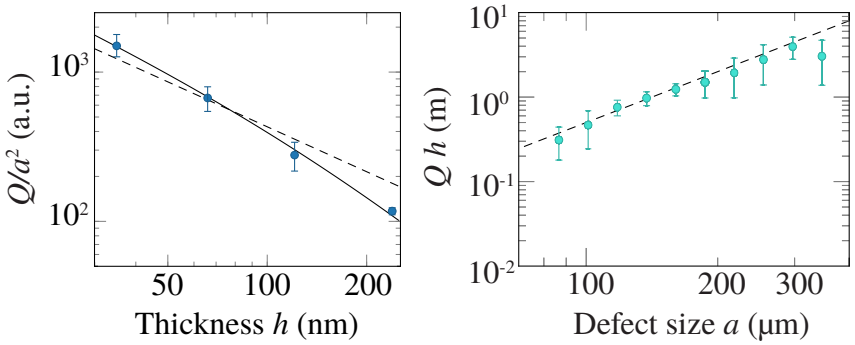

Figure 1.19: Geometric parameter scaling of quality factors for mode A. Left: Measured quality factor normalized by a^2 and averaged across different devices for mode A with a frequency of $\Omega_m/2\pi \approx 1.46\,\mathrm{MHz}$ as a function of membrane thickness. The behaviour follows $Q/a^2 \propto h^{-1}$ (dashed line), in particular when considering additional loss from the bulk (solid line). Right: Averaged Qh for mode A versus lattice constant exhibiting $Qh \propto a^2$ scaling as indicated by the dashed line. Adapted from [3].

here we estimate $\tau \approx 0.97\,\mathrm{ms}$, assuming a 2.5-fold increase of Q [23]. This coherence time is similar to those reported in trapped ions [51].

In Figure 1.19 quality factors are normalized to the defect dimension a for mode A, averaged and shown as a function of membrane thickness h. The data is consistent with the scaling expected from soft clamping $Q/a^2 \propto h^{-1}$. Allowing for contributions to the material loss from both bulk and surface of the membrane we get even better agreement, in particular for the case of thick membranes with $h = 240\,\mathrm{nm}$. Finally, we compare the defect size dependence across several thicknesses by plotting the averaged Qh versus a. Again, for mode A we have excellent agreement with our model as demonstrated on the right hand side of Figure 1.19. The other defect modes exhibit very similar behavior. Overall, our experimental data clearly evidences coherence enhancement via soft clamping.

1.4.3 Soft clamping simulations

We will now support our experimental findings with finite-element simulations.[9] To this end, we simulate eigenmodes of the entire structure. We reproduce the five defect modes, whose eigenfrequencies agree with the measured ones to within 2 %. The deviations are likely due to small differences in geometry and material parameters between the simulations and the physical device. Figure 1.20 shows the simulated displacement of mode A as a function of position along the y-direction. The displacement[10] $w(0, y)$ decays with a characteristic length of $\sim 100\,\mu\mathrm{m}$ from the center at $x = y = 0$, approximately described by the expression $w(0, y) \approx \mathrm{Re}(e^{ik|y|})$, where $k = 2\pi(0.57 + i0.085)/a$.

From the simulated displacement we directly access the quality factor using its definition as the ratio between the total energy stored in the resonator W and the energy

[9] The finite-element simulations were carried out by Y. Tsaturyan.

[10] Without loss of generality, we discard the time dependence of the displacement $w(x, y, t)$.

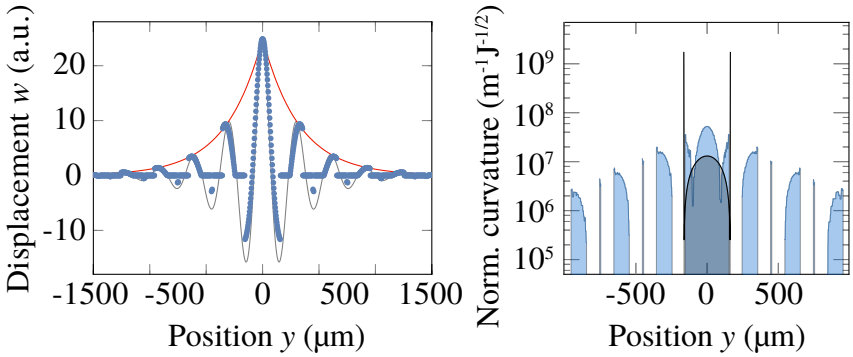

Figure 1.20: Simulated membrane displacement and curvature. Left: Simulated displacement of the defect and surrounding structure for mode A along the y-direction (blue dots) approximately following a decaying sinousoidal (gray line). The red line is an exponential function as a guide to the eye. Right: Simulated curvature evaluated along the same section and normalized to the square root of the total stored energy in the membrane (blue). The black line shows the simulated curvature of the fundamental mode of a square membrane with the same eigenfrequency. Adapted from [3].

dissipated per cycle ΔW [38]:

$$Q = 2\pi \frac{W}{\Delta W}. \tag{1.24}$$

Here ΔW is found by numerically integrating the mode curvature, that is to say, the second derivative of the displacement $w(x, y)$ [48]:

$$\Delta W = \int dV \frac{\pi E_2 z^2}{1-\nu^2} \left(\frac{\partial^2 w}{\partial x^2} + \frac{\partial^2 w}{\partial y^2} \right)^2, \tag{1.25}$$

where $\nu = 0.27$ is Poisson's ratio. The total stored energy W is equal to the maximum kinetic energy, which can be calculated in the following way:

$$W_{\text{kin}} = \frac{\Omega_{\text{m}}^2 \rho}{2} \int dV w(x, y)^2. \tag{1.26}$$

On the right hand side of Figure 1.20 we plot the normalized curvature as calculated via $|(\partial_u^2 + \partial_v^2) w(x, y)|/W^{-1/2}$ of mode A and superimpose the curvature of the fundamental mode of an unperforated square SiN membrane with a side length $l = a$. As expected, the latter experiences strong bending at its edges, exhibiting curvatures almost two order of magnitude larger than the maximum value of mode A.

When calculating the quality factors for the two cases, the comparably large integration domain of the defect mode does not outweigh its reduced curvature. In other words, our simulations predict much higher Q-factors for the defect modes than for those of the square membrane. In Figure 1.21 we show the simulated quality factors, assuming $Q_{\text{int}} = 3750$ [50], and the measured quality factors. Normalized as Qh/a^2 the simulations and the data compare very favourably for all five defect modes and more than 30 samples with $h = 66\,\text{nm}$. We only find a significant discrepancy for mode D, which we attribute to phonon-tunneling loss. This is reasonable since our simulations reveal that mode D exhibits the largest displacement near the silicon frame due to

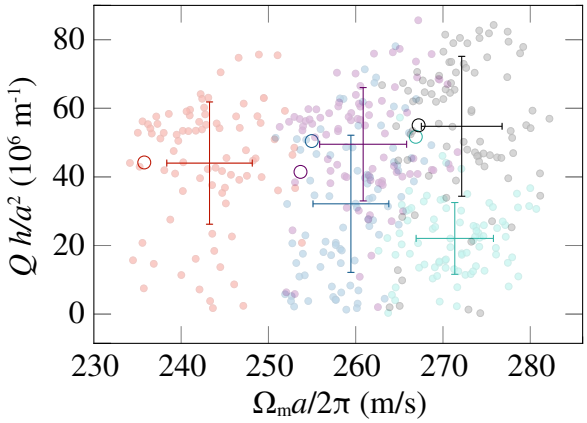

Figure 1.21: Comparison between data and simulation. We compile the measured quality factors for defect modes A (red), B (blue), C (purple), D (cyan), and E (black), including different values of a and $h = \{35\,\text{nm}, 66\,\text{nm}, 121\,\text{nm}\}$. The averages of Qh/a^2 and fa for each mode are shown as error bars and are in good agreement with the simulated quality factors (hollow circles). Adapted from [3].

insufficient suppression of the phononic crystal in the y-direction (see Supplementary Information of [3]). Furthermore, we experimentally find the quality factor of mode D to be somewhat sensitive to clamping conditions.

1.5 Applications

1.5.1 Cavity optomechanics

The ultrahigh quality factors and small effective masses of our patterned SiN membranes are useful for a number of interesting applications. The first is quantum cavity optomechanics, where in particular the long thermal coherence times τ hold promising prospects. At room temperature the membranes could be used for ground-state cooling via dynamical backaction (see Appendix A.3.2), since quantum-coherent oscillations of the defect mode E are maintained over ~ 27 cycles within $\tau \approx 5.4\,\mu\text{s}$, according to the estimate for our best device in Section 1.4.2.2. In comparison, the rate at which we read out the membrane motion in an optomechanical cavity is given by the measurement rate [11, 52][11]

$$\Gamma_{\text{meas}} := \frac{4n_c g_0^2}{\kappa}, \tag{1.27}$$

where n_c is the number of photons in the cavity, κ is the cavity linewidth, and g_0 is the single-photon optomechanical coupling rate. g_0 is defined in Equation (A.33), revealing that $\Gamma_{\text{meas}} \propto g_0^2 \propto m_{\text{eff}}^{-1}$. We see that the effective mass m_{eff} should be small in order to get a large measurement rate. For the ng masses reported here, it is possible to achieve $\Gamma_{\text{meas}}/2\pi = 100\,\text{kHz}$ [34], which is greater than the decoherence rate $1/2\tau\pi \approx 29\,\text{kHz}$ by a factor of $C_q = \Gamma_{\text{meas}}\tau \approx 3.4$, also known as the quantum cooperativity C_q (see

[11] For simplicity we assume perfect detection efficiency $\eta \to 1$.

Equation (A.69)). This means that quantum-coherent interaction between the light and the mechanical motion are enabled at room temperature. Cryogenically cooling the membrane prolongs the coherence time and enhances the interaction even more. Our implementation of ground-state cooling with a patterned SiN membrane at cryogenic temperatures is presented in Chapter 2.

Since ground-state cooling via dynamical backaction causes broadening of the mechanical linewidth, in our case from $\sim$ mHz up to several kHz, the low mode density in the bandgap prevents any overlap and thus coupling between different mechanical modes. Indeed, this is an issue when using higher-order modes of SiN membranes without phononic crystal structures, but with comparable $Q \times f$-products [27], for which we expect a mode density of up to $\sim 1\,\mathrm{kHz}^{-1}$ (see Supplementary Information of [3]). Furthermore, the relatively high frequencies of our membranes at around ~ 1 MHz are well above the typical bandwidth of technical noise, often scaling inversely with frequency. In experiments with optical readout this mostly concerns classical laser noise, originating from laser relaxation oscillations, which in our case occurs at around 380 kHz (see Section 2.3.2.2). Without elaborate laser noise filtering in our experiments, membranes with frequencies $\lesssim$ MHz such as trampoline resonators, would likely not be suitable for ground-state cooling.

1.5.2 Optomechanical sensing

In general, nanomechanical resonators are promising platforms for sensing applications owing to the fact that they can be functionalized and thereby coupled to various external fields [53]. Among the many spectacular examples are the detection of capacitive forces as low as a few 10 zN [54], mass spectrometry with single proteins [55], and detection of radiowaves with pV-sensitivity [56]. With this in view, let us now evaluate our ultrahigh-Q SiN membranes in terms of their force sensitivity. As described in [57] a classical limit to the force detection is set by the force noise power spectral density due to the fluctuation dissipation theorem, which is given in Equation (A.13). Assuming a membrane temperature of $T = 4.2$ K, our best device could reach $S_{FF}^{1/2} \approx 5.5\,\mathrm{aN}/\sqrt{\mathrm{Hz}}$, far below the pN sensitivities typical for atomic force microscopes. We plan to improve upon this result by reducing the effective mass of the defect modes, which can be done by embedding a trampoline or a string geometry in the center. As shown in Figure 1.22 these types of devices have been fabricated and are currently being studied [58]. While still in a preliminary stage, displacement measurements of the string-like defect show a phononic bandgap and localized modes with up to $Q \times f \approx 2 \times 10^{14}$ Hz. Simulations predict an effective mass of $m_{\mathrm{eff}} \approx 250$ pg [58,59], which is about an order of magnitude lower than the masses reported in Section 1.3.2.2.

Finally, we note that soft clamping has recently been utilized in one-dimensional SiN resonators [60]. Here it is used in combination with strain engineering; a nanobeam with phononic crystal is tapered at the defect creating significantly enhanced local stress. Remarkably, this approach leads to $Q \times f$-products exceeding 10^{15} Hz, which are the highest values so far reported at room temperature.

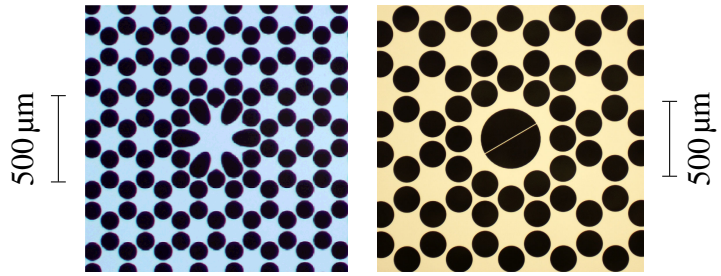

Figure 1.22: Modifications to the defect to reduce effective masses. Left: Micrograph of a trampoline-like defect geometry in a patterned SiN membrane. Right: Micrograph of a SiN membrane in which a string with a width of 1 µm is embedded in the defect. Adapted from [3].

1.6 Conclusion

To sum up, we have developed SiN membranes with phononic crystal patterns and localized mechanical modes around a central defect, which were characterized using a raster-scan interferometer. We have identifed the displacement patterns of the modes and performed ringdown measurements, revealing ultrahigh quality factors of $Q > 10^8$ at room temperature. These exceptional values were attributed to the soft clamping of the modes in good agreement with an analytical model and finite-element simulations. Our membranes are excellent candidates for cavity optomechanics and sensing applications.

Chapter 2

Radiation pressure cooling of silicon nitride membranes

2.1 Introduction

The momentum transfer of light onto mechanical objects upon reflection, generally referred to as radiation pressure, was first experimentally demonstrated in the beginning of the 1900s [61, 62]. In one of the two pioneering experiments of that time, a device known as a Nichols radiometer was used, which in essence consisted of a torsion head with two small mirrors. Reflecting a focused light beam off the mirrors, the device underwent a small rotation, confirming theoretical predictions about the magnitude of radiation pressure remarkably well. More than half a century later in 1967, Braginsky and Manukin introduced the idea that radiation pressure can cause friction on a movable mirror in a Fabry-Pérot cavity [63]. They realized that the intra-cavity light field and the mechanical motion of the mirror can couple via radiation pressure and due to the shift of the cavity resonance frequency from the displacement. This dispersive coupling, in conjunction with a retardation of the force given by the photon lifetime in the cavity, leads to an effect known as dynamical backaction, enabling optical control over the mirror motion (see Appendix A.3). The effect was experimentally verified soon after [64].

Braginsky and Manukin's work laid the foundation for an exciting new research discipline called cavity optomechanics [10]. The field gained considerable interest after the turn of the millennium, when micro- and nanofabricated mechanical devices became widely accessible, which have small effective masses and are therefore particularly susceptible to tiny forces such as radiation pressure. Researchers used these devices to demonstrate significant optical cooling via dynamical backaction [65–67], and achieved a breakthrough when the quantum ground state of motion was reached [12, 13].[1] This was different from motional ground-state cooling of trapped ions presented before [69] since the fabricated mechanical resonators were comparably large in size and made of many millions of atoms. Exploring the quantum behavior of macroscopic objects constitutes a subject of fundamental research and a motivation behind optomechanics.

[1] Ground-state cooling of a mechanical resonator was also achieved via cryogenic refrigeration [68].

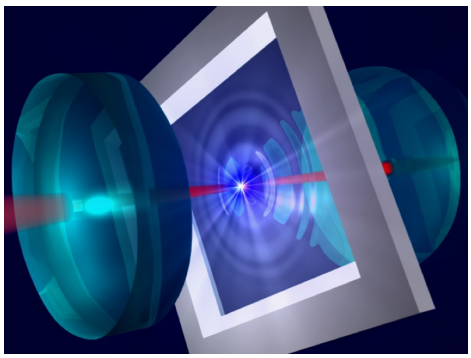

Figure 2.1: Artistic rendering of a MiM system. A SiN membrane is placed between the two mirrors of an optical cavity enabling a coupling between the intra-cavity light field and the mechanical motion via radiation pressure. Reproduced from [84]. Credit: J. Sankey/Yale University.

Apart from basic research, efforts in cavity optomechanics aim to advance metrology, most notably in regard to gravitational wave detection. This is because table-top experiments with small mechanical resonators and large-scale gravitational wave interferometers both approach a fundamental sensitivity limit of displacement detection, known as the standard quantum limit. This limit is set by radiation pressure backaction, originating from quantum fluctuations in light or, put differently, the momentum transfer of photons randomly impinging on the mechanical resonator. Direct evidence of this phenomenon has been found in [70, 71] and in our work discussed in this chapter. Studying the behavior of radiation pressure backaction can lead to the development of evading techniques, enabling position measurements with unprecedented sensitivity. This has been demonstrated in the microwave and optical domain, for example, using two-tone measurements [72, 73], collective mechanical modes [74], and a hybrid spin-optomechanical system [35].

Among the many different platforms in cavity optomechanics, the membrane-in-the-middle (MiM) system has gained much attention in the community ever since it was first introduced in 2008 [75]. The idea is to place a thin (w.r.t. the wavelength) movable membrane in between the two fixed mirrors of a Fabry-Pérot cavity (see Figure 2.1), such that the membrane moves relative to the intensity profile of the standing wave. The response of the dielectric membrane material to the optical field, and vice versa, gives rise to optomechanical coupling, the strength of which can be tuned via the membrane position in the standing wave. A popular choice of membrane material is SiN, facilitating excellent mechanical properties as well as low optical loss [18,76]. The latter enables the use of high-finesse optical cavities to enhance the interaction. Using SiN membranes in a MiM system, different research groups have demonstrated ground-state cooling [77, 78], ponderomotive squeezing [34, 79], quadratic coupling [80], and enhanced coupling with multiple membranes [81, 82], as well as high-contrast gratings [83].

At Quantop, the MiM approach has been implemented since 2012 and has led to a number of promising achievements. For example, in [34] significant squeezing of multiple mechanical modes of a square SiN membrane was reported. The finding is a clear quantum signature, evidencing that the radiation pressure backaction force on

the membrane dominates the thermal force for several modes. In another experiment, quantum backaction evasion in a hybrid spin-optomechanical system was realized [35], in which the motion of a SiN membrane inside a cavity is measured in the negative-mass reference frame of the collective spin of an atomic ensemble. This approach may improve the sensitivity of gravitational wave detectors [85] and paves the way towards entanglement of macroscopic hybrid systems [86]. It should be noted that our optomechanical systems are designed in close collaboration with researchers from SLAB, who have recently prepared a mode of a SiN membrane in the ground state using feedback cooling [87]. This cooling technique is based on an electronic feedback loop which utilizes the information from continuous displacement measurements to control the power of a strong laser beam exerting radiation pressure onto the membrane to counteract its motion.

This chapter deals with the implementation of an ultrahigh-Q SiN membrane in an optical cavity to perform radiation pressure cooling via dynamical backaction to the ground state and Raman sideband thermometry of the mechanical motion. In Section 2.2 we present our MiM system and characterize its key optomechanical properties. Then, we proceed by discussing our heterodyne setup used to determine the phonon occupancy via sideband thermometry and show data of several cooling experiments in Section 2.3. Finally, two future perspectives are considered in Section 2.4 and we conclude this chapter in Section 2.5.

2.2 Membrane in the middle

2.2.1 Background

Before presenting our experiment, we want to discuss the idea behind the MiM approach by providing a one-dimensional theoretical description, which captures the essential dynamics. Consider a membrane placed between two mirrors with amplitude transmission coefficients t_1 and t_2, as illustrated on the left side of Figure 2.2. The amplitude reflection of the membrane is denoted r_m and the distances between each mirror and the membrane are L_1 and L_2. For simplicity, we assume the symmetric configuration in which the membrane sits near the center ($L_1 \approx L_2$) and $|t_1|^2 = |t_2|^2$. Using the TMM (see Appendix A.4) we calculate the spectrum of the cavity transmission $T = |E_\mathrm{t}|^2/|E_\mathrm{in}|^2$, where E_in and E_t are the electric fields of the input light and the transmitted light, respectively. As shown on the right hand side of Figure 2.2, we choose typical values for the parameters and a 250 GHz window around the optical frequency $\omega_\mathrm{l}/2\pi = 351.9\,\mathrm{THz}$, or correspondingly the wavelength of $\lambda = 2\pi c/\omega_\mathrm{l} \approx 852\,\mathrm{nm}$. The calculation is done for different values of $|z_\mathrm{m}| \ll L_1, L_2$, where $z_\mathrm{m} = (L_1 - L_2)/2$ is a small displacement from the center. The result reveals a number of sharp cavity resonances periodically shifting in frequency as a function of z_m. The analytical expression for the resonance frequencies, derived in [88, 89], is given by

$$\omega_\mathrm{c}/\mathrm{FSR} = 2\arg(r_\mathrm{m}) + 2\cos^{-1}\left(|r_\mathrm{m}|\cos\left(2kz_\mathrm{m}\right)\right). \tag{2.1}$$

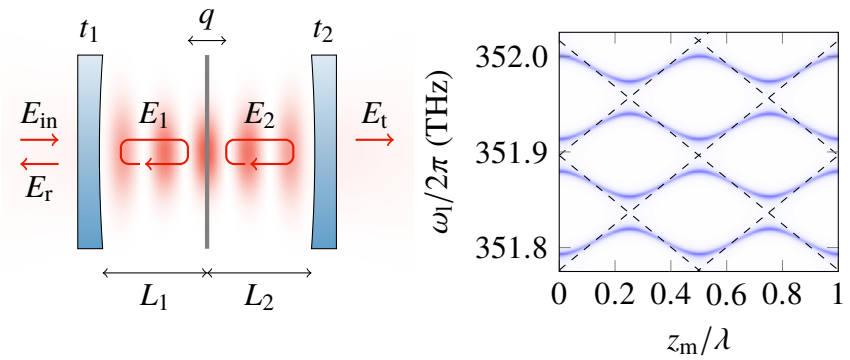

Figure 2.2: Membrane-in-the-middle scheme. Left: Illustration of a movable membrane (thick gray line) between two cavity mirrors, whose transmission coefficients are t_1 and t_2. r_{m} denotes the reflection coefficient and q is the membrane's displacement. Right: Calculated spectrum of the cavity transmission, where large values are shown in blue, as a function of membrane displacement from the center $z_{\text{m}} = (L_1 - L_2)/2$. We set $|r_{\text{m}}|^2 = 40\,\%$, $|t_1|^2 = |t_2|^2 = 20\,\%$, and $L_1 = L_2 = 1.25\,\text{mm}$. Dashed black lines indicate resonances of the two subcavities separated by the membrane.

Here $\text{FSR} = c/2(L_1 + L_2)$ is the free spectral range of the cavity without a membrane and $k = 2\pi/\lambda$. The inverse cosine in the last term is multivalued and thereby accounts for all longitudinal modes of the cavity. Now, from Equation (2.1) the single-photon optomechanical coupling rate $g_0 = q_{\text{zp}}\partial\omega_{\text{c}}/\partial z_{\text{m}}$ is readily derived, quantifying the interaction strength between the light and mechanical motion. q_{zp} denotes the zero-point fluctuations of the membrane (see Equation (A.21)), describing the rms displacement at the motional ground state. The absolute value of g_0 is maximal at $z_{\text{m}} = (2m - 1)\lambda/8$, where m is an integer, and reads

$$\max(|g_0|) = 4\,\text{FSR}\, q_{\text{zp}} k |r_{\text{m}}|. \tag{2.2}$$

An interesting feature of the MiM system compared to the canonical case, i.e., a cavity with a moving end-mirror (see Appendix A.3), is that g_0 is non-linear in z_{m}. Depending on the longitudinal mode and z_{m}, it can vanish[2] and have different signs. To understand this better, it is instructive to view the system from the following perspective: The membrane separates two subcavities, each denoted by the index $i = 1, 2$. Their respective resonance frequencies are $\omega_i/2\pi = c(m_i - 1/2)/2L_i$, where m_i is an integer from which we subtract $1/2$ to account for a $\pi-$phase shift of the light upon reflection from the mirrors of the cavity during one round-trip. The linear functions ω_i are plotted in Figure 2.2 and are reproduced by Equation (2.1) for $|r_{\text{m}}| = 1$. For $|r_{\text{m}}| < 1$ we get a coupling between the electric fields in the two subcavites E_1 and E_2, as manifested by avoided crossings in the spectrum. When $|g_0|$ is maximal we have $\omega_{\text{c}} = \omega_i$, indicating that all the intra-cavity field is concentrated in only one of the two subcavities. The static radiation pressure force onto the membrane is given by

$$F_{\text{RP}} = \frac{2|r_{\text{m}}|^2}{c}\left(|E_1|^2 - |E_2|^2\right), \tag{2.3}$$

[2]At the extrema of ω_{c}, we get $g_0 = 0$ and a finite quadratic coupling $\propto \partial^2\omega_{\text{c}}/\partial z_{\text{m}}^2$. This may be utilized to directly read out the phonon number state [90].

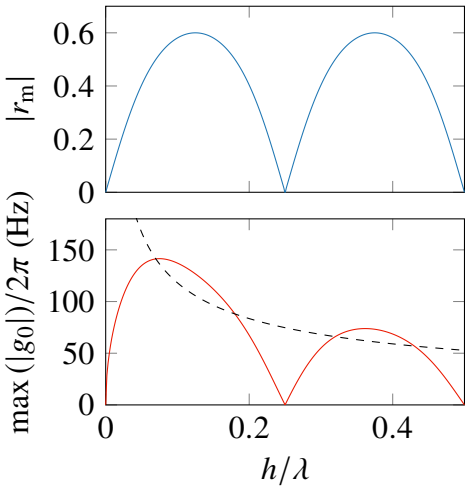

Figure 2.3: Membrane thickness dependence of the optomechanical coupling. Top: Magnitude of membrane reflection coefficient r_m. Bottom: Maximum single-photon coupling rate g_0 for a MiM system (red solid line) as functions of membrane thickness h, calculated using $n = 2.0$, $\lambda = 852\,\text{nm}$, and $L_1 + L_2 = 2.5\,\text{mm}$. The zero-point fluctuation was assumed to be $q_{zp} = 1\,\text{fm}$ at $h = 60\,\text{nm}$. For the same set of parameters the dashed line shows the coupling rate $\tilde{g}_0$ of an optomechanical system with a moving end mirror.

meaning that $g_0 \propto F_{RP}$ is negative if the powers of the two circulating fields are $|E_1|^2 < |E_2|^2$, positive if $|E_1|^2 > |E_2|^2$, and zero if $|E_1|^2 = |E_2|^2$. It should be noted that the sign of g_0 has no impact on the effects of the optomechanical interaction considered here and derived in Appendix A.3 since they only depend on the square of $g = \alpha g_0$, where α is the coherent amplitude of the total intra-cavity field.[3]

Let us now assume that the membrane is a thin dielectric film with thickness h and refractive index n. The following expression for r_m is found via the TMM [91]:

$$r_m = \frac{(n^2 - 1)\sin(knh)}{2in\cos(knh) + (n^2 + 1)\sin(knh)}. \tag{2.4}$$

With r_m expressed this way, we see that the periodic frequency shifts in Equation (2.1) can also be understood in terms of the dielectric response of the membrane material, as mentioned in the introduction of this chapter. The electric fields E_1 and E_2 polarize the membrane material, reducing the total electric field, and thus the energy stored in the cavity. Accordingly, minima and maxima of the frequency shifts correspond to the cases in which the membrane position coincides with an antinode (large electric fields) and node (small electric fields) of the standing wave, respectively.

In Figure 2.3 we plot the magnitude of r_m for the case of a SiN membrane with $n = 2.0$ as a function of h. We also show the maximum coupling rate $\max(|g_0|) \propto |r_m|$ given by Equation (2.2). Notice that here the scaling of $q_{zp} \propto 1/\sqrt{m_{eff}} \propto 1/\sqrt{h}$, where m_{eff} is the membrane's effective mass, is taken into account. Assuming a value of $q_{zp} = 1\,\text{fm}$ typical for a mm-size, square membrane with a thickness of $h = 60\,\text{nm}$, we

[3]See, for example, the optical damping and optical spring effect in Equations (A.50) and (A.51).

can directly compare the coupling in a MiM system to that of an empty cavity with the same length but a moving end mirror (see Appendix A.3.1), i.e., $\tilde{g}_0 = q_{\mathrm{zp}}\omega_{\mathrm{c}}/(L_1 + L_2)$. As can be seen, the two coupling rates are similar around the maxima of $|r_{\mathrm{m}}|$ and the coupling of the MiM system can even be slightly larger. By calculating the ratio

$$\frac{\max\left(|g_0|\right)}{\tilde{g}_0} = 2|r_{\mathrm{m}}|, \tag{2.5}$$

where Equation (2.2) was used, we see that this is the case for $|r_{\mathrm{m}}| > 0.5$.

When comparing the two systems, it is also important to bring forward an advantage of the MiM approach in relation to the following technical challenge: in a canonical system the end mirror is not only required to have good mechanical properties but also a high reflectance that enables a high-finesse cavity in order to facilitate a strong optomechanical interaction. Although remarkable progress has been made to realize such an end mirror, for example, by attaching a high-reflectivity mirror pad to a resonator [92, 93] and using high-contrast gratings [94], as well as photonic crystals [95, 96] in SiN membranes, the implementation is arguably difficult and sometimes compromises the mechanical quality factor. On the other hand, in a MiM system the two requirements are associated with separate elements. One can simply use two commercially available mirrors with low-loss dielectric coatings in combination with a high-Q SiN membrane such as those presented in Section 1.3 that have only moderate reflectance. This greatly benefits the overall performance and, among other things, explains the growing interest in MiM systems within the field.

We have so far only analyzed the symmetric configuration of the MiM system. However, in our experimental realization, detailed in the following section, $|t_1|^2 \neq |t_2|^2$ and $L_1 \neq L_2$. Consequently, not only the cavity frequency ω_{c} but also the linewidth κ and total transmission $|t|^2$ are modulated as a function of the membrane position because the two subcavities have different optical properties. We will address this feature in Section 2.2.3.4.

2.2.2 Experimental realization

2.2.2.1 Sample holder design

Over several years, our group has developed sample holders to implement MiM systems in liquid-helium cryogenic environments, with design iterations for different types of membranes and mirrors. In each design, particular importance is placed on passive stability and good thermal contact of the membrane to the cryostat cold finger. For instance, in previous work of our group [34] this is realized by pressing the two mirrors firmly against the membrane chip and the surrounding copper pieces using small springs. Note that this is possible without compromising the mechanical quality factor since a phononic bandgap shield in the membrane chip is used that suppresses phonon tunneling loss. Indeed, without such a shield the chip needs to be mounted more delicately to avoid disturbing the performance of the membrane, for example, by using small dabs of glue on the corners of the chip [88].

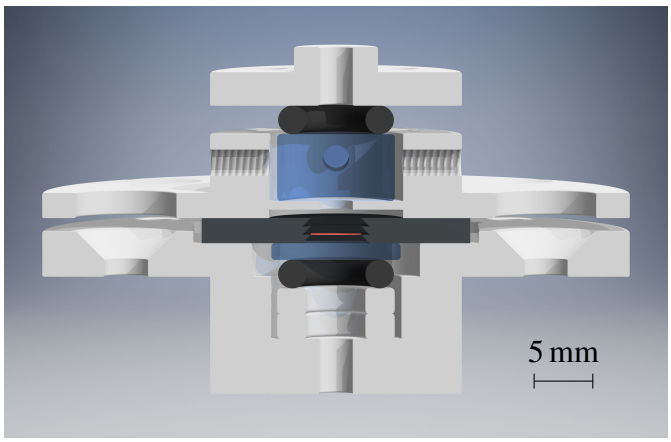

Figure 2.4: 3D rendering of the cavity sample holder. The silicon frame holding a 20-nm-thick SiN membrane (red) is pressed against a flat outcoupling mirror (blue, bottom). Two silicon spacers and a copper piece define the distance to the curved mirror (blue, top). Both mirrors are held in place by rubber o-rings that allow all copper pieces (gray) to be clamped together tightly with screws. The copper piece shown at the bottom is in direct contact to the cryostat cold finger at $T = 4.2\,\mathrm{K}$.

In this experiment we follow the approach of a tightly clamped sample holder. As shown in Figure 2.4, our design consists of a stack of two silicon spacers and the membrane chip placed in between two copper pieces, each accommodating a high reflective mirror. The copper part at the bottom is clamped directly onto the cold finger. The mirrors are held in place by o-rings which are slightly compressed when bolting together the copper parts. The larger mirror on the top has a radius of curvature of $R_1 = 25\,\mathrm{mm}$ while the smaller mirror at the bottom is flat with $R_2 = \infty$. This mirror arrangement forms a plano-concave cavity with a length of $L := L_1 + L_2 \approx 2.5\,\mathrm{mm}$ which fulfils the stability condition [97]

$$0 \leq \left(1 - \frac{L}{R_1}\right)\left(1 - \frac{L}{R_2}\right) \leq 1. \tag{2.6}$$

The highly-reflective surface of the flat mirror is directly pressed against the membrane chip, defining the distance between the membrane and the flat mirror to be $L_2 \approx 500\,\mu\mathrm{m}$, and minimizing tilt between the two.

2.2.2.2 Optical setup and cavity alignment

The sample holder is placed inside a liquid-helium flow cryostat[4] with a cold finger at a temperature of $T = 4.2\,\mathrm{K}$ and a vacuum pressure of $< 10^{-6}$mbar. The optical setup around the cryostat is illustrated in Figure 2.5. We use light from a Ti-sapphire laser[5] at a wavelength of $\lambda = 852\,\mathrm{nm}$ and send it through a fiber-based electro-optic modulator (EOM), a 70:30 BS and a lens. Then, the light partly reflects from the cavity and is analyzed by an avalanche photodetector (APD)[6]. Transmitted light is detected

[4]Janis ST-100 Optical Cryostat
[5]M Squared SolsTiS 10 W PSX-R
[6]Thorlabs APD430A

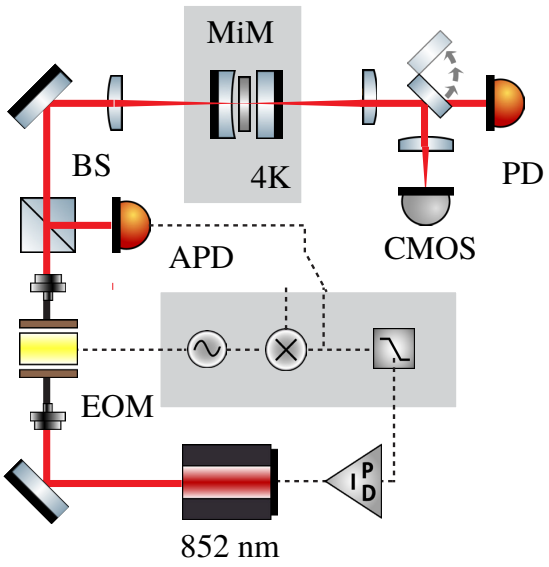

Figure 2.5: Illustration of the optical setup around the MiM system. We couple laser light at a wavelength of $\lambda = 852\,\text{nm}$ into the MiM cavity. The latter is placed in a cryostat at a temperature of $T = 4.2\,\text{K}$. Reflected light from the cavity is detected by an APD whose signal is used to stabilize the laser frequency to the cavity using slope locking or the PDH technique. In transmission we can directly detect the light with a photodetector (PD) or insert a mirror on a flip-mount to image the membrane onto a CMOS camera.

by another photodetector, while a mirror on a flip-mount can be inserted to image the mode profile and the membrane onto a CMOS camera.

We couple light into the cavity by mode matching the input beam to the fundamental transverse cavity mode TEM_{00}, whose beam waist w_0 (radius) is set by the fact that the optical wavefronts must match the radii of curvature of the mirrors. Using the properties of Gaussian beams [97] the following expression is found:

$$w_0^2 = \frac{\lambda L}{\pi}\sqrt{\frac{R_1}{L} - 1}, \tag{2.7}$$

which for our parameters results in $w_0 \approx 45\,\mu\text{m}$. In the experiment we obtain this waist by focusing a collimated beam with a beam diameter of 2.4 mm using a lens with a focal length of 200 mm onto the flat mirror. The mode matching efficiency ϵ is quantified by determining the cavity transmission of different transverse modes that are identified by means of CMOS camera. Scanning the laser frequency over these resonances while detecting the transmitted light using a photodetector we measure the peak transmission of the ten brightest higher-order modes and compare them to the transmission of the TEM_{00} mode. In an exemplary measurement, shown on the left hand side of Figure 2.6, the TEM_{00} mode accounts for $\epsilon \approx 92\,\%$ of the total transmitted light. It should be noted that ϵ is not a critical parameter in our experiment, since we can always compensate for a low mode matching efficiency by increasing the input power.

The radius of the laser spot on the membrane is approximately equal to w_0. This is a valid assumption because the Rayleigh length $z_\text{R} = \pi w_0^2/\lambda \approx 7.5\,\text{mm}$ is much larger

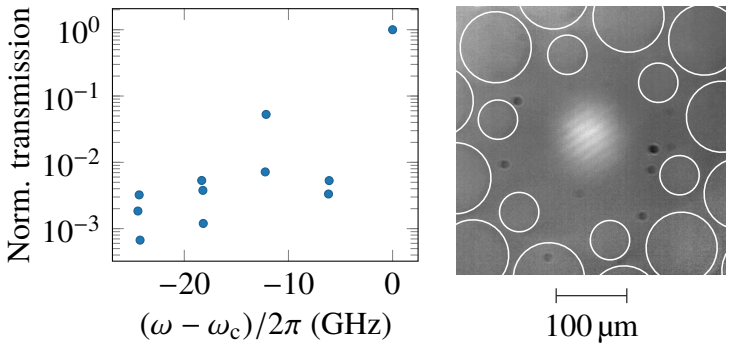

Figure 2.6: Cavity mode matching and spot alignment. Left: Normalized peak cavity transmission of higher-order transverse cavity modes normalized to the peak transmission of the fundamental mode, from which we extract a mode matching efficiency of $\epsilon \approx 92\,\%$. Right: Microscope image showing the focused laser beam aligned to the central defect. The membrane edges are traced with white lines. Black dots are due to small dirt particles attached to the imaging lenses.

than the distance between membrane and flat mirror $L_2 = 500\,\mu\text{m}$. To achieve maximal optomechanical coupling to the fundamental defect mode of the membrane, the cavity mode should be aligned to the center of the defect, where the displacement is maximal. For this reason, we carefully adjust the horizontal position of the curved mirror until the cavity mode is found near the optimal position, as shown in the microscope image on the right side of Figure 2.6. Notice that in contrast to the membranes introduced in Section 1.3 we use a slightly modified design of the pattern around the defect with six smaller holes added to shift the frequency of the fundamental defect mode towards to the center of the bandgap [87].

2.2.2.3 Optical losses

As a next step, we want to characterize the optical losses of our MiM system. A particularly important quantity in this context is the cavity finesse $\mathcal{F}$ that is related to the FSR and the cavity linewidth κ in the following way [98]:

$$\mathcal{F} := 2\pi \frac{\text{FSR}}{\kappa} \approx \frac{2\pi}{\delta}. \tag{2.8}$$

In the last expression, $\delta \ll 1$ denotes the fraction of photons lost per round-trip in the cavity including several different contributions:

$$\delta = |t_1|^2 + \delta_1 + |t_2|^2 + \delta_2 + \delta_\text{m}. \tag{2.9}$$

Here t_1 and t_2 are the amplitude transmission coefficients of the two mirrors. Scattering and absorption losses are combined into δ_1, δ_2, and δ_m for the two mirrors and the membrane, respectively.

Let us now distinguish the different contributions and first concentrate on the losses of the two mirrors. We assemble an empty cavity, that is, a cavity without a membrane, and determine its linewidth κ by scanning the laser frequency over the resonance,

detecting the transmitted light, and extracting the full width at half maximum (FWHM) from a fit to the Lorentzian peak in the signal. Sidebands around the peak, generated at a well-known frequency via the EOM, serve as a frequency reference in the signal. Furthermore, the FSR = $(\omega_{c,m} - \omega_{c,m+1})/2\pi$ is measured by finding the frequencies of adjacent longitudinal modes, denoted here by the integers m and $m+1$ in the subscripts. The two measurements yield $\kappa/2\pi = 2.70(3)$ MHz and FSR = 60 GHz, from which we calculate that $\mathcal{F} = 2.22(2) \times 10^4$ and $|t_1|^2 + |t_2|^2 = 277(3) \times 10^{-6}$, assuming typical values of $\delta_1 = \delta_2 = 3 \times 10^{-6}$ [88, 99]. This is in fair agreement with transmission measurements of mirrors with the same coatings, where we find that $|t_1|^2 \approx 20 \times 10^{-6}$ for the curved mirror and $|t_2|^2 \approx 230 \times 10^{-6}$ for the flat mirror. Notice that with the curved mirror serving as an incoupler, the majority of intra-cavity photons exit the cavity in transmission, which is quantified by the outcoupling efficiency

$$\eta_c \coloneqq \frac{|t_2|^2}{\delta}. \tag{2.10}$$

For the parameters above we get $\eta_c \approx 93\,\%$, meaning that in order to achieve a high detection efficiency of the intra-cavity field, it is preferable to detect the transmitted light instead of the reflected light from the cavity.

Coming back to the full MiM system, we proceed by estimating the last term in Equation (2.9), namely the optical losses per round-trip δ_m due to the membrane. In many optomechanical experiments with SiN membranes δ_m is found to be negligibly small with reported values on the order of a few 1×10^{-6} at a similar wavelength [76,99]. This is because of the fact that SiN has a very low optical absorption. However, in our case we also need to consider scattering losses, presumably due to diffraction at the sharp edges of the phononic crystal structure around the defect. Recall that the cavity mode with a spot radius of $w_0 = 45\,\mu$m is aligned to the center of the defect. A crude estimate assuming a circular aperture around the center with a diameter of 103 µm, i.e., the distance between the edges of two opposing small holes, yields $\delta_m \approx 10 \times 10^{-6}$. We are lead to conclude that if the cavity mode is correctly aligned to the center of the defect, the scattering losses δ_m are much smaller than δ, rendering all the aforementioned parameters virtually unaffected.

It should be noted that the discussion of optical losses in this section is simplified, since it does not take into account any dependences on the membrane position z_m. Indeed, as mentioned before κ varies with z_m, in our case by $\sim 20\,\%$, which we measure in Section 2.2.3.4. Consequently, the FSR, $\mathcal{F}$ and η_c are also changing. Nonetheless, we find that the average values agree well with those calculated here.

2.2.2.4 Active stabilization

The optomechanical cavity is subject to acoustic noise and temperature variations from the environment causing the cavity length L and thus the resonance frequency ω_c to fluctuate over time. In order to maintain a given cavity detuning $\Delta \coloneqq \omega_l - \omega_c$ we need to actively stabilize the laser frequency ω_l. There are different, well-established techniques to realize this and in this section we will present the two used in our experiment.

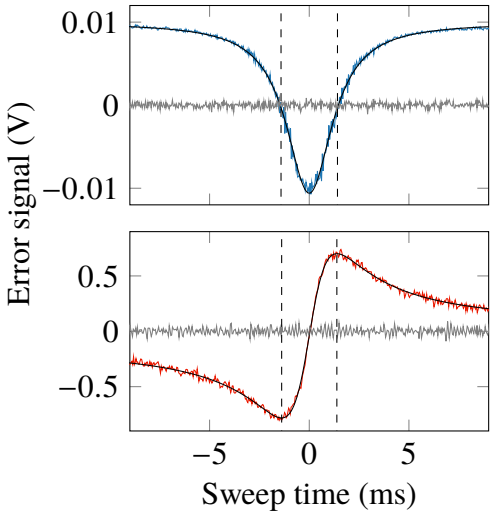

Figure 2.7: Laser frequency stabilization to the cavity resonance. Error signals for slope locking (top) and PDH locking (bottom) when sweeping the laser frequency over the cavity resonance (colored lines). From fits (solid black lines) we extract the FWHM of the resonance, indicated here in units of time with vertical dashed black lines. Measured error signals from the locked cavity are shown in gray.

As mentioned before we detect the reflected light from the cavity with an APD. The photocurrent from the APD is proportional to the absolute square of the amplitude reflection coefficient $r_c(\Delta)$ of the cavity. With the previously introduced parameters we find that

$$r_c(\Delta) = \frac{E_r}{E_{in}} = 1 - \frac{\eta_c \kappa}{\frac{\kappa}{2} - i\Delta}, \tag{2.11}$$

where we assume a perfect incoupling efficiency $\epsilon = 1$. The photocurrent is used to generate an error signal $e_{slope} \propto c - |r_c(\Delta)|^2$, where the constant c is the setpoint, and stabilize the laser frequency near the slope of the cavity with $|\Delta| \approx \kappa/2$ (reflection locking). This is achieved by feeding the error signal to a proportional-integral controller that controls the piezo of the laser etalon. As an alternative to this, we can lock the laser close to the cavity resonance frequency ($\Delta \approx 0$) by generating a Pound-Drever-Hall (PDH) error signal [100], where the input light is phase-modulated via the EOM at a frequency of $\Omega_{pdh} = 32.5\,\text{MHz} \gg \kappa/2\pi$. As illustrated in Figure 2.5, we then demodulate the photocurrent from the APD at the same frequency, low-pass filter it, and adjust the phase difference between the EOM drive and the signal to be 90°. The error signal, derived in [100], is an odd function around $\Delta = 0$ and has the following form:

$$e_{pdh} \propto c - \text{Im}\left(r_c(\Delta) r_c(\Delta + \Omega_{pdh})^* - r_c(\Delta)^* r_c(\Delta - \Omega_{pdh})\right), \tag{2.12}$$

Figure 2.7 shows measurements and fits of e_{slope} and e_{pdh} when sweeping the laser over the cavity resonance. In the case of the PDH error signal the fit is used to determine the linewidth $\kappa/2\pi = 2.91(1)\,\text{MHz}$. We can also find the detuning $\Delta/2\pi = 42.1(291)\,\text{kHz}$ when the laser is locked to the cavity. All error signals shown here are low-pass filtered with a bandwidth of 4.9 kHz in order to strongly suppress high-frequency noise in the feedback loop.

In principle, using the two locking techniques interchangeably we can stabilize the laser frequency to the resonance with an arbitrary detuning, provided that we correctly adjust the setpoint c and the gain of the feedback. In practice, however, we are limited to the interval between $\Delta \approx -2\kappa$ and $\Delta \approx 0$. Indeed, if the laser frequency is far away from the resonance $|\Delta| \gg \kappa$, the derivatives of the error signals with respect to Δ become too small to maintain the feedback loop, even with maximum gain. Blue detuning from the resonance ($\Delta > 0$) is widely inaccessible in our experiment because here the membrane motion is greatly amplified via dynamical backaction and thereby causes ω_c to widely fluctuate at the mechanical frequency. We find that this is the case even when using the lowest possible optical powers of the input beam set by the sensitivity of the APD.

2.2.3 Characterization of optomechanical parameters

While the laser frequency is locked near the cavity resonance with $\Delta < 0$ we can detect mechanical motion of the patterned SiN membrane inside the cavity using a photodetector in transmission. The membrane used here is 20 nm thick and has its fundamental defect mode at a frequency of $\Omega_m/2\pi \approx 1.275$ MHz. In the following we present data to characterize various optomechanical parameters such as the quality factor Q, the coupling rate g_0, and the quantum cooperativity C_q.

2.2.3.1 Quality factor

The quality factor Q of the defect mode is measured via ringdown fitting. The procedure for this is the same as that described in Section 1.2.1.4. We resonantly drive the membrane mode using a PZT placed next to the sample holder in the cryostat and fit an exponential function to the decay of the amplitude after switching off the drive. When implementing this with the membrane placed inside the MiM cavity, it is important to consider that dynamical backaction can modify the mechanical linewidth $\Gamma_m = \Omega_m/Q$ and thereby the ringdown time, as described in Appendix A.3.2. We minimize this effect by tuning the laser wavelength to ~ 750 nm where both cavity mirrors have low reflectance and the finesse is on the order of unity. This means that the cavity linewidth $\kappa \gg |\Delta \pm \Omega_m|$, resulting in the optical damping $\Gamma_{opt} \approx 0$ according to Equation (A.50). To verify this experimentally, we compare ringdown measurements at positive and negative detunings Δ and find that in the two cases Q varies by less than 10 %.

With the cold finger of the cryostat cooled to a temperature of $T = 4.2$ K we measure an average quality factor as large as $Q = 934(4) \times 10^6$. An example ringdown measurement is shown in Figure 2.8. Furthermore, we get $Qf = 1.191(5) \times 10^{15}$ Hz which exceeds the expected value based on our previous results presented in Section 1.4 by about a factor of two, taking into account the reduced membrane thickness and assuming a 2.5-fold increase of Q compared to the room temperature measurement. At the moment, we are unsure what causes this discrepancy. We suspect that the modified defect design reduces the curvature and thus the material loss even further than before.

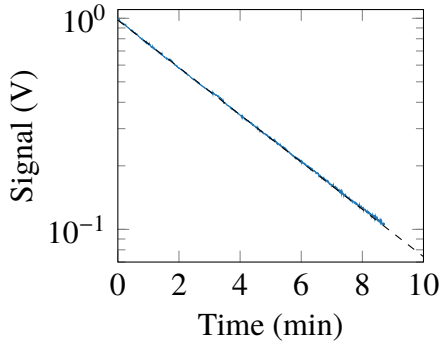

Figure 2.8: Quality factor of the patterned SiN membrane mounted in the cavity. We perform ringdown measurements of the fundamental defect mode A at a cold finger temperature of $T = 4.2\,\mathrm{K}$ (blue line) and extract from exponential fits (black dashed line) an average value of $Q = 934(4) \times 10^6$.

2.2.3.2 Optomechanically-induced transparency

As a next step, we want to characterize the optomechanical interaction strength of our MiM system. To this end, we use the following procedure. While stabilizing the laser frequency near the cavity resonance with a given detuning $\Delta < 0$, we perform a frequency-swept phase modulation in the range $\Omega/2\pi = 500\,\mathrm{kHz}...10\,\mathrm{MHz}$ using the EOM at the input of the cavity. The phase modulation results in amplitude modulation of the intra-cavity field, coherently driving the membrane motion via radiation pressure. Near the mechanical resonance $\Omega \approx \Omega_\mathrm{m}$ the membrane motion is driven to a large amplitude and in turn induces phase modulation that interferes with the drive. When probing the cavity in transmission, this interference is visible as a sharp feature in the spectrum on top of the broadband response of the cavity. The effect is commonly referred to as optomechanically induced transparency (OMIT) [101]. In Figure 2.9 we present data of such a measurement, acquired using a vector network analyzer.

In order to find an expression for the signal we employ the linearized Langevin equations presented in Appendix A.3.1. We are interested in the intra-cavity amplitude fluctuations $\delta\hat{X}$, proportional to the amplitude fluctuations $\delta\hat{X}_\mathrm{t}$ at the cavity output (in transmission):

$$\delta\hat{X}_\mathrm{t} = \sqrt{\eta_\mathrm{c}\kappa}\,\delta\hat{X}. \tag{2.13}$$

The light at the cavity input is subject to phase modulation denoted $\delta\hat{Y}^\theta_\mathrm{in}$, while the amplitude fluctuations $\delta\hat{X}^\theta_\mathrm{in}$ are assumed to be zero. The cavity rotates $\delta\hat{Y}^\theta_\mathrm{in}$ by a phase angle θ, meaning that the quadratures fluctuations of the drive in Equations (A.43) and (A.44) are $\delta\hat{X}_\mathrm{in} = -\sin\theta\delta\hat{Y}^\theta_\mathrm{in}$ and $\delta\hat{Y}_\mathrm{in} = \cos\theta\delta\hat{Y}^\theta_\mathrm{in}$. We identify that $\theta = \arg\left(\chi_\mathrm{c}(0)^{-1}\right) = \tan^{-1}(-2\Delta/\kappa)$, where $\chi_\mathrm{c}(\Omega)$ is the cavity susceptibility defined in Equation (A.49). Using trigonometric identities we then get

$$\delta\hat{X}_\mathrm{in} = \frac{2\Delta}{\sqrt{\kappa^2 + 4\Delta^2}}\delta\hat{Y}^\theta_\mathrm{in}, \tag{2.14}$$

$$\delta\hat{Y}_\mathrm{in} = \frac{\kappa}{\sqrt{\kappa^2 + 4\Delta^2}}\delta\hat{Y}^\theta_\mathrm{in}. \tag{2.15}$$

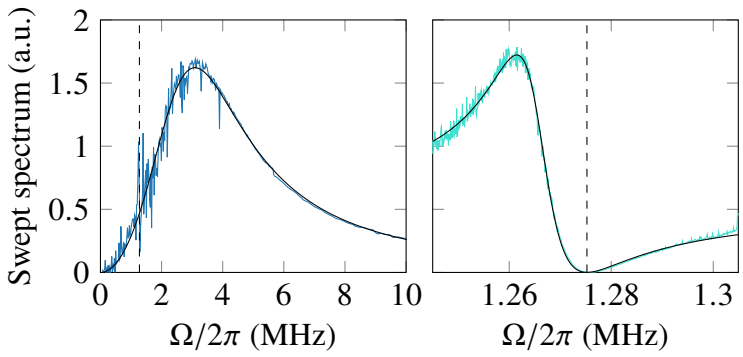

Figure 2.9: Optomechanically induced transparency to quantify the interaction strength. Left: Square magnitude of the cavity response to a phase modulation sweep over a broad frequency range as measured at $T = 4.2\,\mathrm{K}$ (blue) and fitted (black) from which we extract $\kappa/2\pi = 3.97(3)\,\mathrm{MHz}$ and $\Delta/2\pi = -2.37(2)\,\mathrm{MHz}$. Right: The narrow band response around the mechanical mode is then used to determine $\Omega_\mathrm{m}/2\pi = 1.275\,\mathrm{MHz}$ (dashed lines) and $g/2\pi = 148.8(4)\,\mathrm{kHz}$. Data and the fit are shown in cyan and black, respectively.

Next, we solve Equations (A.43–46) for $\delta\hat{X}$, insert Equations (2.14) and (2.15) and find the following expression in agreement with [99, 102]:

$$\delta\hat{X} = \frac{C(\Omega)}{M(\Omega)+1}\delta\hat{Y}^{\theta}_{\mathrm{in}}. \tag{2.16}$$

Here we distinguish the response functions $C(\Omega)$ and $M(\Omega)$ of the cavity and the mechanical mode, respectively. The former is given by

$$C(\Omega) = \sqrt{\frac{(1-\eta_\mathrm{c})\epsilon\kappa}{\kappa^2+4\Delta^2}}\Omega\delta\hat{Y}^{\theta}_{\mathrm{in}}\left(\chi_\mathrm{c}^*(-\Omega)-\chi_\mathrm{c}(\Omega)\right), \tag{2.17}$$

where we included the incoupling efficiency in the driving terms of the Langevin equations, substituting $\kappa \to (1-\eta_\mathrm{c})\epsilon\kappa$ in the numerator. Now $|C(\Omega)|^2$ is used to fit to the square magnitude of the swept spectrum[7] to determine κ and Δ. This is exemplified on the left hand side of Figure 2.9. Afterwards, we perform a second sweep in a narrow window ($\sim 50\,\mathrm{kHz}$) around the mechanical frequency Ω_m, in which $|C(\Omega)|^2$ is approximately constant. These data are fit to $|C(\Omega_\mathrm{m})/(M(\Omega)+1)|^2$, where

$$M(\Omega) = \frac{i\hbar g^2}{q_\mathrm{zp}^2}\chi_\mathrm{m}(\Omega)\left(\chi_\mathrm{c}^*(-\Omega)-\chi_\mathrm{c}(\Omega)\right). \tag{2.18}$$

Here $\chi_\mathrm{m}(\Omega)$ is the mechanical susceptibility defined in Equation (A.15). As shown on the right side of Figure 2.9, we extract the cavity-enhanced coupling rate $g/2\pi = 148.8(4)\,\mathrm{kHz}$ at $\Delta/2\pi = -2.37(2)\,\mathrm{MHz}$. To get $g_0 = g/\alpha$, where α is the real coherent amplitude of the cavity field, we simply measure the power $P_\mathrm{t} \approx 18\,\mu\mathrm{W}$ of the transmitted light and evaluate the number of photons in the cavity $n_\mathrm{c} = \alpha^2 = P_\mathrm{t}/\eta_\mathrm{c}\kappa\hbar\omega_\mathrm{l} \approx 3.3\times10^6$.

[7] We compensate for the detector response, measured independently via a SN spectrum.

This means that $g_0/2\pi \approx 81.5\,\mathrm{Hz}$ in our system, assuming $\lambda = 2\pi c/\omega_\mathrm{l} = 852\,\mathrm{nm}$ and $\eta_\mathrm{c} = 0.93$. For now, we disregard the $< 5\,\%$ modulation of η_c as a function of z_m (see Section 2.2.3.4)

We also calculate the quantum cooperativity C_q; an important figure of merit that compares the strength of the optomechanical interaction to the thermal decoherence rate (see Appendix A.3.3). It reads

$$C_\mathrm{q} = \frac{4g^2}{\kappa\Gamma_\mathrm{m}\bar{n}_\mathrm{th}}, \tag{2.19}$$

derived from the definitions in Equations (1.27) and (A.69). For the phonon occupancy $\bar{n}_\mathrm{th} = k_\mathrm{B}T_\mathrm{m}/\hbar\Omega_\mathrm{m} \approx 1.76 \times 10^5$ we use the membrane's bath temperature of $T_\mathrm{m} \approx 10.4\,\mathrm{K}$, determined in Section 2.3.3. With $\Gamma_\mathrm{m} = \Omega_\mathrm{m}/Q \approx 2\pi\times 1.36\,\mathrm{mHz}$ and the other measured parameters mentioned above, we then get $C_\mathrm{q} = 92.7(8)$. Evidently, this satisfies the condition $C_\mathrm{q} > 1$ by a large margin, suggesting that with our MiM system we should be able to control the membrane motion at the quantum level.

2.2.3.3 Static bistability

The expression for the cavity-enhanced coupling rate $g = \alpha g_0$ suggests that the strength of the optomechanical interaction can be amplified to an arbitrary degree by increasing α. However, in most systems α is limited by an effect known as the static bistability, originating from the constant radiation pressure exerted onto the membrane by the mean intra-cavity field. To see this, let us find the steady state solutions of the Langevin equations. We first take the expectation values of Equations (A.35–37), and identify the mean optical field amplitudes as $\alpha = \langle\hat{a}\rangle$, $\alpha_\mathrm{in} = \langle\hat{a}_\mathrm{in}\rangle$ and the mean displacement $\bar{q} \coloneqq \langle\hat{q}\rangle$. Then, we set all time derivatives to zero, along with the fluctuating term including $\langle\hat{F}_\mathrm{th}\rangle$, which results in

$$\alpha = \frac{\sqrt{(1-\eta_\mathrm{c})\epsilon\kappa}\,\alpha_\mathrm{in}}{\kappa/2 - i\left(\Delta - g_0\bar{q}/q_\mathrm{zp}\right)}, \tag{2.20}$$

$$\bar{q} = -\frac{2q_\mathrm{zp}g_0\alpha^2}{\Omega_\mathrm{m}}. \tag{2.21}$$

In the numerator of Equation (2.20) we replaced $\kappa \to (1-\eta_\mathrm{c})\epsilon\kappa$ to consider the incoupling efficiency in our two-sided cavity, as was done in the last section. Combining Equations (2.20) and (2.21) we get a cubic expression for the intra-cavity photon number $n_\mathrm{c} = \alpha^2$ that has more than two real solutions if $\Delta \geq -\sqrt{3}\kappa/2$ and if the input power $P_\mathrm{in} = \hbar\omega_\mathrm{l}|\alpha_\mathrm{in}|^2$ fulfills [103]

$$P_\mathrm{in} \geq \frac{\hbar\omega_\mathrm{l}\Omega_\mathrm{m}\kappa^2}{6\sqrt{3}(1-\eta_\mathrm{c})\epsilon g_0^2}. \tag{2.22}$$

The regime with multiple solutions is unstable, since small perturbations can cause α and $\bar{q}$ to abruptly alternate between different solutions. In our experiment, this can be observed once the input power exceeds $\sim 500\,\mu\mathrm{W}$. We find that when linearly

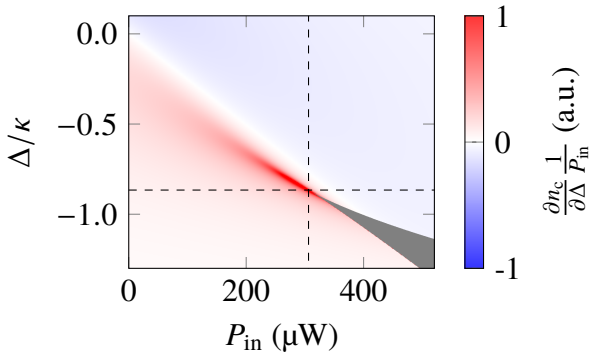

Figure 2.10: Static bistability due to the membrane bridge mode. Calculated derivative of the mean cavity photon number n_c with respect to the detuning Δ normalized by the input power P_{in}, in which the static displacement of the bridge mode with a frequency of $\Omega_m/2\pi = 80.1\,\mathrm{kHz}$ and a coupling $g_0/2\pi \approx 95\,\mathrm{Hz}$ is taken into account. Dashed lines indicate the onset detuning and input power of the static bistability, according to Equation (2.22). The gray shaded area covers the parameter space for which the bistability occurs.

scanning the laser frequency across the cavity resonance, a sudden jump appears on the red-detuned side of the resonance, preventing us from locking the cavity. We presume that the fundamental bridge mode of the entire membrane structure at a frequency of $\Omega_m/2\pi = 80.1\,\mathrm{kHz}$ gives rise to static bistability and determine its coupling rate $g_0/2\pi \approx 95\,\mathrm{Hz}$ via OMIT. Assuming $\eta_c = 0.93$ and $\epsilon = 0.92$, Equation (2.22) yields $P_{in} \gtrsim 306\,\mu\mathrm{W}$. This number is in fair agreement with our observation. In Figure 2.10, we calculate the derivative of n_c with respect to Δ for different P_{in}. This quantity shows that the resonance frequency linearly shifts and the slope on the red-detuned side increases with P_{in} before the bistability sets in. The range of detunings Δ for which the bistability occurs widens when increasing P_{in}.

Before moving on, it should be noted that except in this section we always redefine the detuning so that the shift due to the static displacement $\bar{q}$ is discarded, i.e., $\Delta - g_0\bar{q}/q_{zp} \rightarrow \Delta$. In other words, we always reference the laser frequency to the observed cavity resonance frequency. Furthermore, assuming typical values of $n_c \sim 10^6$ and $q_{zp} \sim 1\,\mathrm{fm}$ Equation (2.21) reveals that the mean displacement $\bar{q} \approx 2\,\mathrm{pm} \ll \lambda$. This means that $\bar{q}$ can be neglected when determining the membrane position z_m with respect to the standing wave, which is especially relevant in the following.

2.2.3.4 Modulation of parameters with membrane position

In Section 2.2.1 we saw that the cavity resonance frequency ω_c of a MiM system is a periodic function of the membrane position z_m and has a period of $\lambda/2$. In order to maximize the coupling rate $g_0 \propto \partial\omega_c/\partial z_m$, it is necessary to control z_m with sub-wavelength precision ($\lesssim 100\,\mathrm{nm}$). Typically, this is done by means of a PZT displacing the membrane chip with respect to the fixed cavity mirrors [76, 91, 104]. In our sample holder we do not include a PZT in such a way and use another technique to adjust g_0. We change the laser wavelength by $\delta\lambda_m \ll \lambda$ and address different longitudinal modes m of

the cavity, each exhibiting a different g_0. It is clear why this is possible by inspection of Equation (2.1), in which the argument of the cosine describing the modulation of ω_c and thus $\partial\omega_c/\partial z_m$ is $2kz_m \propto 1/\lambda$. Now, for each longitudinal mode at $\lambda + \delta\lambda_m$ we map out where the membrane is located in relation to one intensity 'bubble' of the standing wave. This is done by redefining the (relative) membrane position $0 \leq z_m \leq \lambda/2$ using the following modulo operation:

$$z_m \coloneqq L_2 \text{ modulo } (\lambda + \delta\lambda_m)/2. \tag{2.23}$$

Here $z_m = 0$ and $z_m = \lambda/2$ correspond to the membrane sitting at a node of the standing wave, while for $z_m = \lambda/4$ the membrane is at an antinode. We stress that L_2 is fixed in our experiment, meaning that the membrane position with respect to the mirrors is unchanged while we alter z_m via the laser wavelength.

Figure 2.11 shows measurements of the cavity frequency shift $\delta\omega_c$ as a function of z_m. To extract $\delta\omega_c$, we fit a linear function with sinusoidal modulation to the resonance frequencies $\omega_{c,m} = 2\pi c/(\lambda+\delta\lambda_m)$ versus their corresponding longitudinal mode number m. Afterwards, the linear part of the fitted curve, with a slope of $\sim 2\pi$ FSR, is subtracted from the data and the maximum of the residual sine is set to zero [99], resulting in the plot of $\delta\omega_c$ shown in Figure 2.11. Note that the sinusoidal modulation in the fit function is based on Equation (2.1) and constitutes an approximation justified for a low membrane reflectivity $|r_m|$. The latter is indeed fulfilled as $|r_m| \approx 0.213 \ll 1$ according to Equation (2.4) with $\lambda = 852\,\text{nm}$ and $h = 20\,\text{nm}$.

Apart from $\delta\omega_c$, we record at each cavity resonance an OMIT signal (see Section 2.2.3.2) as well as the cavity input and output power in transmission. These measurements reveal the cavity linewidth κ, the peak transmission $|t|^2$, and the coupling rate g_0, as shown in Figure 2.11. The sinusoidal modulations of κ and $|t|^2$ are characteristic features of an asymmetric MiM system owing to the different loss rates of the two subcavities. Note that this also concerns the outcoupling efficiency η_c, defined in Equation (2.10), which is maximal if $|t|^2$ is minimal. We see this in the identity [105]

$$|t|^2 = 4\epsilon\eta_c(1-\eta_c). \tag{2.24}$$

The coupling rate g_0 follows the derivative of the frequency shift as expected and reaches up to $g_0/2\pi = 84.3(2)\,\text{Hz}$. A comparison between the fitted curves to $\delta\omega_c$ and g_0 reveals that $q_{zp} = 2.24(8)\,\text{fm}$ corresponding to an effective mass of $m_{\text{eff}} = 1.31(5)\,\text{ng}$, where we used Equation (A.21). Although a slightly different defect geometry is used here, the effective mass is in fair agreement with that reported in Section 1.3.2.2 ($\sim 5\,\text{ng}$), if we take into account the difference in membrane thickness and accordingly rescale m_{eff} by the thickness ratio $66\,\text{nm}/20\,\text{nm} = 3.3$.

We now want to contrast our findings with the TMM (see Appendix A.4). For simplicity, we neglect all optical losses in the cavity and use the mirror transmission coefficients $|t_1|^2 = 20\times10^{-6}$ and $|t_2|^2 = 275\times10^{-6}$. These values reproduce the average of the modulated linewidth $\bar{\kappa} = \text{FSR}\,(|t_1|^2 + |t_2|^2) \approx 2\pi \times 2.82\,\text{MHz}$ shown in Figure 2.11, where $\text{FSR} = 60\,\text{GHz}$. $\bar{\kappa}$ deviates from the measured linewidth of the empty cavity by less than 5 % (see Section 2.2.2.3). To match the average transmission

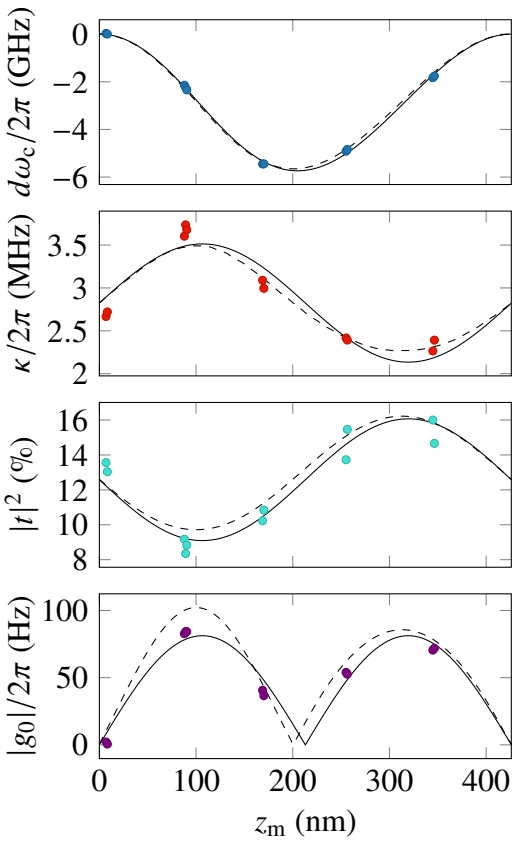

Figure 2.11: Optomechanical cavity parameters versus membrane position. The cavity frequency shift $\delta\omega_c$, cavity linewidth κ, peak transmission $|t|^2$, and single-photon coupling rate g_0 are modulated as a function of relative membrane position z_m and have a periodicity of $\lambda/2$. From sinusoidal fits (black solid lines) to the data (colored dots) we extract the average parameters $\bar{\kappa}/2\pi = 2.82(6)$ MHz and $|\bar{t}|^2 = 12.6(3)$ %, as well as $q_{zp} = 2.24(8)$ fm. The gray dashed lines are calculations based on the TMM. Relative errors of κ and g_0 from the OMIT fits are < 1.5 % and are not shown.

of $|\bar{t}|^2 = 12.6(3)$ % at the average output coupling efficiency of $\bar{\eta}_c \approx 0.93$, we assume $\epsilon = 0.5$. Now, we numerically calculate the cavity transmission spectrum around $\lambda = 852$ nm and track the frequency, the peak transmission as well as the linewidth of a single resonance for different values of the membrane position in the range $z_m = 0...\lambda/2$. The coupling $|g_0|$ is found via the derivative of the resonance frequency with respect to z_m, multiplied by $q_{zp} = 2.24$ fm. As shown in Figure 2.11, the data and the TMM exhibit the same overall behavior. We see that the modulations are not exactly sinusoidal as assumed for the fits. This is particularly evident in the case of $|g_0|$, where the two peaks in the TMM curve are not of equal height.

In order to match the measured values for $\delta\omega_c$ with the TMM we have to set the membrane thickness to ~ 13.6 nm, which is significantly lower than the actual $h \approx 20$ nm. For the latter we expect $\max(|\delta\omega_c|)/2\pi = 2\,\mathrm{FSR}\,|r_m|/\pi \approx 8.14$ GHz according to Equations (2.1) and (2.4), assuming FSR = 60 GHz. This discrepancy can be explained by a small membrane tilt α with respect to the flat mirror. Consider a Gaussian beam with a radius of $w_0 = 45$ µm. At each point across its intensity profile

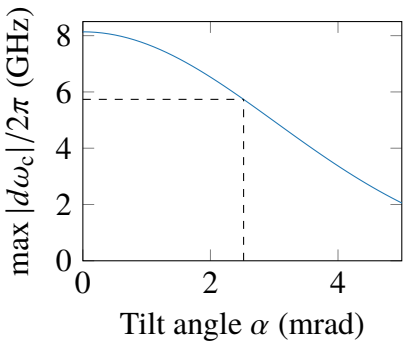

Figure 2.12: Reduced frequency shift due to membrane tilt. Calculated maximal cavity frequency shift as a function of membrane tilt angle α (blue) for a membrane thickness of $h = 20\,\text{nm}$, FSR = 60 GHz, and a beam waist of $w_0 = 45\,\mu\text{m}$. Dashed lines indicate the maximal frequency shift extracted from fits in Figure 2.11, corresponding to $\alpha \approx 2.52\,\text{mrad}$.

along the tilt axis x, where $x = 0$ is the center of the Gaussian, we have a slightly different position $z_m + x \tan\alpha$ with respect to the standing wave, resulting in an x-dependent phase offset of the sinousoidal frequency modulation. Assuming $h = 20\,\text{nm}$, we numerically calculate the total frequency modulation averaged over all points x, where each point is weighted by the Gaussian function. This is repeated for different values of α and shown in Figure 2.12, where we see that the maximum frequency shift is expected to decrease with α. The value $\max(|\delta\omega_c|)/2\pi \approx 5.74\,\text{GHz}$ extracted from the fit to the data in Figure 2.11 is obtained at $\alpha = 2.52\,\text{mrad}$. Such a small tilt corresponds to a height difference of $\alpha l \approx 37.5\,\mu\text{m}$ between two points at opposite ends of the $l \sim 15\,\text{mm}$-wide membrane chip, which proves difficult to avoid when assembling our sample holder. We suspect that this is because of small dirt particles or surface irregularities at the edges of the flat mirror that is pressed against the chip.

2.3 Sideband cooling and thermometry

We will now turn our attention towards sideband cooling of the membrane's fundamental defect mode via dynamical backaction. The basic theory for this is outlined in Appendix A.3.2. In this section, we will first present our optical heterodyne detection setup, in which we reference the light transmitted through the cavity to a LO with a fixed frequency offset, allowing us to distinguish the sidebands induced by the optomechanical interaction and perform Raman sideband thermometry. Afterwards, we demonstrate the cooling and explore the cooling limit set by radiation pressure backaction.

2.3.1 Heterodyne detection

2.3.1.1 Experimental setup

Consider the illustration in Figure 2.13 showing our heterodyne detection setup. Compared to the setup presented in the previous section, we add a number of components; in

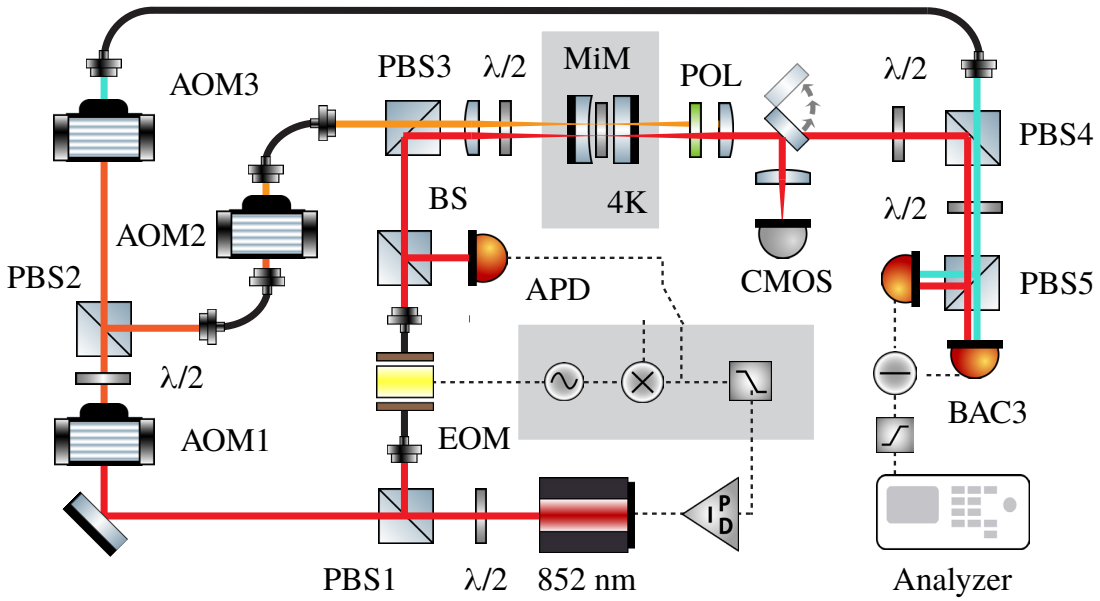

Figure 2.13: Illustration of the heterodyne detection setup. We expand our setup shown in Figure 2.5 to derive three beams with different frequencies from the same laser using three AOMs. After transmitting through the MiM cavity, the probe beam (red) is spatially overlapped with the LO (cyan). The cooling beam (orange) is used to optically cool the membrane mode and is blocked at the cavity output by a polarizer (POL). A balanced photoreceiver (BAC3) generates the heterodyne signal, which is bandpass filtered and analyzed.

essence three AOMs, from which we derive two optical tones, and a balanced receiver. The light from the Ti:sapphire laser at a wavelength of around $\lambda = 852\,\mathrm{nm}$ is split by means of a half-waveplate ($\lambda/2$) and PBS1, and the reflected vertically polarized light is sent to the optomechanical cavity as described before. This beam, with an optical frequency $\omega_\mathrm{p} = 2\pi c/\lambda$, will be referred to as the probe beam in the following. The horizontally polarized light at PBS1 is guided through AOM1, shifting its frequency upwards by 62.5 MHz. After that, we place a half-waveplate and PBS2 to again separate two beams. The reflected part is coupled into a fiber and guided to AOM2, where the frequency is shifted downwards by $62.5\,\mathrm{MHz} - \Delta_\mathrm{cl}/2\pi$, with $\Delta_\mathrm{cl}/2\pi \sim -2.6\,\mathrm{MHz}$. The light is then sent via a fiber to the cavity and serves as a red-detuned cooling beam with a frequency of $\omega_\mathrm{cl} \coloneqq \omega_\mathrm{l} + \Delta_\mathrm{cl}$ and orthogonal polarization compared to the probe beam. At the transmission port of PBS2, the light passes through AOM3 and is shifted down in frequency by $62.5\,\mathrm{MHz} + \Delta_\mathrm{LO}/2\pi$, resulting in a tone at $\omega_\mathrm{LO} \coloneqq \omega_\mathrm{l} - \Delta_\mathrm{LO}$, where $\Delta_\mathrm{LO}/2\pi \approx 10.742\,\mathrm{MHz}$. The light is guided through a fiber and is spatially overlapped with the probe beam at the cavity output to serve as a LO. We use a high-bandwidth home-built balanced photoreceiver (BAC3) to detect the light. The transmitted light from the cooling beam is blocked by means of a thin film polarizer (POL) at the cavity output.

Figure 2.14 shows an illustration of the spectrum with the three optical tones used in our setup as well as the cavity resonance at a frequency of ω_c. We reference ω_c to the probe beam via the detuning $\Delta_\mathrm{p} \coloneqq \omega_\mathrm{p} - \omega_\mathrm{c}$.

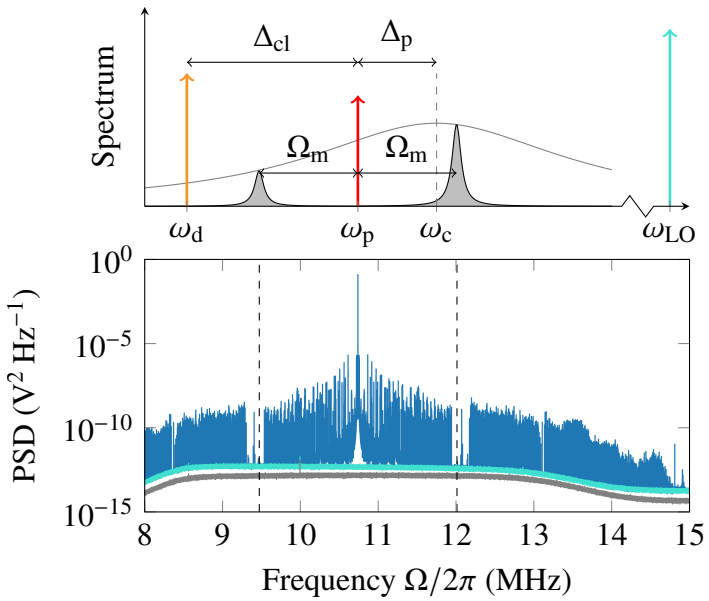

Figure 2.14: Heterodyne detection signal. Top: Sketch of the optical spectrum with the tones used in our setup, i.e., the cooling beam (orange), probe beam (red) and LO (cyan). The probe beam carries mechanical sidebands (gray-filled peaks), which are weighted by the square magnitude of the cavity susceptibility (solid gray line). Bottom: Measured heterodyne signal (blue) of the membrane motion with sideband frequencies from the mode of interest at $\Omega_m/2\pi = 1.275\,\mathrm{MHz}$ indicated as black dashed lines. SN and electronic noise backgrounds are shown in cyan and gray, respectively.

2.3.1.2 Heterodyne signal of the membrane motion

The difference photocurrent $\hat{i}_-$ from BAC3 is characterized by a large beating at the frequency of Δ_{LO}. This can be seen in the first term of the following expression, where we substitute the time-dependent phase $\phi \longrightarrow \Delta_{LO}t$ in Equation (1.4):

$$\hat{i}_- = 2\alpha_{LO}\alpha_p \cos(\Delta_{LO}t) + \sqrt{2}\alpha_{LO}\left(\delta\hat{X}_p \cos(\Delta_{LO}t) + \delta\hat{Y}_p \sin(\Delta_{LO}t)\right). \tag{2.25}$$

Here the coherent amplitudes of the probe beam transmitted through the cavity and the LO are α_p and α_{LO}, respectively. In the second term of Equation (2.25) we find the fluctuations of the probe beam described by the amplitude quadrature $\delta\hat{X}_p$ and phase quadrature $\delta\hat{Y}_p$. In contrast to homodyne detection, the quadratures cannot be addressed individually by adjusting the phase of the LO. Heterodyning simultaneously measures both quadratures, which is also reflected in the normalized PSD of the photocurrent, i.e., (in the rotating wave approximation) [11][8]

$$\begin{aligned} S_{ii}(\Omega) = \frac{1}{4}\Big(&S_{XX}^{out}(-\Omega - \Delta_{LO}) + S_{YY}^{out}(-\Omega - \Delta_{LO}) \\ &+ S_{XX}^{out}(\Omega - \Delta_{LO}) + S_{YY}^{out}(\Omega - \Delta_{LO})\Big), \end{aligned} \tag{2.26}$$

[8]Notice that in [11] Δ_{LO} is defined with the opposite sign.

where S_{XX}^{out} and S_{YY}^{out} denote the PSDs of the amplitude and phase quadratures of the probe beam at the cavity output, respectively. They are found by solving the linearized Langevin equations (A.43) and (A.44) in the frequency domain and using the input-output relations (see Equation (A.63)), as well as the definition of the PSD in Equation (A.3). We assume that the input quadrature fluctuations $\delta\hat{X}_{\text{in}}$ and $\delta\hat{Y}_{\text{in}}$ correspond to SN so that the noise correlation relations in Equations (A.57) and (A.58) apply. Then, the photocurrent PSD is found to be

$$S_{ii}(\Omega) = \frac{1}{2} + \frac{g^2\eta\kappa}{2q_{\text{zp}}^2}\Big(S_{qq}(-\Omega - \Delta_{\text{LO}})\,|\chi_{\text{c}}(-\Omega - \Delta_{\text{LO}})|^2 + S_{qq}(\Omega - \Delta_{\text{LO}})\,|\chi_{\text{c}}(\Omega - \Delta_{\text{LO}})|^2\Big). \tag{2.27}$$

Here the first term represents the white SN background and the second term contains the membrane's displacement PSD S_{qq}, centered around $\pm\Delta_{\text{LO}}$, and multiplied by the absolute square of the cavity susceptibility χ_{c}. As one might expect, the displacement sensitivity depends on the square of the cavity-enhanced coupling rate g^2, proportional to the intra-cavity photon number. In Equation (2.27) we introduce the overall detection efficiency η, which in our setup is estimated to be $\eta = \eta_{\text{c}}\eta_{\text{opt}}\mathcal{V}^2\eta_{\text{det}} \approx 0.6$, where $\eta_{\text{c}} \approx 0.93$ is the cavity output coupling, $1 - \eta_{\text{opt}} \approx 0.12$ is the loss due to optical elements, $\mathcal{V} = 0.92$ is the fringe visibility, and $\eta_{\text{det}} = 0.87$ is the nominal quantum efficiency of BAC3.

A typical heterodyne spectrum is shown in Figure 2.14, where the optical power of the LO at the detector is $P_{\text{LO}} \approx 430\,\mu\text{W}$ and the power of the probe at the cavity input is $P_{\text{p}}^{\text{in}} = 53\,\mu\text{W}$. We maximize $|g_0|$ and η_{c} by adjusting the membrane position z_{m} in the standing wave (see Section 2.2.3.4) and stabilize the laser frequency to the cavity resonance with $\Delta_{\text{p}}/2\pi \approx -1\,\text{MHz}$. In the spectrum, we see the beat note at $\Delta_{\text{LO}}/2\pi \approx 10.742\,\text{MHz}$ visible as a sharp peak and surrounded by a large number of sidebands. Each pair of sidebands represents a different membrane mode. The 250 kHz-wide gaps around $(\Delta_{\text{LO}} - \Omega_{\text{m}})/2\pi \sim 9.5\,\text{MHz}$ and $(\Delta_{\text{LO}} + \Omega_{\text{m}})/2\pi \sim 12\,\text{MHz}$ show the phononic bandgap, which contains our mode of interest; the fundamental defect mode A at $\Omega/2\pi = 1.275\,\text{MHz}$. The background in the bandgap is dominated by SN. Notice that we use a bandpass filter centered near Δ_{LO}, rejecting unwanted noise at frequencies $\Omega/2\pi \lesssim 8.5\,\text{MHz}$ and $\Omega/2\pi \gtrsim 13\,\text{MHz}$.[9]

2.3.1.3 Sideband ratio and thermometry

Heterodyne detection gives us access to a straightforward method to determine the membrane mode temperature, or equivalently the mean phonon occupancy $\bar{n}$. The method is known as sideband thermometry [77, 106, 107] and is based on the fact that every mechanical resonator oscillating near the quantum ground state of motion has a measurably asymmetric displacement PSD (see Appendix A.2.3).

[9]This prevents aliasing during digital detection (with a sample rate of 30 MHz) and suppresses DC noise so that we can use the entire analog-to-digital converter's range.

To describe the method, let us first transform the frequency axis in Equation (2.27) by substituting $\Omega \to \Omega + \Delta_{\mathrm{LO}}$ so that the beating at $+\Delta_{\mathrm{LO}}$ is shifted to zero frequency. Then, we define the ratio R_{sa} between the Stokes sideband at $\Omega = -\Omega_{\mathrm{m}}$ and the anti-Stokes sideband at $\Omega = \Omega_{\mathrm{m}}$ as

$$R_{\mathrm{sa}} \coloneqq \frac{S_{ii}(-\Omega_{\mathrm{m}})}{S_{ii}(\Omega_{\mathrm{m}})}. \tag{2.28}$$

Next, we solve the displacement PSD in Equation (A.31) for $\bar{n}$, assuming that the membrane mode is optically cooled and out-of-equilibrium with its thermal environment ($\bar{n}_{\mathrm{th}} \to \bar{n}$). This yields

$$\bar{n} = \left(\frac{S_{qq}(-\Omega_{\mathrm{m}})}{S_{qq}(\Omega_{\mathrm{m}})} - 1 \right)^{-1}, \tag{2.29}$$

$$\approx \left(R_{\mathrm{sa}} \left| \frac{\chi_{\mathrm{c}}(\Omega_{\mathrm{m}})}{\chi_{\mathrm{c}}(-\Omega_{\mathrm{m}})} \right|^2 - 1 \right)^{-1}. \tag{2.30}$$

In the last line, we use Equations (2.27) and (2.28), neglect the SN background and we arrive at the expression that will be used repeatedly through the remainder of this chapter. It directly relates the measured sideband ratio R_{sa} to the phonon occupancy $\bar{n}$. In the ground state ($\bar{n} = 0$) we expect the anti-Stokes sideband to vanish, i.e., $S_{qq}(\Omega_{\mathrm{m}}) = 0$ so that $R_{\mathrm{sa}} = \infty$. On the other hand, if $\bar{n} \gg 1$ we expect $S_{qq}(-\Omega_{\mathrm{m}}) \approx S_{qq}(\Omega_{\mathrm{m}})$ and $R_{\mathrm{sa}} = 1$ assuming $\Delta_{\mathrm{p}} = 0$.

Sideband thermometry is a particularly convenient and robust method to determine $\bar{n}$. This is because we analyze the relative size of peaks in the photocurrent PSD and do not rely on a thorough calibration of the signal into units of $\mathrm{m^2\,Hz^{-1}}$, for which knowledge of the optomechanical parameters g, κ, q_{zp}, and the detection efficiency η in Equation (2.27) is required. Yet there are a number of characteristics that we have to consider to correctly determine the phonon occupancy via sideband thermometry, as will be detailed in the following section.

2.3.2 Response and noise characterization

In this section, we characterize the detector response, the cavity response, and classical noise from different sources in our setup. All of the above can cause systematic errors to the measurement of the sideband ratio, if not properly accounted for.

2.3.2.1 Detector and cavity response

The responses of the detector and the electronic components in the signal chain are determined by blocking the probe beam and only sending the LO to both photodiodes of the detector. In the frequency window of interest (8…14 MHz) the noise in the signal is dominated by SN that is frequency-independent (white noise) and thus conveniently serves as a reference. In Figure 2.15 we show the measured PSD, resembling predominantly the response of the electronic band-pass filter. The averaged spectrum at a total

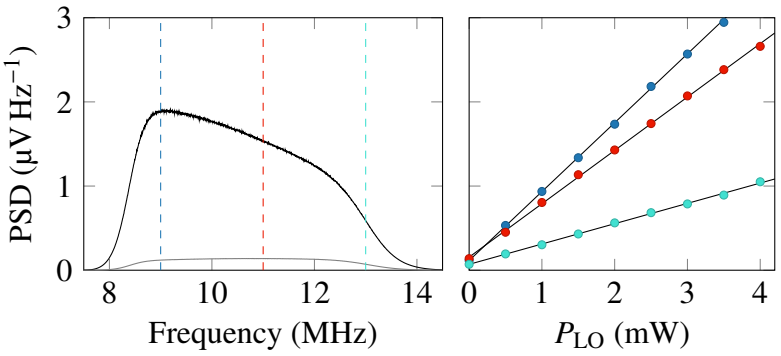

Figure 2.15: Response of the balanced heterodyne detector. Left: Averaged PSD from a SN measurement (black line) at an optical power of $P_{LO} = 2.05\,\text{mW}$ balanced between the two photodiodes of BAC3. The gray line shows the electronic noise of the detector and the colored dashed lines indicate the frequency bins at which we extract the SN level for the plot on the right. Right: SN level in the PSD versus P_{LO} for the three frequency bins indicated on the left. Dots are data points, whose color-code refer to the dashed lines, and black solid lines are linear fits.

optical power of $P_{LO} = 2.05\,\text{mW}$ is about ten times larger than the electronic noise of the detector. For three different frequency bins across the region of interest, we verify that the noise is indeed limited by SN, demonstrating a linear scaling with P_{LO} as shown on the right side of Figure 2.15. We subtract the electronic noise from the PSD to get only the SN at $P_{LO} = 2.05\,\text{mW}$, smoothen[10] the trace and use it to normalize all subsequent heterodyne spectra acquired using the same electronics and $\Delta_{LO}/2\pi \approx 10.742\,\text{MHz}$.

With the detection response accounted for, we now measure how the cavity response alters the sideband ratio R_{sa}. This is done by acquiring heterodyne spectra for different values of $\Delta_p < 0$ and selecting a number of mechanical modes of the membrane that are outside the bandgap in the frequency range $\Omega_m/2\pi = 80\,\text{kHz}...2\,\text{MHz}$. Using low input powers of the probe $P_p^{in} = 3\,\mu\text{W}$ and the cooling beam $P_{cl}^{in} = 10\,\mu\text{W}$ at which cooling due to dynamical backaction is small, we ensure that the modes have high thermal occupancies and their displacement PSD is essentially symmetric. Now, for each pair of sidebands induced by the membrane modes we numerically integrate the heterodyne spectrum in small windows ($\sim 1\,\text{kHz}$) around the peaks and calculate the ratio of the integrals, analogous to Equation (2.28). The left hand side of Figure 2.16 shows data acquired in such a way. As one might expect, the cavity causes a frequency-dependent asymmetry between the sidebands. At lower mechanical frequencies the ratio is near unity, while for larger mechanical frequencies it changes significantly with the detuning.

The behavior is readily described by the fact that each sideband is weighted by the absolute square of the cavity susceptibility $\chi_c(\Omega)$ as expressed in Equation (2.27). We fit the function $|\chi_c(-\Omega)/\chi_c(\Omega)|^2$ and from that obtain an average linewidth $\kappa/2\pi = 3.133(9)\,\text{MHz}$, as well as the detunings Δ_p of each dataset. On the right side of Figure 2.16, the latter are shown to be in agreement with the detunings measured via the PDH signal (see Section 2.2.2.4). When calculating the sideband ratio R_{sa} of the mechanical mode of interest, we compensate for the extracted cavity response, dividing

[10] We smoothen using a Hanning window with a width of 300 kHz.

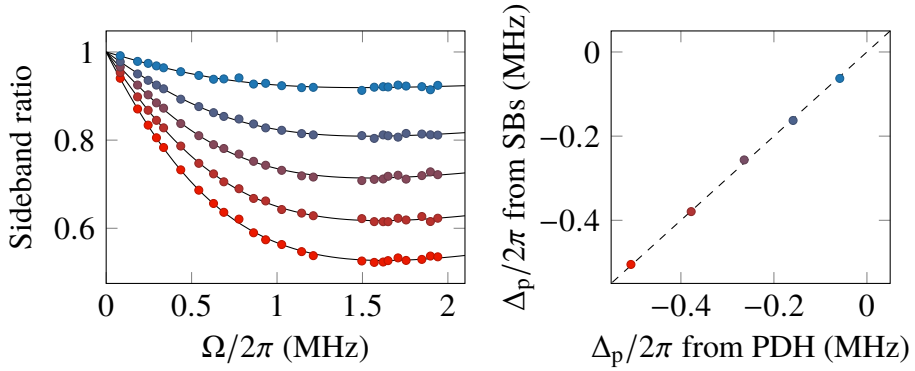

Figure 2.16: Cavity response extracted from the asymmetry of mechanical peaks. Left: Ratios of integrated sidebands of mechanical modes outside the bandgap for different detunings $\Delta_p \approx \{-0.51, -0.38, -0.26, 0.16, -0.06\}$ MHz (red to blue dots). Solid black lines are fits. Right: Detunings extracted from the fit to each dataset compared to those extracted from the PDH signal (color-coded dots). The dashed black line is a linear function with unity slope and zero intercept. Statistical errors of the detunings are ~ 10 kHz and are not shown.

R_{sa} by the fit function evaluated at the respective frequency $\Omega_m/2\pi = 1.275$ MHz. We confirm that this results in $R_{sa}|\chi_c(\Omega)/\chi_c(-\Omega)|^2 \approx 1$ to within ~ 1 % for the low cooling powers used and large values of $\bar{n}$ expected here.

2.3.2.2 Laser and mirror noise

Next, we characterize the technical noise in our setup and focus on laser amplitude and phase noise of the probe beam and the cooling beam. In regard to ground-state cooling of the membrane mode this type of noise is unwanted, since it increases the background level, compromising displacement sensitivity, and contributes a driving force via radiation pressure that increases the minimum achievable occupancy. The latter will be discussed further in Section 2.3.3.2.

In order to measure the amplitude noise, the probe beam and the cooling beam bypass the optomechanical cavity and impinge on a single photodiode of the detector. Both beams are adjusted to have the same optical power of 190 µW and the LO is blocked. Now, for each beam separately we record the photocurrent PSD in the frequency range $\Omega = 0...2$ MHz as shown on the left hand side of Figure 2.17. Here we first subtract and then divide the spectra by a SN trace, acquired by detecting light from an incandescent flashlight[11] using the same detector and the same average photocurrent. The broad peak around 380 kHz represents the laser relaxation oscillations. At the frequency of interest $\Omega_m/2\pi = 1.275$ MHz the noise levels are significantly lower than the SN. Averaged over a window of 50 kHz around Ω_m the classical noise of the probe beam and the cooling beam in comparison to SN are $C_{xx} \approx 7$ % and $C_{xx} \approx 14$ %, respectively. This means that the two AOMs, with which we control the detuning Δ_{cl} (see Section 2.3.1.1), introduce extra noise in the cooling beam.

[11]The flashlight constitutes a thermal light source with very short coherence time, so that intensity fluctuations up to several MHz are dominated by SN.

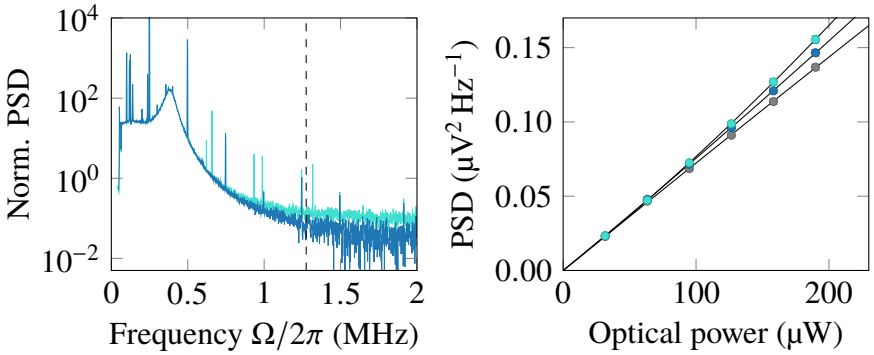

Figure 2.17: Laser amplitude noise of the probe and the cooling beam. Left: Amplitude noise PSD from which we subtract SN and normalized by SN, comparing the probe beam (blue) and the cooling beam (cyan) at an optical power of 190 µW. The dashed line indicates the mechanical frequency $\Omega_m/2\pi = 1.275$ MHz. Right: Noise levels of the PSDs in a 50 kHz window around $\Omega_m/2\pi$ measured as a function of optical power and fit to quadratic functions (black solid lines). While for SN (gray dots) we find a negligible quadratic component, the probe beam (blue) and cooling beam (cyan) show quadratic scalings.

We want to verify that part of the amplitude noise is indeed classical and determine the noise level around Ω_m for different optical powers. The result is shown on the right hand side of Figure 2.17, where we fit second-order polynomials to the data. The noise in the cooling beam has a larger quadratic component than that of the probe beam. In comparison, SN shows virtually no quadratic scaling. These findings evidence the presence of small amounts of classical amplitude noise in our setup. It should be noted that the optical powers shown here are relevant for our system as we require a cavity input power on the order of 100 µW to cool the defect mode to the backaction limit (see Section 2.3.3.2).

We characterize the phase noise of the probe beam and the cooling beam by means of an empty cavity with similar high-reflective mirrors and dimensions as used in our MiM system. The empty cavity is placed in a vacuum chamber with a pressure of $< 1 \times 10^{-5}$ mbar and a temperature of $T = 300$ K. We couple each of the two beams into the cavity and stabilize its frequency to the slope of the resonance (half-fringe) so as to transduce part of the phase noise into amplitude noise of the intra-cavity field. The optical powers are adjusted to the same value at the cavity output in transmission, i.e., $P_p^{out} = P_{cl}^{out} = 64$ µW. We record spectra separately for each beam via direct detection in transmission. The results are shown in Figure 2.18. Here a small phase-modulation of the probe beam induced by the EOM with a well-known frequency and amplitude is used to calibrate both PSDs, as well as the SN background, in terms of frequency fluctuations (in units of Hz^2 Hz^{-1}). As before, the SN background is measured with a flashlight and the same photodetector. Around the frequency of interest Ω_m the spectra corresponding to the probe beam and the cooling beam are nearly identical. We see a number of broad peaks that are several orders of magnitude larger than the SN. The peaks are likely due to mirror substrate modes which have been studied previously in a similar MiM system [99]. If this is true, we cannot reliably extract the phase noise

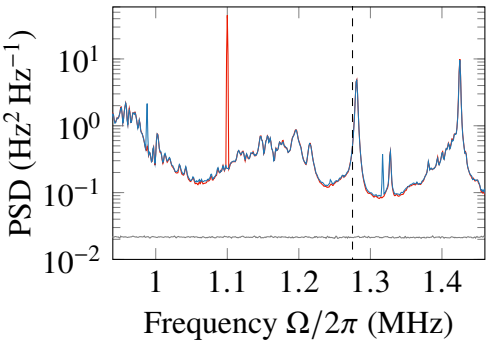

Figure 2.18: Laser frequency noise and cavity mirror noise. Frequency noise spectral density measured using an empty Fabry-Pérot cavity at room temperature for the probe beam (red) and the cooling beam (blue). The spectra were recorded at the same optical power and calibrated using a well-known phase modulation at 1.1 MHz. The dashed line indicates the frequency $\Omega_m/2\pi = 1.275\,\text{MHz}$ at which the membrane mode of interest is found in our MiM system. The gray line corresponds to the SN at the same detected optical power.

of the two beams from this measurement. A way to proceed would be to cryogenically cool the empty cavity to $T = 4.2\,\text{K}$, so that the mirror modes decrease by a factor of ~ 70, and repeat the measurements for both beams. This has not been realized yet.

2.3.3 Single beam operation

Having considered different sources of errors, we now put our setup and the sideband thermometry method to the test. For all measurements presented in this section and Section 2.3.4, we maximize $|g_0|$ and η_c by adjusting the relative membrane position z_m with respect to the standing wave, and cool the defect mode of our membrane via dynamical backaction. To start with, we utilize a single laser beam to drive the cavity, that is to say, we block the cooling beam and send only the probe beam to the cavity. The temperature of the cold finger is $T = 4.2\,\text{K}$.

2.3.3.1 Detuning series

We measure heterodyne spectra at a fixed input power of the probe beam $P_p^{in} = 20\,\mu\text{W}$ and for different detunings[12] $\Delta_p < 0$. After normalizing each spectrum to SN, we select 10 kHz-wide windows around the sidebands induced by the defect mode of interest. To these data we fit the sum of two Lorentzian functions, in accordance with the square magnitude of the mechanical susceptibility in Equation (A.15). For the two Lorentzians we assume equal FWHMs Γ_{eff} and background levels (offsets), as well as the same peak frequency but with opposite signs $\pm\Omega_{eff}$. Examples of the fits are shown in Figure 2.19, where Stokes and anti-Stokes sidebands are superimposed by transforming the frequency axis as $\Omega \rightarrow |\Omega|$.

[12]Here Δ_p is determined via mechanical sideband asymmetries as detailed in Section 2.3.2.1.

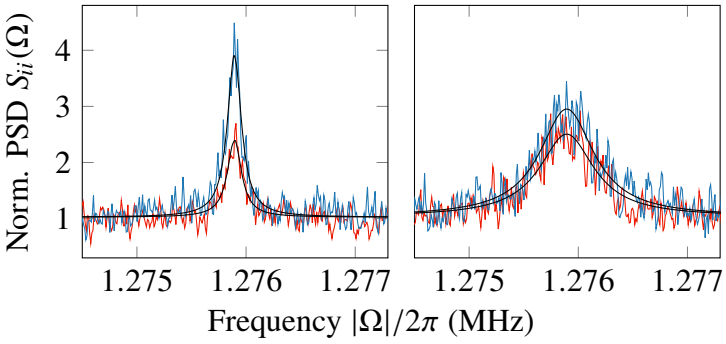

Figure 2.19: Zoom-ins to heterodyne spectra for the single beam detuning series. Stokes (red) and anti-Stokes (blue) sideband peaks for different cavity detunings $\Delta_p/2\pi = -3\,\mathrm{MHz}$ (left) and $\Delta_p/2\pi = -1.33\,\mathrm{MHz}$ (right). Black lines are Lorentzian fits from which we extract the linewidth Γ_{eff}, resonance frequency Ω_{eff} and peak areas.

The data show significant broadening of the linewidth which depends on the detuning, as expected from optical damping via dynamical backaction (see Appendix A.3.2). In Figure 2.20 we plot Γ_{eff} and the frequency shift $\delta\Omega_{\mathrm{m}}$ versus Δ_p with several data points in the detuning range $-3.5\,\mathrm{MHz}...-0.5\,\mathrm{MHz}$. The behavior of the damping rate is well-reproduced by a fit to Equation (A.50), where we take into account how $g^2 \propto n_c \propto |\chi_c(0)|^2$ depends on Δ_p for a fixed P_p^{in}. Note that we use an overall scaling as the only free parameter for the fit. The mode frequency Ω_{m} is described by Equation (A.51) where we include the aforementioned detuning dependence of g^2. From a fit we extract the mechanical frequency $\Omega_{\mathrm{m}}/2\pi = 1.276\,07(1)\,\mathrm{MHz}$ at $\Delta_p = 0$ and calculate the frequency shift $\delta\Omega_{\mathrm{m}} := \Omega_{\mathrm{eff}} - \Omega_{\mathrm{m}}$ for each data point. As can be seen, the latter is negative and on the order of $-100\,\mathrm{Hz}$. This compares favourably with estimates of $\Gamma_{\mathrm{eff}}/2\pi \approx 503\,\mathrm{Hz}$ and $\delta\Omega_{\mathrm{m}}/2\pi \approx -183\,\mathrm{Hz}$ for $\Delta_p = -\Omega_{\mathrm{m}}$, assuming $g_0/2\pi \approx 84\,\mathrm{Hz}$, $n_c \approx 10^5$, $\kappa/2\pi \approx 3.7\,\mathrm{MHz}$, and $\Gamma_{\mathrm{m}}/2\pi \approx 1.36\,\mathrm{mHz}$. Employing Equation (A.53) then yields a cooling factor of $T/T_{\mathrm{eff}} = \Gamma_{\mathrm{eff}}/\Gamma_{\mathrm{m}} \approx 3.7 \times 10^5$.

In Figure 2.19 we see sideband asymmetries in both heterodyne spectra; the anti-Stokes sidebands are larger so that $R_{\mathrm{sa}} < 1$. This is the case for all measurements presented here and is due to the cavity response as previously discussed in Section 2.3.2.1. From the Lorentzian fits we extract the peaks' spectral areas and use them to calculate R_{sa} as well as the mean phonon occupancy $\bar{n}$ via Equation (2.30). The results are shown in Figure 2.21, where the lowest value is $\bar{n} = 0.80(2)$. We fit the data to

$$\bar{n} \approx \frac{\Gamma_{\mathrm{m}}}{\Gamma_{\mathrm{eff}}}\bar{n}_{\mathrm{th}} + \bar{n}_{\mathrm{min}}, \tag{2.31}$$

which follows from Equation (A.62) assuming $\Gamma_{\mathrm{opt}} \approx \Gamma_{\mathrm{eff}}$. Here $\bar{n}_{\mathrm{min}}$ is the minimum achievable occupancy, defined in Equation (A.61). It amounts to $\bar{n}_{\mathrm{min}} = 0.381(5)$ for our measured cavity parameters above and the optimal detuning for the cooling

$$\Delta_{\mathrm{min}} = -\sqrt{\Omega_{\mathrm{m}}^2 + \kappa^2/4}, \tag{2.32}$$

yielding $\Delta_{\mathrm{min}}/2\pi = -2.25(2)$ MHz. The peak areas from which we calculate R_{sa} are also shown Figure 2.21. Their detuning dependence is proportional to the Bose enhanced scattering rates $(\bar{n}+1)\Gamma_+$ (Stokes sideband) and $\bar{n}\Gamma_-$ (anti-Stokes sideband), where Γ_- and Γ_+ are defined in Equations (A.54) and (A.55), respectively.

2.3.3.2 Power series

Let us now see how much further we can lower the phonon occupancy $\bar{n}$ via optical cooling with the probe beam. Fixing the cavity detuning to $\Delta_{\mathrm{p}} = \Delta_{\mathrm{min}}$, we perform measurements at different input powers in the range $P_{\mathrm{p}}^{\mathrm{in}} = 3.2...320\,\mu$W. For each value of $P_{\mathrm{p}}^{\mathrm{in}}$ three heterodyne spectra are recorded from which we determine Γ_{eff}, the peak area of each sideband, $\bar{n}$ and $\bar{n}_{\mathrm{min}}$ as described above. The results are shown in Figure 2.22 and plotted versus $\Gamma_{\mathrm{eff}}/2\pi \propto P_{\mathrm{p}}^{\mathrm{in}}$. As expected from Equation (2.31), we see that $\bar{n}$ decreases with Γ_{eff} and levels off for larger powers. We average the data points for $\bar{n}$ obtained from the three spectra at $P_{\mathrm{p}}^{\mathrm{in}} = 100\,\mu$W and $\Gamma_{\mathrm{eff}}/2\pi \sim 3$ kHz, and find the lowest occupancy in our data of $\bar{n} = 0.55(1)$. To put this number into perspective, the probability of finding the membrane mode in a state with n phonons reads [11]

$$p(n) = \frac{\bar{n}^n}{1+\bar{n}^{n+1}}, \tag{2.33}$$

and yields $p(0) = 76(1)\,\%$. This means that the membrane spends the majority of its time in the ground state of motion ($n = 0$). The data also shows that we cool the mode close to the backaction limit, where $\bar{n} \approx \bar{n}_{\mathrm{min}} = 0.442(5)$. Here we again average three data points extracted from the measurements at $P_{\mathrm{p}}^{\mathrm{in}} = 100\,\mu$W.

Equation (2.31) provides an approach to determine the thermal occupancy $\bar{n}_{\mathrm{th}}$ and the membrane's bath temperature $T_{\mathrm{m}} = \hbar\Omega_{\mathrm{m}}\bar{n}_{\mathrm{th}}/k_{\mathrm{b}}$, which follows from Equation (A.23).

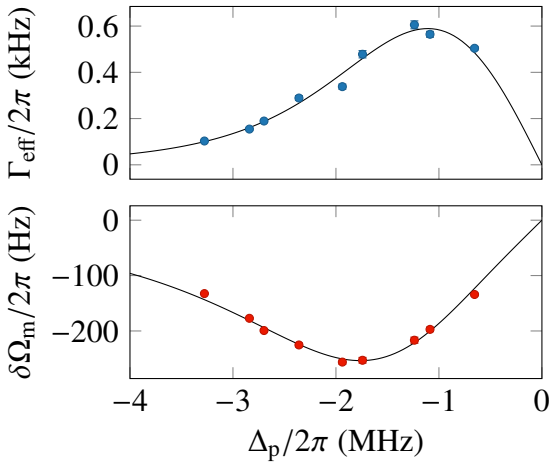

Figure 2.20: Optical damping and spring effect versus detuning. Effective mechanical linewidth (top) and frequency shift (bottom) as a function of cavity detuning $\Delta_{\mathrm{p}} < 0$ for a fixed input power $P_{\mathrm{p}}^{\mathrm{in}} = 20\,\mu$W and $\kappa/2\pi = 3.70(3)$ MHz. The data points (colored dots) are obtained from Lorentzian fits to heterodyne spectra. Black solid lines are model fits.

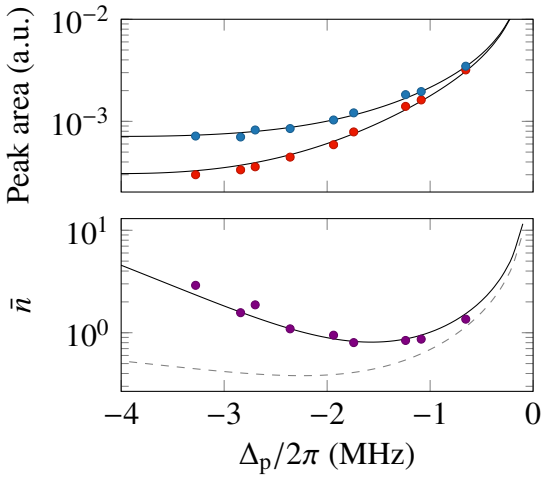

Figure 2.21: Sideband thermometry detuning series. Top: Measured peak spectral areas of Stokes sidebands (red dots) and anti-Stokes sidebands (blue dots) as a function of detuning Δ_p for a fixed input power $P_p^{in} = 20\,\mu W$ and $\kappa/2\pi = 3.70(3)\,MHz$.. Bottom: Mean phonon occupancy $\bar{n}$ (purple dots) versus Δ_p. Solid black lines are fits and the dashed line shows the calculated minimum phonon occupancy $\bar{n}_{min}$.

We fit the expression for $\bar{n}$ to our data in the regime where $\Gamma_{eff}/2\pi \lesssim 3\,kHz$ and reveal that $T_m = 10.4(6)\,K$. Comparable membrane temperatures were reported in previous work of Quantop and SLAB where similar MiM systems were used [34,35,87]. Furthermore, the fit to $\bar{n}$ also yields $\bar{n}_{min} = 0.462(8)$, in fair agreement minimum occupancy mentioned above.

In Figure 2.22 the data for $\bar{n}$ corresponding to $\Gamma_{eff}/2\pi \gtrsim 5\,kHz$ deviate systematically from the fitted curve. As it seems, the values increase with Γ_{eff}, which is not expected from the model. A possible explanation for this inconsistency is the fact that the relatively large optical powers of $P_p^{in} > 170\,\mu W$ used here, alongside with the LO power of $P_{LO} = 400\,\mu W$, give rise to a large heterodyne beat note that saturates the transimpedance amplifier in our detector. We test the effect of this saturation by acquiring spectra $S_{ii}^{bg}(\Omega)$ normalized to SN, while the probe beam bypasses the cavity and is directly sent to the detector. Without any mechanical peaks in the signal we compare the 'background' noise at $\pm\Omega_m$ and calculate the ratio $R_{bg} = S_{ii}^{bg}(-\Omega)/S_{ii}^{bg}(+\Omega)$ similar to Equation (2.28). In Figure 2.23 we plot R_{bg} as a function of the rms amplitude of the beat note at the detector output, proportional to the square root of the incident probe beam power (see Equation (2.25)). Initially at $R_{bg} = 1$ the ratio decreases once the rms amplitude exceeds $\sim 1.3\,V$. Provided that the sideband ratio R_{sa} used to calculate the phonon occupancy $\bar{n}$ follows the same behavior as R_{bg}, we might be overestimating $\bar{n}$ in Figure 2.22 because of the saturation. It should be noted that while we have reduced the power of the LO to prevent the detector from saturating we did not account for the rather subtle deviation of R_{bg} from unity near the saturation point. To fully overcome the saturation problem in the future, the gain of the transimpedance amplifier in the heterodyne detector needs to be reduced.

The detector saturation may not be the only source of systematic error in our data.

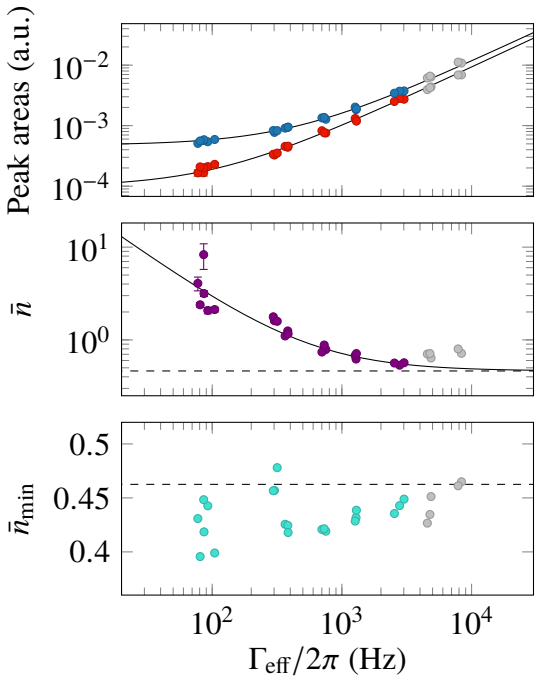

Figure 2.22: Sideband thermometry near the backaction limit. Top: Measured peak spectral areas of the Stokes sidebands (red dots) and anti-Stokes sidebands (blue dot) versus effective damping Γ_{eff}. The solid black lines are linear fits. Center: Phonon occupancy $\bar{n}$ as measured (purple dots) and described by a fit (solid line) from which we extract the membrane's bath temperature $T_{\mathrm{m}} = 10.4(6)\,\mathrm{K}$ and $n_{\mathrm{min}} = 0.462$ (dashed line). Bottom: The minimum occupancy (cyan dots) calculated via measured values of κ and Δ_{p}. The dashed line again indicates $\bar{n}_{\mathrm{min}} = 0.462(8)$ obtained from the fit in the center plot. Gray data points are discarded from the fits.

We need to examine whether at larger optical powers the membrane motion is driven by classical laser noise, as theoretically described in [108]. This requires a proper estimate of the phase noise, which can be done using an empty cavity at cryogenic temperature (see Section 2.3.2.2 and [87]) or via a delay-line interferometer [78]. For amplitude noise alone, we can express the contribution to the phonon occupancy by substituting $\bar{n} \longrightarrow \bar{n} + \bar{n}_{\mathrm{err}}$, where the correction term is given by [78]

$$\bar{n}_{\mathrm{err}} = \frac{g^2\kappa}{4\Gamma_{\mathrm{eff}}}(1-\eta_{\mathrm{c}})C_{\mathrm{xx}}\left|\chi_{\mathrm{c}}^{*}(-\Omega_{\mathrm{m}}) + \chi_{\mathrm{c}}(\Omega_{\mathrm{m}})\right|^2 . \tag{2.34}$$

Here C_{xx} denotes the amplitude noise coefficient in relation to SN. For the parameters used here, as well as $\Gamma_{\mathrm{eff}}/2\pi \gtrsim 5\,\mathrm{kHz}$ and $C_{xx} \sim 7\,\%$, we get $\bar{n}_{\mathrm{err}} \lesssim 6 \times 10^{-3}$. This is less than 2 % of the lowest measured $\bar{n}$ and hence does not account for the discrepancy shown in Figure 2.22. Finally, mirror noise could also cause a systematic error for large cooling powers. Indeed, the mirror mode with relatively large thermal displacement near the membrane mode of interest, visible in Figure 2.18, may contribute to the noise floor, offsetting the sidebands used to determine the occupancy. Further investigations on this matter are needed.

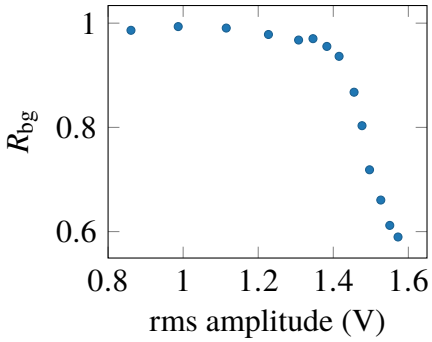

Figure 2.23: Saturation of the heterodyne photodetector. We measure the background noise around the sidebands at $\pm\Omega_m$ while the probe beam bypasses the cavity. As a result of detector saturation, the background ratio R_{bg} decreases if the rms amplitude of the heterodyne beat note in the voltage signal exceeds ~ 1.3 V.

2.3.4 Dual beam operation

There are a few reasons why we want to drive our cavity simultaneously with two beams, instead of only a single beam. For starters, it is convenient to stabilize the probe beam to the cavity resonance with $\Delta_p = 0$ using the PDH technique, since this is robust against power drifts [100]. The second (cooling) beam, whose detuning Δ_{cl} is well-defined by the AOM drive frequencies, can be controlled independently to optically cool or amplify the membrane motion. The cooling beam may also be rapidly switched in order to facilitate optical pulsing and fast changes in Δ_{cl}, while we maintain the locking using the probe beam. Among other things, pulse protocols are used for the generation of mechanical Fock states, envisioned in Section 2.4.

2.3.4.1 Beam rejection

When we introduce the cooling beam and record heterodyne spectra using the probe beam, we immediately face the following technical issue: the cooling beam cannot be fully rejected by the polarizer at the cavity output and thus creates a second beat note together with the LO that appears at $\Omega = -\Delta_{cl}$ (see Figure 2.24). Since the cooling beam couples to the membrane's motion, this beat note carries mechanical sidebands, constituting a dense distribution of noise peaks near $\Omega = \pm\Omega_m$, where $\Omega_m/2\pi \approx 1.275$ MHz corresponds to the defect mode of interest. With increasing cooling beam power the added beat note and the noise peaks become larger. This is demonstrated on the right hand side of Figure 2.24, where we plot the ratio between the two beat notes $S_{ii}(0)/S_{ii}(-\Delta_{cl})$, as a function of the power ratio P_{cl}^{out}/P_p^{out} measured at the cavity output. We see that the beat note ratio is inversely proportional to P_{cl}^{out}/P_p^{out}. In many cases, we want the cooling beam to be 100-fold stronger, resulting in a rather small beat note ratio of ~ 83 and the sidebands of interest being largely contaminated by the noise peaks.

We reduce the number of noise peaks near the Stokes sideband ($-\Omega_m$) by choosing $\Delta_{cl}/2\pi \approx -2.63$ MHz, as is the case for the spectrum in Figure 2.24. Here the bandgaps

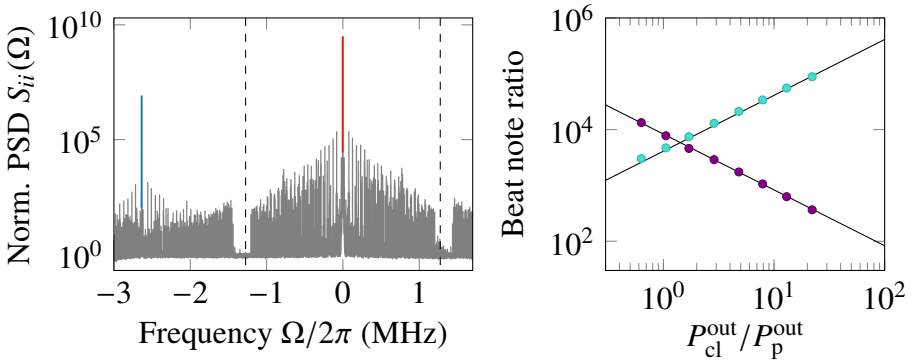

Figure 2.24: Rejection of the probe and the probe beams. Left: Photocurrent PSD $S_{ii}(\Omega)$ normalized to SN (gray) with $\Delta_{\mathrm{p}} = 0$, where the beat note from the probe beam is indicated in red. The cooling beam with $\Delta_{\mathrm{cl}}/2\pi = -2.63$ MHz creates another beat note marked in blue, which we minimize by adjusting the polarizer at the cavity output. Dashed lines indicate $\pm\Omega_{\mathrm{m}}/2\pi$. Right: Ratio between the two beat notes $S_{ii}(0)/S_{ii}(\pm\Delta_{\mathrm{cl}})$ when rejecting the cooling beam (purple dots) and the probe beam (cyan dots) versus the power ratio $P_{\mathrm{cl}}^{\mathrm{out}}/P_{\mathrm{p}}^{\mathrm{out}}$. Solid black lines are linear fits to the data.

in the peak distributions around the two beat notes overlap for $\Omega < 0$. However, this is not the case for $\Omega > 0$, meaning that we find many (yet smaller) unwanted peaks near the anti-Stokes sideband ($+\Omega_{\mathrm{m}}$). Notice that our choice of Δ_{cl} is similar to the optimal detuning $\Delta_{\mathrm{min}}/2\pi \approx -2.25$ MHz and therefore does not compromise significantly on the optical cooling of the defect mode.

The easiest way in our setup to effectively tackle this noise issue is to rotate the polarizer at the cavity output so that the probe beam is blocked and the cooling beam is used to generate the heterodyne signal.[13] The beat note ratio, now given by $S_{ii}(0)/S_{ii}(+\Delta_{\mathrm{cl}})$ assuming that $\Omega = 0$ corresponds to the beating between the cooling beam and the LO, is then linearly increasing with $P_{\mathrm{cl}}^{\mathrm{out}}/P_{\mathrm{p}}^{\mathrm{out}}$. Using a strong cooling beam and $P_{\mathrm{cl}}^{\mathrm{out}}/P_{\mathrm{p}}^{\mathrm{out}} = 100$, we expect a beat note ratio of $\sim 4 \times 10^5$ and a much cleaner spectrum than in the previous configuration.

2.3.4.2 Backaction due to the probe beam

Whether the resonant probe beam ($\Delta_{\mathrm{p}} \approx 0$) is used for detection or only for locking to the cavity resonance, it impacts the behavior of the membrane via additional radiation pressure backaction. In Appendix A.3.3 we derive the measured displacement PSD of a resonant beam at the cavity output. The PSD reaches a minimum, known as the standard quantum limit, if the membrane is in the ground state and the imprecision noise equals the backaction noise. With our setup we are in a position to study this behaviour and the effect on the phonon occupancy $\bar{n}$.

Figure 2.25 shows a measurement of $\bar{n}$, in which we generate the heterodyne signal using the cooling beam and the LO, while the probe beam is locking to the resonance with $\Delta_{\mathrm{p}} \approx 0$. The input power of the cooling beam is $P_{\mathrm{cl}}^{\mathrm{in}} = 53\,\mu$W and the detuning

[13] For this, the halfwave-plate at the input port of PBS4 is rotated by 45°.

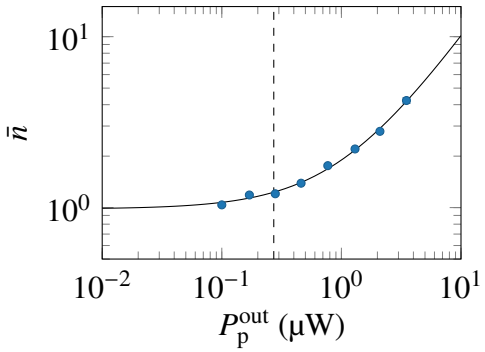

Figure 2.25: Backaction due to the resonant probe beam. Mean phonon occupancy $\bar{n}$ as a function of probe beam power P_p^{out} measured at the cavity output. Blue dots are data obtained from sideband thermometry using the cooling beam and the solid black line is a linear fit. From the slope a of the fit we extract the output power $P_p^{sql} = 1/4a \approx 0.272(6)\,\mu W$ corresponding to the standard quantum limit, as indicated by the dashed line.

is $\Delta_{cl} \approx -2.63\,MHz$. We gradually increase the probe beam power and find that $\bar{n}$ increases linearly with the probe power. To see why this is the case, let us write an expression similar to Equation (A.62) but including a second optical bath:

$$\bar{n} = \frac{\Gamma_m \bar{n}_{th} + \Gamma_{opt}^{cl} \bar{n}_{min}^{cl} + \Gamma_{opt}^{p} \bar{n}_{min}^{p}}{\Gamma_m + \Gamma_{opt}^{cl} + \Gamma_{opt}^{p}}, \tag{2.35}$$

$$\approx \frac{\Gamma_m \bar{n}_{th}}{\Gamma_{eff}} + \bar{n}_{min}^{cl} + \frac{4g_0^2 n_c^p}{\kappa \Gamma_{eff}} \left(1 + \frac{4\Omega_m^2}{\kappa^2}\right)^{-1}. \tag{2.36}$$

Here the superscripts 'cl' and 'p' refer to the cooling beam and the probe beam, respectively. In the last line we assume that $\Gamma_{eff} = \Gamma_m + \Gamma_{opt}^{cl} + \Gamma_{opt}^{p} \approx \Gamma_{opt}^{cl}$ meaning that the effective linewidth is dominated by the optical damping from the cooling beam. Furthermore, Equation (A.50) and Equation (A.61) are used with $\Delta_p = 0$ to find the last term in Equation (2.36). Since the intra-cavity photon number $n_c^p = P_p^{out}/\hbar\omega_l \eta_c \kappa$, the model confirms the measured linear relation between $\bar{n}$ and P_p^{out}.

We identify the optical power at which the backaction due to the probe beam adds an energy of $\hbar\Omega_m/4$ to the membrane, corresponding to the standard quantum limit [10]. Setting the last term in Equation (2.36) equal to $1/4$ and solving for the photon number, we see that the power at the output reads

$$P_p^{sql} = \hbar\omega_l \frac{\Gamma_{eff}\eta_c \kappa^2}{16 g_0^2} \left(1 + \frac{4\Omega_m^2}{\kappa^2}\right). \tag{2.37}$$

Notice that this expression also directly follows from the condition $4\Gamma_{meas}/\Gamma_{eff} = 1$ for the standard quantum limit used in Appendix A.3.3. Inserting our typical experimental parameters and $\Gamma_{eff}/2\pi = 0.85(3)\,kHz$ measured here into Equation (2.37), we get $P_p^{sql} = 0.25(9)\,\mu W$. From the linear fit in Figure 2.25 we extract a comparable value $P_p^{sql} = 1/4a = 0.272(6)\,\mu W$, where a is the slope of the fitted curve.

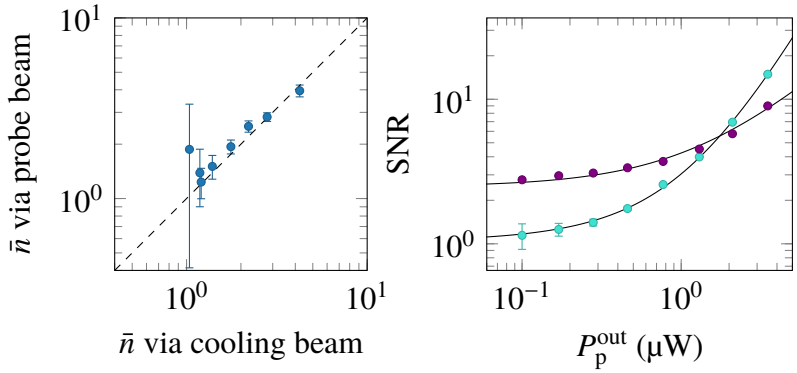

Figure 2.26: Sideband thermometry via the probe beam and the cooling beam. Left: Comparison between phonon occupancies $\bar{n}$ measured using the probe beam and the cooling beam. The dashed line is a linear function with unity slope and zero intercept. The uncertainties are extracted from Lorentzian fits to the sidebands. Right: SNR of the anti-Stokes sideband as a function of output probe power P_p^{out} for measurements via the probe beam (cyan dots) and the cooling beam (purple dots). Linear and quadratic fits are shown as black solid lines. Errors on $\bar{n}$ and SNR from the cooling beam measurements are < 5 % and are not shown.

2.3.4.3 Cooling beam and probe beam detection

The standard quantum limit refers to a balance between backaction and imprecision noise when using a resonant beam to detect the membrane motion (see Appendix A.3.3). The measurements in Figure 2.25 show only the effect of the backaction noise, since we utilize the cooling beam instead of the probe beam for detection and maintain the imprecision noise, inversely-proportional to the cooling beam power, throughout the power series. As a next step, we perform measurements of $\bar{n}$ under the same conditions as before but with the polarizer at the cavity output rotated by 90° to reject the cooling beam and generate the heterodyne signal via the probe beam. A comparision between the two configurations is shown in Figure 2.26. The two datasets reveal similar values for $\bar{n}$ but we see much larger uncertainties when using the probe beam. These uncertainties represent the measurement imprecision and naturally decrease with probe beam power.

We may also contrast the SNR achieved in the two configurations as shown on the right hand side of Figure 2.26. To determine the SNR for each measurement we extract the peak value of the anti-Stokes sideband from the Lorentzian fit and divide by the SN-limited background level. For the spectra acquired via the cooling beam the SNR scales linearly with P_p^{out}, in accordance with the Bose enhanced scattering rate $\Gamma_-^{cl}\bar{n} \propto P_p^{out}$. On the other hand, we see a quadratic behavior for the measurements performed with the probe beam, reflecting the fact that in this case the imprecision decreases and the backaction increases with P_p^{out}. Once again, we write down the scattering rate and see that $\Gamma_-^p\bar{n} \propto (P_p^{out})^2$, since $\Gamma_s^p \propto n_c^p \propto P_p^{out}$ (see Equation (A.54)).

2.4 Outlook

Our work presented above demonstrates a high degree of control over the defect mode motion in the MiM system, facilitating a mean phonon occupancy as low as $\bar{n} = 0.55(1)$ and interesting quantum effects such as radiation pressure backaction. There are many different directions into which this work can be continued and extended. In the following, we provide two particularly intriguing perspectives.

2.4.1 Optomechanics with a birefringent cavity

In a recent paper, researchers proposed a new method to independently measure the Stokes and anti-Stokes sidebands for sideband thermometry [109], which could be implemented in our MiM system. The method is based on a birefringent optomechanical cavity, in which polarization splitting of the fundamental cavity mode is observed, as illustrated on the left hand side of Figure 2.27. Linearly polarized input light, whose electric field vector is rotated by 45° with respect to the fast and the slow axes of the cavity, is placed in the middle of the two polarization modes. In the resolved sideband regime, if the splitting is on the order of two times the mechanical frequency ($2\Omega_\mathrm{m}$), Stokes and anti-Stokes sidebands are generated with perpendicular polarizations. At the cavity output a half-wave plate and a PBS are placed, adjusted such that each sideband creates a beat note with the unscattered light at either output port of the PBS. Using two separate photodetectors we can compare the amplitudes of the beat notes and infer the phonon occupancy $\bar{n}$. In contrast to our heterodyne setup, this configuration takes full advantage of the polarization degree of freedom and is technically simpler, as deriving and spatially overlapping a LO with the transmitted beam is superfluous.

In our MiM system, the polarization splitting is realized by replacing the soft-clamped SiN membrane with a 210-nm-thick birefringent SiN ribbon, such as the one studied in Section 1.2.3, and aligning the cavity mode to the center of the ribbon. Moreover, we remove the two silicon spacers so that the cavity length is reduced to $L \approx 1.76\,\mathrm{mm}$. We scan the laser wavelength $\lambda \approx 811\,\mathrm{nm}$ over the resonance and analyze the light transmitted through the cavity with a photodetector. The splitting is extracted by measuring the difference in frequency of the two peaks in the signal. We find values on the order of 100 MHz, varying sinusoidally with the position of the membrane z_m in the standing wave, as shown on the right hand side of Figure 2.27. Here z_m is controlled by means of the laser wavelength as described in Section 2.2.3.4. The behavior is reproduced by the TMM (see Appendix A.4), in which we calculate the cavity frequencies of a given longitudinal mode as a function of z_m for two different refractive indices $n = 2.0$ and $n + \Delta n$ of the membrane, and subtract the two results. The birefringence $\Delta n = C\Delta\sigma$ is determined assuming a stress anisotropy of $\Delta\sigma = 1.2\,\mathrm{GPa}$ and the photoelastic coefficient $C = 3.4 \times 10^{-6}\,\mathrm{MPa}^{-1}$ calculated in Equation (1.18). We attribute the discrepancy between data and the TMM to a small tilt between the membrane and the flat mirror, reducing the amplitude of the sinusoidal modulation (see Section 2.2.3.4).

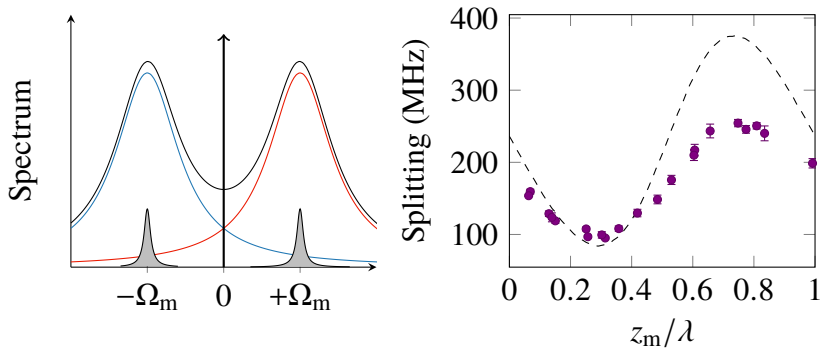

Figure 2.27: Optomechanics with a birefringent cavity. Left: Sketch of the polarization splitting, where light waves polarized along the fast and the slow axes see different resonances, as shown in blue and red, respectively. The black line shows the sum of the two. If a laser drive (black arrow), 45° linearly polarized, is placed between the two peaks and the splitting is $2\Omega_m$, the Stokes and anti-Stokes sidebands (grey shaded peaks) have nearly orthogonal polarizations. Right: Polarization splitting due to a birefringent SiN ribbon in our MiM system as a function of membrane position z_m at $\lambda \approx 811$ nm. The purple dots are data and the dashed line is calculated via the TMM.

The measured splittings are far larger than the typical mechanical frequencies of our membranes. For example, the ribbon used here has an estimated fundamental mode frequency of $\Omega_m/2\pi = \sqrt{\sigma/4\rho l^2} \approx 278\,\mathrm{kHz}$ [38], where $\sigma \approx 1.2\,\mathrm{GPa}$, $\rho = 2.7\,\mathrm{g\,cm^{-3}}$, and $l = 1.2\,\mathrm{mm}$. This means that in the current configuration we cannot implement the new method because the two sidebands nearly have the same polarization at the cavity output. However, as verified by the TMM, decreasing the splitting to $\sim 1\,\mathrm{MHz}$ is possible by increasing the cavity length tenfold and reducing the membrane thickness to about 30 nm. On top of that, we can reduce the size of the ribbon to increase its fundamental mechanical mode to $\Omega_m/2\pi \sim 500\,\mathrm{kHz}$ and thus match the mode splitting. This is in line with our idea of embedding the ribbon into the defect of a patterned SiN membrane, similar to the string resonator presented in Section 1.5, which will increase the quality factor of the ribbon through soft-clamping.

It should be mentioned that we have also observed MHz splittings of the cavity mode by mechanically compressing the curved cavity mirror from two sides with screws, i.e., by applying a force along an axis parallel to the mirror surface. In this case, the splitting is due to stress-induced birefringence in the mirror coating. If the compression can be properly controlled, for example, via a PZT clamped on the side of the mirror, we could implement sideband thermometry using the polarization degree of freedom without replacing our current SiN membrane.

2.4.2 Mechanical Fock-state generation

Another interesting route for our experiment is to take the control over the membrane motion via light even further and prepare other non-classical mechanical states than the ground state. Specifically, we want to generate and read out eigenstates of the Hamiltonian describing the mechanical resonator, i.e., phonon number (Fock) states and

superpositions thereof. By doing so, we could temporarily store quantum information in the form of individual phonons occupying the ultrahigh-Q membrane mode with long thermal coherence times. We estimate via Equation (A.27) the coherence time τ_1 of a single excitation ($n = 1$) using the parameters measured for our membrane, i.e., $\Omega_m/2\pi = 1.275\,\mathrm{MHz}$, $T_m \approx 10.4\,\mathrm{K}$, and $Q \approx 934 \times 10^6$, and get $\tau_1 \approx 229\,\mu\mathrm{s}$. This would allow us to study the behavior of single excitations in a macroscopic quantum system and constitute a long-lived quantum memory interesting for various applications in quantum information processing

In order to create a Fock state of motion via the optomechanical interaction in the weak-coupling regime ($g \ll \kappa$), a nonlinearity must be introduced that enables the conversion from Gaussian to non-Gaussian states [10]. Proposals for this are based on nonlinearities due to the mechanical resonator [110] or photon subtraction [111]. In [112] it was suggested to utilize the nonlinearity provided by the detection of a single photon scattered by the optomechanical interaction. Briefly, the scheme is as follows: in the resolved-sideband regime and with the mechanical resonator initiated in the ground state, a 'write' laser pulse, blue-detuned by the mechanical frequency ($\Delta = +\Omega_m$), is sent to the cavity. The optomechanical interaction is that of parametric down-conversion). The state of the mechanical resonator is projected onto a single-phonon Fock state upon detection of a single scattered photon (heralded preparation). For retrieval, a second 'read' laser pulse, red-detuned by the mechanical frequency ($\Delta = -\Omega_m$), is sent to the cavity and converts the phonon into an anti-Stokes scattered photon (state swap). Intensity interferometry [113] of the latter confirms the successful heralded generation of the single mechanical excitation, if the second-order correlation function vanishes $g^{(2)}(0) \to 0$. Recently, the scheme was realized utilizing a silicon nanobeam optomechanical crystal [114] and it was demonstrated that $g^{(2)}(0) \approx 0.65 < 1$, clearly evidencing sub-Poissonian statistics of the anti-Stokes scattered light. The deviation from a perfect single-photon state was mainly attributed to local heating from absorption of the laser pulses.

Before we can implement the scheme in our MiM system, we have to cool our membrane closer to the ground state than we have done so far. This is suggested by the relation $g^{(2)}(0) \approx 4\bar{n}$, derived in [112]. If $g^{(2)}(0) < 1$ is to be demonstrated, the mean phonon occupancy before sending the first pulse must be $\bar{n} \lesssim 0.25$. The easiest way to realize this is to increase the cavity length L, thereby reducing the linewidth κ and the minimum occupancy $\bar{n}_{\mathrm{min}}$, which is proportional to κ^2 assuming $\Delta = -\Omega_m \gg \kappa$ (see Equation (A.61)). Concretely, using our current cavity mirrors we can extend L up to $\sim 25\,\mathrm{mm}$ based on the cavity stability condition in Equation (2.6). In this case, we expect $\bar{n}_{\mathrm{min}} \sim 5 \times 10^{-3}$. It remains to be tested whether such a low occupancy can actually be achieved in practice given the non-negligible classical laser noise and mirror noise currently present in our experiment (see Section 2.3.2.2).

The next challenge after improving the ground-state cooling is to spectrally filter out the unscattered light pulses at the cavity output. This can be achieved with narrow linewidth ($\kappa_f \ll \Omega_m$) Fabry-Pérot filter cavities [115, 116], whose resonance frequencies are stabilized to the mechanical sidebands, so that the scattered light transmits through

and the write and read pulses are reflected from the filter cavity. This filtering is necessary in order to avoid the detection of unscattered photons coming directly from these pulses, which would obscure the photon counting signal. In this context, an important figure of merit is the ratio R_+ between the Bose enhanced Stokes scattering rate $(\bar{n}+1)\Gamma_+$ and the photon flux corresponding to the blue-detuned pulse $n_c\kappa$ at the cavity output, where we set the outcoupling efficiency $\eta_c = 1$, without loss of generality. Using Equation (A.54), $\Delta = -\Omega_m$ and assuming $\bar{n}+1 \approx 1$, we get

$$R_+ \approx \frac{4g_0^2}{\kappa^2}. \tag{2.38}$$

With the estimated parameters of the aforementioned 25-mm-long cavity $g_0/2\pi \approx 8.4\,\mathrm{Hz}$ and $\kappa/2\pi \approx 370\,\mathrm{kHz}$, Equation (2.38) yields $R_+ \approx 2\times10^{-9}$. This means that the filter cavities have to suppress the write pulse by more than nine orders of magnitude while enabling low-loss transmission of the scattered light. We are currently implementing and testing different filter cavities to solve this rather challenging problem.[14]

In the long run, implementing the scheme to generate mechanical Fock states using our MiM system may open up more possibilities, such as phonon counting [117] and phonon control to create superposition states [118], as well as the generation of phonon-added coherent states [119]. We could also perform quantum-state tomography on the mechanical Fock state [120, 121] using backaction evasion measurements with two optical tones [73] or short pulses [122, 123]. Finally, we envision quantum entanglement between two mechanical resonators via the DLCZ protocol [124], as demonstrated in [125, 126]. The DLCZ protocol may also be used to entangle our SiN membrane with an atomic spin ensemble such as that in [127].

2.5 Conclusion

In conclusion, we have demonstrated ground-state cooling using an ultrahigh-Q SiN membrane in a MiM system. The phonon occupancy, determined via sideband thermometry, approaches the cooling limit set by radiation pressure backaction. Moreover, we have studied the behavior of the system when driving the cavity with two beam, one of which is resonant with the optical cavity and introduces additional backaction noise. In the future, our MiM system can be used to exploit the polarization degree of freedom of a birefringent cavity for sideband thermometry, and to realize long-lived single-phonon Fock states via a pulsed scheme.

[14] The setup for spectral filtering is designed and constructed by I. Galinskiy.

Chapter 3

Carrier-mediated forces in coupled quantum wells

3.1 Introduction

Optomechanical systems most commonly utilize radiation pressure to couple light and mechanical motion. They rely on amplifying the weak momentum transfer of each photon through high-finesse optical cavities, compensating for the fact that the single-photon coupling rate g_0 is small compared to the mechanical frequency and cavity linewidth. To enhance the optomechanical interaction researchers mainly address the properties of the optical and mechanical resonators. An example of the latter is presented in Chapter 1 of this thesis, which deals with improving the quality factors and effective masses of nanomembranes. On the other hand, high-finesse optical resonators with better confinement of the light are being developed [128–130].

As an alternative to these approaches, it has been suggested to exploit other physical mechanisms than radiation pressure to mediate the interaction with potentially much larger forces exerted per single photon. This could be done with mechanical resonators made of optically active semiconductor materials which absorb photons, create charge carriers and enable coupling to the mechanical motion via the electronic degrees of freedom. Examples of this are photothermal coupling [131, 132] and piezoelectricity [133, 134]. The latter was recently demonstrated in [135], where optically generated electrons and holes in a gallium arsenide (GaAs) cantilever are spatially separated by means of a built-in electric field and thus induce a piezoelectric force that actuates the cantilever. Interestingly, in this system cooling and amplification of the fundamental mechanical mode can be realized without the need of an optical cavity. This is because of a feedback between motion and optical absorption at the edge of the electronic bandgap, mediated by the deformation potential which quantifies the change in the energy bands due to the strain in the cantilever. While at this point the effect only allows cooling by about a factor of two from a bath temperature of 9.4 K, the experiment provides a first glimpse of the rich physics that systems with carrier-mediated optomechanical coupling can benefit from.

In 2012 researchers in our group experimentally demonstrated that local heating due to the non-radiative decay of optically generated carriers in GaAs results in photothermal forces much stronger than radiation pressure [132]. Using these forces in combination with a low-finesse cavity they optically cooled a mechanical mode of a GaAs membrane [136] from 300 K to an effective temperature of 4 K. To reach lower temperatures, it was suggested to employ forces originating directly from the deformation potential. This should not be confused with the feedback mechanism implemented in [135] and mentioned above; the proposal was based on the fact that the excitation of carriers into the conduction band entails an increase of the lattice constant and hence a hydrostatic stress. So far this effect has only been observed in optomechanical resonators with GHz frequencies [137], whose periods of oscillation match the typical carrier lifetime in GaAs of several ns. For nanomembranes in the $\sim$ MHz regime, the lifetime needs to be enhanced by almost three orders of magnitude. As was suggested in the work of our group, this can readily be achieved with a quantum well structure.

The work presented in this chapter is motivated by this idea. We study optomechanical forces induced by optically generated, long-lived electron-hole pairs (EHPs)[1] in coupled quantum wells (CQWs) embedded in a nanomembrane. Identifying contributions from both the piezoelectric effect and the deformation potential, we find that these forces are much larger than expected from radiation pressure. Furthermore, the carrier-induced forces respond with a delay which matches the independently measured carrier lifetimes in the CQWs. We envision that the delay can be harnessed as the retardation mechanism necessary to enable dynamical backaction cooling and amplification. This approach is in contrast to radiation-pressure-based systems where the retardation is provided by the finite storage time of light inside an optical cavity [138] (see also Appendix A.3.2).

Our description in this chapter closely follows our published work [4], which was conducted in collaboration with the Quantum photonics groups at NBI and ETH in Zürich[2]. In Section 3.2.1 we first present our device focusing on its mechanical and optical properties. Notice that a discussion of the device fabrication process[3] is not part of this thesis and can be found in the Supplementary Information of [4] and [139]. In Section 3.3 we distinguish and study the carrier-mediated forces by means of driven response measurements. In Section 3.4 we discuss the feasibility of using the carrier-mediated forces for cavity optomechanics. Finally, we conclude this chapter in Section 3.5.

[1] In what follows we often use the terms EHPs and (charge) carriers interchangeably.

[2] The group leaders of the two groups are P. Lodahl and A. İmamoğlu, respectively.

[3] The device fabrication was carried out by L. Midolo.

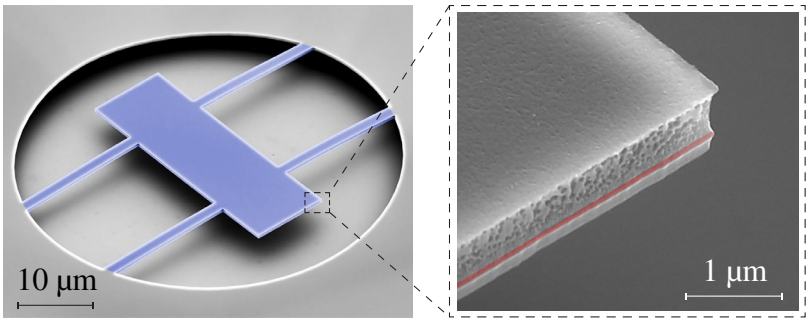

Figure 3.1: SEM images of a free-free membrane with CQWs. Left: The membrane is suspended by four thin beams, colored in blue. Right: A close-up image shows the membrane cross section with the vertical position of the CQWs marked in red. Adapted from [4].

3.2 Device design

3.2.1 Free-free membranes

In our experiments we use free-free nanomembranes [140] which consist of a 40 µm × 12.73 µm rectangular plate with a thickness of 562 nm, suspended by four thin beams. Such a device is shown on the left hand side of Figure 3.1. It is made of a GaAs-based heterostructure, detailed in Section 3.2.2, including two CQWs where carriers are optically generated. Due to the off-center position of the CQWs, the forces induced by the carriers cause a bending motion and thus enable coupling to the symmetric bending mode of the membrane. The mechanical modes of the free-free membrane and their properties are discussed further in the following.

3.2.1.1 Eigenmodes

The motion of the nanomembrane is analyzed using our home-built Michelson interferometer, whose functionality is described in Section 1.2.1. With regard to the optically active materials used in the device, it should be noted that the probe laser at a wavelength of $\lambda = 1064\,\text{nm}$ is energetically well below any interband optical transition in the CQWs. Hence, at this point, we do not excite any carriers but simply observe the out-of-plane membrane motion with the probe laser.

We first measure the thermally excited motion of the nanomembrane in vacuum at $T = 300\,\text{K}$ probing near the center of the rectangular plate and use an incident optical power of 800 µW focused to a spot radius of $\sim 1\,\mu\text{m}$. The normalized displacement PSD extracted from this measurement is shown in Figure 3.2, where we find a number of sharp peaks in the MHz regime. The two peaks that are of interest for our experiment are at mode frequencies of $\Omega_{\text{M1}}/2\pi = 0.828\,\text{MHz}$ and $\Omega_{\text{M2}}/2\pi = 1.602\,\text{MHz}$, referred to in the following as mode M1 and M2, respectively. Their simulated displacement patterns are shown on the right hand side of Figure 3.2. M1 can be described as the fundamental drum mode in which the entire central plate is displaced without deforming. M2 exhibits a symmetric bending motion with significant displacement and maximum curvature in

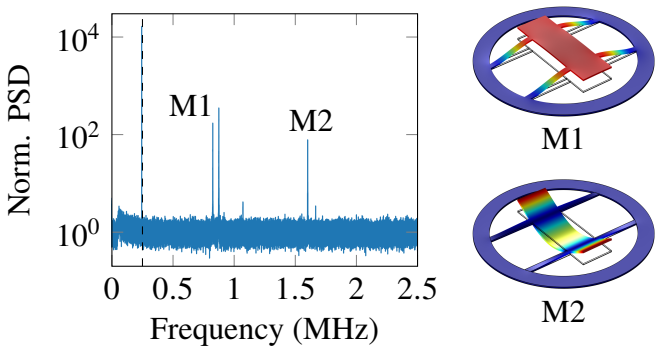

Figure 3.2: Eigenmodes of a free-free membrane. Left: Displacement PSD normalized to SN measured close to the center of the membrane with mode M1 at a frequency of $\Omega_{M1}/2\pi = 0.828\,\text{MHz}$ and M2 at $\Omega_{M2}/2\pi = 1.602\,\text{MHz}$. The vertical dashed line indicates the calibration peak at a frequency of 250 kHz. Right: Simulated mode shapes of membrane for the two modes.

the center of the plate. Notice that the four thin beams are not displaced vertically as their anchor points coincide with the nodes of M2. This feature results in a suppression of phonon-tunneling loss as demonstrated in [140].

Due to its curvature, mode M2 efficiently couples to the bending force induced by the EHPs in the CQWs. We therefore focus primarily on M2 in the following and first experimentally verify the simulated mode shape by applying the raster-scan technique detailed in Section 1.2.1.3. For this we drive a PZT that is mounted close to the sample in the vacuum chamber and at each measurement point of the scan the drive frequency swept over the resonance at Ω_{M2}. The resulting signal is analyzed with a lock-in amplifier and is fit to the expression for the mechanical susceptibility (see Equation (A.15)) to extract the amplitude and the phase of the motion at resonance. From these data, we compose a displacement map, shown in Figure 3.3, revealing large motion at the long ends of the rectangular plate and near the center. As represented by an opposite sign of the displacement, the center and the ends oscillate out of phase, which is expected from the simulation.

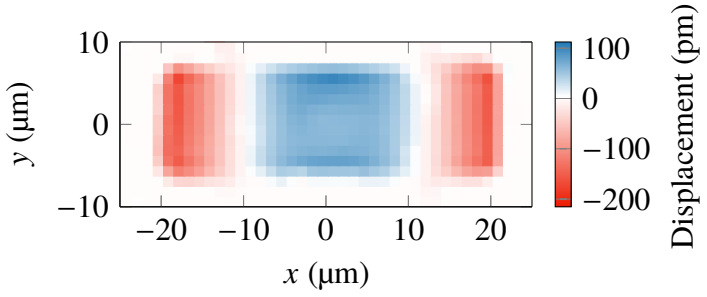

Figure 3.3: Identification of the symmetric bending mode. We spatially scan the membrane and measure the displacement while mechanically exciting its motion at a mode frequency of $\Omega_{M2}/2\pi = 1.643\,\text{MHz}$ with a PZT. The phase of the displacement is used to extract the sign of the displacement. Redrawn from [4].

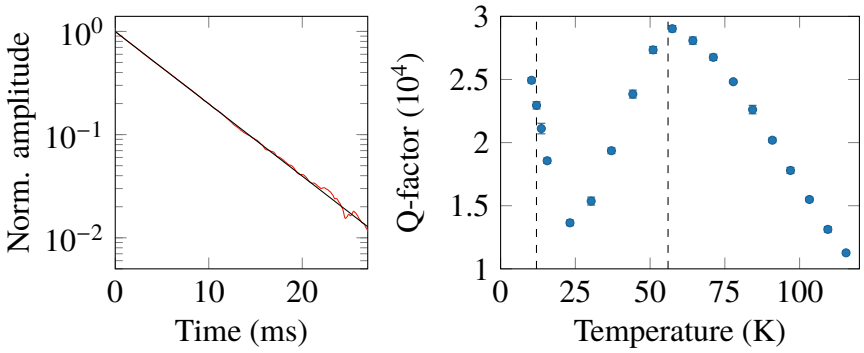

Figure 3.4: Quality factor of the symmetric bending mode M2. Left: Ringdown measurement (red) of mode M2 at a temperature of $T = 57.4\,\mathrm{K}$ and exponential fit (black) resulting in a maximum quality factor of $Q = 2.8 \times 10^4$. Right: Quality factor as a function of temperature. Dashed lines at 12 K and 56 K indicate the temperatures at which the linear expansion coefficient of GaAs $\beta \approx 0$. Redrawn from [4].

3.2.1.2 Quality factor

To measure the quality factor of mode M2 we use ringdown fitting, described in Section 1.2.1.4. In Figure 3.4 we show data obtained at a temperature of $T = 57.4\,\mathrm{K}$, from which we extract that $Q = 2.8 \times 10^4$. This result is comparable to that found for the same type of membranes in [140], despite the different temperature and membrane material used. The temperature behaviour of Q for our devices is interesting since it varies by almost a factor of three in the range of 10...100 K, as can be seen on the right hand side of Figure 3.4. In particular, we find that the quality factor peaks near 12 K and 56 K, which coincide with the zero-crossings of the coefficient of thermal expansion β for GaAs and other III-V compounds used in the heterostructure [141, 142]. We are led to conclude that thermoelastic damping, which is proportional to the square of β [41], plays a major role in the dissipation of mechanical energy in our nanomembranes [143]. Other than that, we suspect loss due to defects at the interfaces and surfaces of the different layers in the heterostructure [144] but have yet to confirm this hypothesis.

3.2.2 Coupled quantum wells

3.2.2.1 Heterostructure and band diagram

The crucial ingredient to extend lifetimes of EHPs in our device enabling large carrier-mediated forces is an epitaxially-grown GaAs-based heterostructure[4]. In Figure 3.5 we show an illustration of this heterostructure which constitutes the 562-nm-thick membrane cross section. At the top and bottom side are p and n doped GaAs layers[5], respectively, functioning as electrical contacts for a bias voltage V_b. Embedded in between two AlGaAs layers are 9-/5-/9-nm InGaAs/GaAs/InGaAs CQWs which host the

[4]The wafer was grown by J. Miguel-Sanchez at ETH.

[5]Each of the two layers has a doping concentration of $2 \times 10^{18}\,\mathrm{cm}^{-3}$.

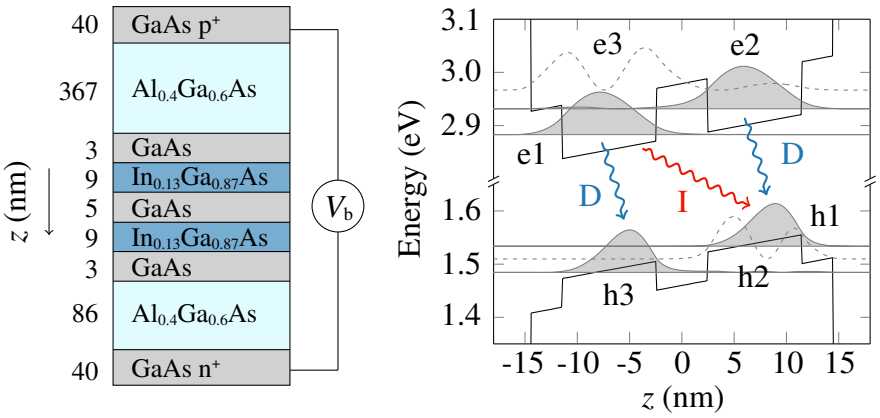

Figure 3.5: GaAs heterostructure with coupled quantum wells. Left: Illustration of membrane cross-section. The heterostructure is 562 nm thick, includes InGaAs/GaAs CQWs and provides two doped GaAs layers as electrical contacts for the bias voltage V_b. Right: Band diagram of CQW at $V_b = -1$ V where the edges of the conduction and valence bands are shown in black. The squared carrier wavefunctions and the corresponding energy levels are shown in solid and dashed gray lines. Direct (D) and indirect (I) optical transitions are indicated with arrows. Adapted from [145].

long-lived EHPs in our experiment. A band diagram of the CQWs is shown on the right hand side of Figure 3.5, including the first three wavefunctions of electrons e1, e2, e3 and holes h1, h2, h3. The wavefunctions are found by solving the one-dimensional single-particle Schrödinger equation numerically.[6] The band diagram is shown for $V_b = -1$ V and a bias electric field $E_b \approx V_b/h + E_0 = 19\,\mathrm{kV\,cm^{-1}}$, where $h = 562$ nm is the membrane thickness and $E_0 = 30\,\mathrm{kV\,cm^{-1}}$ is the built-in electric field due to the doped layers. Here the EHP ground state consist of e1 and h1, spatially separated by the thin potential barrier between the CQWs. This means that the state is indirect, in contrast to the direct states, in which electrons and holes reside in the same quantum well. The two direct states are formed by e1 and h3, as well as e2 and h1.

As described below, our experiments are performed at a temperature of $T = 12$ K. It should be noted that at this temperature EHPs in the CQWs can occur in two different phases. At relatively low densities they bound as insulating pairs, known as excitons, due to coulombic attraction. Increasing the carrier density or the sample temperature leads to a transition into a conducting phase, in which excitons ionize and form a EHP plasma (Mott-transition). The two phases exhibit slightly different recombination energies and lifetimes as demonstrated in [145, 146]. For our discussion below we will not make a distinction between the two phases.

3.2.2.2 Photoluminescence spectra

EHPs generated in the CQWs recombine radiatively via the interband transitions sketched in Figure 3.5, allowing us to study the carrier dynamics by means of photoluminescence (PL) measurements. To do this, we first cryogenically cool the sample

[6] This calculation was carried out by P. Tighineanu.

to $T = 12\,\mathrm{K}$ and focus continuous-wave, above-bandgap laser light at a wavelength of $\lambda = 785\,\mathrm{nm}$ to a spot radius of $\sim 0.75\,\mu\mathrm{m}$ at the center of a membrane using a microscope objective. PL emitted from the CQWs is collected by the same objective and passes through a longpass dichroic mirror with a cutoff wavelength of 875 nm rejecting directly reflected light from the sample. Then, a spectrum of the PL is obtained by a spectrometer.

Figure 3.6 shows examples of such a spectrum in the wavelength range from 890 nm to 950 nm at $V_\mathrm{b} = 0\,\mathrm{V}$. We find a small peak at around 935 nm corresponding to the radiative recombination of the indirect ground state (I) and a large peak around 905 nm that is due to the two direct transitions (D). When probing the PL at the center of the membrane the peaks in the spectrum are red shifted by a few nm and slightly broadened in comparison to the peaks found when measuring on the bulk. We attribute these differences to stress release at the membrane and surface effects, slightly modifying the band structure.

The energies of the electron and hole states in the CQWs can be shifted by changing the applied electric field E_b, or rather the bias voltage V_b. This effect is known as the quantum confined Stark shift [147] and is characterized in our device by extracting the peak values in the PL spectrum for different values of V_b, as shown on the right hand side of Figure 3.6. We find that the wavelength of I decreases linearly with about $-20\,\mathrm{nm\,V^{-1}}$. The wavelengths of D, on the other hand, are nearly constant between $V_\mathrm{b} \approx 0\,\mathrm{V}\ldots1\,\mathrm{V}$. For smaller voltages our model predicts that they shift linearly with V_b. This is a result of the overall skew of the energy bands visible in Figure 3.5, decreasing the separation between the valance band and the conduction band within the same quantum well. Notice also that the wavefunctions are reshaped so that they are predominantly located at the opposite corners of the quantum well, indicating that the transition D becomes slightly indirect.

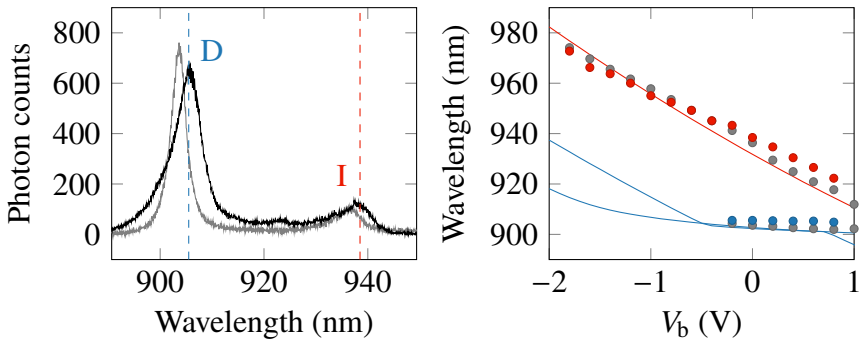

Figure 3.6: PL spectra of optical transition in the CQWs. Left: PL spectra of the CQWs measured in bulk (gray) and at the center of a membrane (black) for a bias voltage of $V_\mathrm{b} = 0\,\mathrm{V}$. The wavelength of the peaks corresponding to the indirect (I) and direct transitions (D) are marked with dashed lines. Right: Wavelength of the peaks for different values of V_b. We confront the data measured on the membrane (colored dots) with calculations for D (blue) and I (red). Gray dots are the peak values when measuring on the bulk.

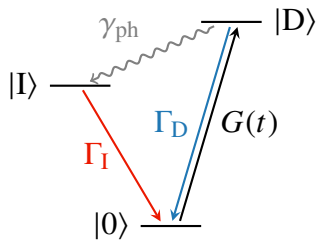

Figure 3.7: Three-level scheme for the lowest EHP states and transitions. In the scheme $G(t)$ denotes the time-dependent generation rate and γ_{ph} an acoustic phonon-mediated decay. Γ_D and Γ_I are the radiative decay rates of the direct state $|D\rangle$ and indirect state $|I\rangle$, respectively. Adapted from [4].

3.2.2.3 Carrier decay dynamics

We will now turn our attention towards the decay dynamics of carriers in the CQWs. To begin with, we assume a model based on the three-level scheme shown in Figure 3.7 and derive rate equations for the area densities n_I and n_D of carriers in the indirect state $|I\rangle$ and direct state $|D\rangle$, respectively. Γ_I and Γ_D denote the corresponding radiative decay rates and the rate γ_{ph} refers to a non-radiative decay from $|D\rangle$ to $|I\rangle$ mediated by acoustic phonons.[7] The state $|0\rangle$ denotes the reservoir from which EHPs are generated. The small overlap between the wave functions e1 and h1 in the indirect state implies that the probability of photoabsorption α_I associated with the transition I is negligible ($\alpha_I \approx 0$). Therefore, we assume that above-bandgap laser light used in our experiments only generates carriers via the direct transition D and introduce the time-dependent generation rate per unit area $G(t) = \alpha_D I(t)/\hbar\omega_l$, where $\alpha_D = 0.0214$ [145] is the absorption probability corresponding to transition D, $I(t)$ is the intensity of the incident light, and $\omega_l = 2\pi c/\lambda$. This leads us to the following rate equations:

$$\dot{n}_D(t) = G(t) - \gamma_{ph} n_D(t), \tag{3.1}$$

$$\dot{n}_I(t) = \gamma_{ph} n_D(t) - \Gamma_I n_I(t). \tag{3.2}$$

In Fourier domain, where $d/dt \rightarrow i\Omega$, they can be easily solved. Following [148], we simplify the solution by assuming that the phonon-mediated decay is fast and $\gamma_{ph} \gg \Gamma_D, \Omega$. Then, we get $n_D(\Omega) \approx 0$ and

$$n_I(\Omega) \approx \frac{G(\Omega)}{\Gamma_I + i\Omega}. \tag{3.3}$$

Evidently, all the carriers are now found in the state $|I\rangle$. We are interested in their dynamics in response to an amplitude-modulated optical pump with $I(t) = I_0(\sin(\Omega t) + 1)$, where I_0 is the amplitude and Ω is the frequency of the modulation. By inspection of Equation (3.3) we see that if $\Gamma_I \gg \Omega$ the overall carrier density is relatively small and modulated in phase with the pump. On the other hand, if $\Gamma_I \leq \Omega$ a much larger density $|n_I|$ and a phase shift $\arg(n_I) \leq -\pi/4$ are expected. This regime is realized

[7] Notice that EHPs cannot transition in the opposite direction via phonons since the energy difference between the two states $\Delta E \approx 0.05$ eV is much larger than $k_B T \approx 1$ meV, where $T = 12$ K.

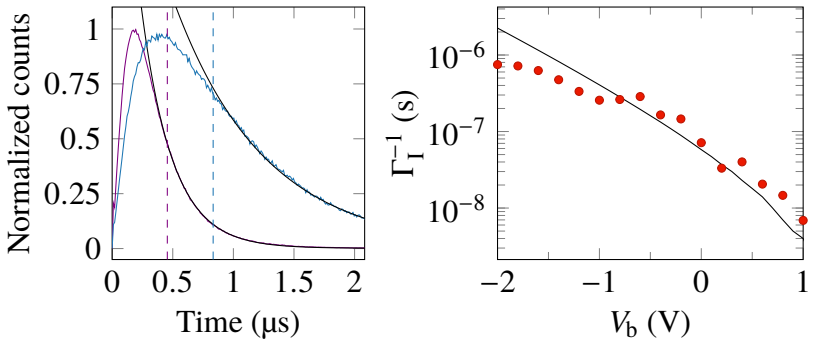

Figure 3.8: Decay dynamics of the charge carriers. Left: Time-resolved PL measurements at the indirect transition wavelength for bias voltages V_b of −2 V (blue) and −1 V (purple), where black lines are fits. Colored dashed lines indicate the start time of the fits. The photon counts are normalized to the peak value in each trace. Right: Extracted lifetimes for Γ_I (red dots) as a function of V_b, as well as calculated lifetimes of the indirect transition (black). Redrawn from [4].

by our device and is interesting because it enables strong carrier-mediated forces and a retardation mechanism necessary to implement dynamical backaction cooling.

In order to measure the lifetime Γ_I^{-1} we modify our PL setup (see Section 3.2.2.2) in the following way: Instead of using continuous-wave laser light to excite carriers, we send picosecond light pulses to the center of the membrane and then spectrally filter the PL in a narrow bandwidth around the indirect transition wavelength. After that, the light is detected by an APD whose photocurrent is recorded over time. This measurement is repeated after each of many consecutive pulses until the accumulated photon counts are well-above the background noise. As exemplified in Figure 3.8, the resulting signal quickly builds up as carriers transition into the indirect state via acoustic phonons and then slowly decays. To extract Γ_I^{-1} we fit an exponential function to the tail of the curve and repeat the procedure for different V_b. The result, shown on right hand side of Figure 3.8, demonstrates that we can tune the lifetime over more than two orders of magnitude reaching a maximum value of $\Gamma_I^{-1} = 749.5(4)$ ns at $V_b = -2$ V. This behavior agrees well with a calculation[8] based on Fermi's Golden rule, in which we numerically evaluate the overlap of the wave functions of the indirect state $|I\rangle$ (e1 and h1) and assume no free parameters. Discrepancies between the data and the model are found in the voltage range from −2 V to −1 V, likely due to fast surface recombination at the edges of the membrane.

3.2.2.4 Carrier diffusion

As a next step, we consider the diffusion of carriers across the membranes. This is particularly important because of the long lifetimes achieved in our CQWs. For similar structures the diffusion has been measured via time-resolved optical imaging in [149] showing that EHPs can travel over large distances of several 100 µm. In our PL setup we do not have access to such a measurement technique and therefore we analyze the

[8]This calculation was carried out by P. Tighineanu.

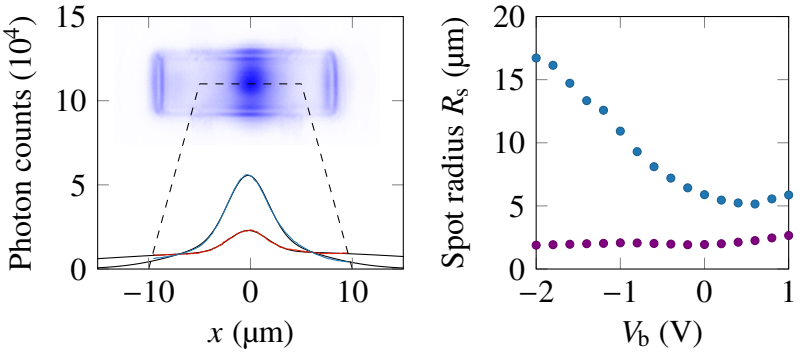

Figure 3.9: Imaging of carrier diffusion. Left: Imaged PL (inset) and cross section along the horizontal dashed line for bias voltages of 0 V (blue) and −2 V (red). Black solid lines are fits using double-Gaussian functions. Right: Spot radii extracted from the fits as a function of bias voltage. Redrawn from [4].

diffusion by imaging the time-averaged PL onto a CCD camera instead. As before, this is done while the center of the membrane is illuminated with laser light at a wavelength of 785 nm and a spot radius of $\sim 0.75\,\mu$m. On the left hand side of Figure 3.9, we present an image captured with the CCD camera for $V_b = 0\,$V. Here the PL spreads over a larger area than the excitation spot. At the membrane edges we see bright lines that are likely due to scattering of the PL and are thus not considered further. Near the center we analyze the cross section of the image along the x-direction and find a peak that is well-reproduced by a double-Gaussian function. We fit the data and for each Gaussian extract the variance, here referred to as the spot radius R_s. Repeating this measurement at different values of V_b results in the plot shown on the right side of Figure 3.9. It can be seen that one of the two spot radii is overall larger with a maximum value of $R_s = 16.7\,\mu$m at $V_b = -2\,$V and changes by more than a factor of three in the measured range. We attribute this feature to the PL of the transition I, associated with the recombination of indirect EHPs that have widely tunable lifetimes. Accordingly, the nearly constant and generally smaller spot radius shown in Figure 3.9 is likely due to PL of the direct transition D.

Based on the above assumption we extract the diffusion constant $D = R_s^2\Gamma_I/2$, considering only the largest measured spot radii at $V_b \leq -1\,$V and the corresponding lifetimes Γ_I^{-1} shown in Figure 3.8. The result is $D = 2.0(3)\,\mathrm{cm^2\,s^{-1}}$ which is comparable to the values reported in [149]. With this, we are now ready to model the area density of the carriers $n_I(x, y, \Omega)$ in response to an incident laser beam modulated at a frequency Ω, where we also explicitly write down the dependence on the position (x, y). Equation (3.3) is extended to include the diffusion of EHPs across the membrane in the following way:

$$D\nabla^2 n_I(x, y, \Omega) \approx (\Gamma_I + i\Omega)\, n_I(x, y, \Omega) - G(x, y, \Omega). \tag{3.4}$$

While it is possible to solve this equation analytically for the case of an infinitely large membrane, we need to consider the more complicated boundary conditions defined by the finite, rectangular shape of the membrane and solve Equation (3.4) numerically as part of the finite-element simulations in Section 3.3.2. In these we choose the

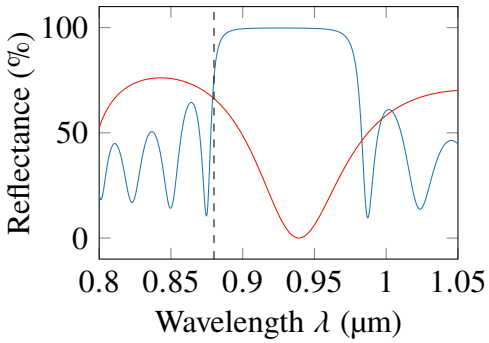

Figure 3.10: Spectral reflectance of the membrane and the DBR. Using the TMM we calculate the reflectance of the DBR $|r_{\mathrm{dbr}}|^2$ (blue), as well as the membrane $|r_{\mathrm{m}}|^2$ (red) as a function of wavelength, assuming a temperature of $T = 300\,\mathrm{K}$. The dashed black line indicates the wavelength $\lambda = 880\,\mathrm{nm}$ used in our experiments.

modulation frequency on resonance $\Omega/2\pi = \Omega_{\mathrm{M2}}/2\pi \approx 1.6\,\mathrm{MHz}$ and a Gaussian beam spot so that the generation rate reads

$$G(x, y, \Omega_{\mathrm{M2}}) = \frac{\alpha_{\mathrm{D}}}{\hbar\omega_{\mathrm{l}}} e^{-\frac{x^2+y^2}{2R_{\mathrm{s}}^2}} I_0\left(\sin(\Omega_{\mathrm{M2}}t)\right). \tag{3.5}$$

The other parameters correspond to those used in our driven response measurements (see Section 3.3.3), that is to say, the power of the modulated light is $P_0 = \pi I_0 R_{\mathrm{s}}^2/4 = 0.5\,\mu\mathrm{W}$ and $R_{\mathrm{s}} = 1\,\mu\mathrm{m}$.

3.2.3 Integrated optical cavity

Our device features a Fabry-Pérot cavity formed by the nanomembrane and an integrated distributed Bragg reflector (DBR). While studying carrier-mediated forces we avoid driving any optical resonances of this cavity, which is why it plays no role throughout most of this chapter. However, in Section 3.4 we discuss how the integrated cavity could be used for optical cooling via carrier-mediated forces.

3.2.3.1 Distributed Bragg reflector

The nanomembrane is released by etching away a 2-μm-thick sacrificial layer exposing a DBR below the membrane. The DBR consists of 20 alternating layers of GaAs and AlAs with thicknesses of 66 nm and 79 nm, respectively. It is optimized for the wavelength range of the indirect transition I (900 nm to 950 nm) as can be seen in Figure 3.10 where we plot the reflectance $|r_{\mathrm{dbr}}|^2$ of the DBR versus wavelength calculated via the TMM (see Appendix A.4). At a wavelength of $\lambda = 880\,\mathrm{nm}$, used in our driven response measurements, we are at the edge of the stop band and get $|r_{\mathrm{dbr}}|^2 \approx 76\,\%$. Furthermore, the membrane has a reflectance of $|r_{\mathrm{m}}|^2 \approx 66\,\%$ meaning that the finesse of the integrated cavity is expected to be $\mathcal{F} \approx 9$.

3.2.3.2 Cavity characterization

The vertical position of the membrane above the DBR and thus the cavity length L are not well-defined by the thickness of the sacrificial layer. This is because the membrane buckles and deforms when released, as was initially observed in scanning electron microscope images of the device. To investigate this further, we use a confocal microscope and perform topography measurements of a nanomembrane. In Figure 3.11 we show a cross section of this measurement along the x-direction, where the height profile of the 40 µm-long plate is visible as a curved graph in the center. Compared to the profile of the bulk, visible near the edges of the plot, the membrane is buckled upwards by more than 1 µm and is deformed in a U-shape around the center. This behavior is expected from the stress release of different layers in the heterostructure. By fitting a quadratic function to the profile of the membrane and subtracting its thickness $h = 562\,\text{nm}$, we extract the position-dependent cavity length $L(x)$. Furthermore, we calculate the second derivative with respect to x and find the radius of curvature in the center ($x = 0$) to be $R_c = 578(2)\,\mu\text{m}$. R_c is positive by choice of the coordinate system, yet technically the membrane constitutes a convex mirror with negative radius of curvature $-R_c$ in relation to the integrated cavity. This means than the cavity is unstable as the condition $1 - L(0)/(-R_c) \leq 1$ is not satisfied [97].

As a next step, we characterize the cavity using a focused laser at $\lambda = 880\,\text{nm}$ with a spot diameter of $\sim 2\,\mu\text{m}$. We measure the reflectance at various positions x across the deformed membrane and find a resonance as shown on the right hand side of Figure 3.11. Here we translate each position x into a cavity length via $L(x)$. The resonance at $L \approx 3.1\,\mu\text{m}$ has a FWHM of $\delta L = 170(7)\,\mu\text{m}$ resulting in a finesse of $\mathcal{F} = \lambda/2\delta L = 2.6(1)$, which is quite different from the expected value mentioned above. The discrepancy could be because of photo absorption in the membrane, which was not taken into account in our TMM. Furthermore, the unstable nature of the cavity may cause diffraction loss at the membrane's edges.

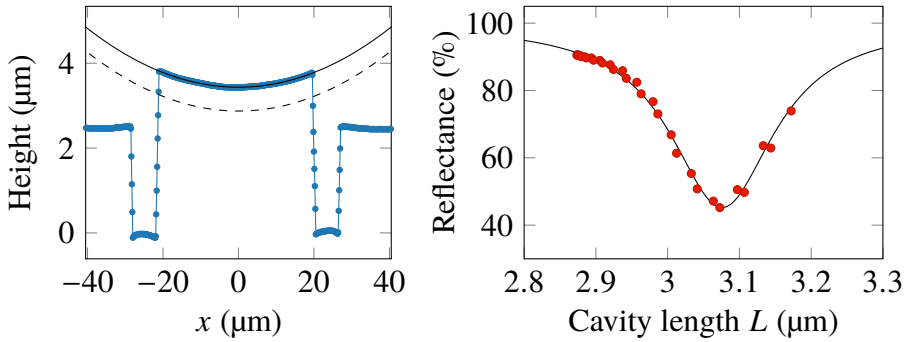

Figure 3.11: Cavity characterization at room temperature. Left: Topography measurement along the x axis (blue dots) and quadratic fit to the membrane surface (black solid line). Subtracting the membrane thickness from the fit (dashed line) we determine the length of the integrated cavity. Right: Reflectance of the integrated cavity at $\lambda = 880\,\text{nm}$ vs cavity length as measured (red dots) and fitted (solid line). Redrawn from [4].

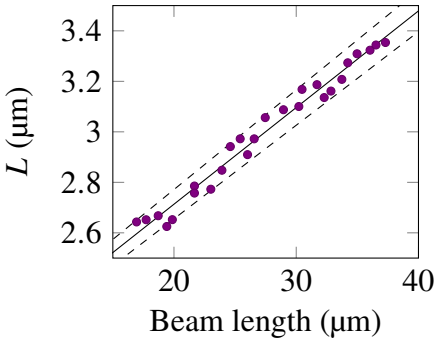

Figure 3.12: Dependence of the cavity length on membrane buckling. Cavity length L extracted at the center of each of 26 nanomembranes with different beam lengths (purple). A linear fit with a slope of 0.038(1) is shown as a black line, while the 1-sigma standard deviations to the fit are indicated with dashed lines. Errors of the data points are < 1 % and are not shown.

At a fixed wavelength and probing position we can adjust the cavity detuning by changing the length L. To this end, we control the buckling by varying the length of the four thin beams that suspend the central plate. We fabricate a sample including an array of 26 membranes with beam lengths ranging from 17 µm to 37 µm and characterize their topography with the confocal microscope. For each membrane we extract the cavity length averaged over an area of 10 µm × 10 µm at the center. Figure 3.12 shows the result of this measurement, where we find a linear relation between L and the beam length. From a fit to the data we get a slope of 0.038(1) and a 1-sigma standard deviation on the cavity length of $\sim$ 58 nm. The latter serves as a measure for the precision with which we can target a given L using this method. In comparison, this is about three times smaller than δL, meaning that at least a coarse adjustment of the cavity detuning is possible. It should be noted that the measurements were performed at room temperature and when cooling the membranes down to $T = 12$ K the buckling changes. Thus far this change has not been characterized thoroughly.

For the measurements presented in Section 3.3.3 we exclude membranes that feature a resonance in the center at $T = 12$ K. This is because we want to quantify the behavior of carrier-mediated forces at a given input power without having to take into account the enhancement of the light inside the cavity or any optomechanical effects. In Section 3.4 we will discuss how the integrated cavity could be of use in regard to the implementation of a cavity optomechanical system.

3.3 Carrier-mediated optomechanical forces

3.3.1 Physical mechanisms

Let us now consider the forces mediated by optically generated EHPs in the CQWs. There has been a number of thorough experimental studies on the different physical mechanisms underlying these forces in various materials, typically in form of pump-

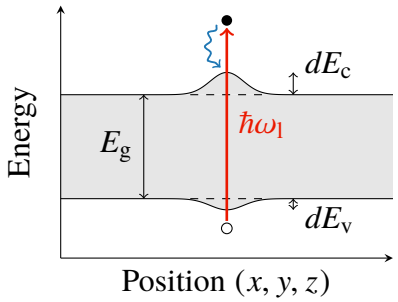

Figure 3.13: Schematic illustration of a band diagram upon the generation of an EHP. The absorption of a photon with energy $\hbar\omega_l > E_g$, indicated by a red arrow, promotes an electron (black circle) to the conduction band and creates a hole (white circle) in the valence band. As a result, the band gap (gray shaded area) locally increases by $dE_c + dE_v$ as described by the deformation potential. The dashed lines show the band gap edges without the presence of an EHP. The blue line indicates intraband relaxation processes of the electron mediated by acoustic phonons.

probe measurements with femto-second lasers to temporally resolve acoustic phonons in the GHz or THz regime. Following a comprehensive review of this topic in [150], we identify three mechanisms relevant for our device that will be described in the sections below.

3.3.1.1 Deformation potential

The deformation potential refers to the interdependence of strain and energy of the electronic distribution in the crystal. At the microscopic level it describes the fact that the generation of an EHP alters the interatomic bonds in the crystal, leading to a new equilibrium position of the atoms and a new lattice constant. The result is a local deformation of the crystal, or rather a volumetric strain $d\epsilon$, accompanied by a change in the bandgap energy E_g, as is illustrated in Figure 3.13. Here we distinguish the contributions from the conduction band dE_c and the valence band dE_v, and for each define a deformation potential parameter

$$d_{c/v} := \frac{dE_{c/v}}{d\epsilon}. \tag{3.6}$$

The values depend only on the material and have been measured in GaAs to be $d_e = -5.3\,\text{eV}$ and $d_h = 2.7\,\text{eV}$ [151]. Given a distribution of electrons n_e and holes n_h in the material the hydrostatic stress reads

$$\sigma_{dp} = d_c n_e - d_v n_h. \tag{3.7}$$

In order to apply Equation (3.9) to our device we first need to consider that the CQWs spatially separate electrons and holes in the indirect state I. In the z-direction the separation is described by the wavefunctions e1 and h1 introduced in Section 3.2.2 which we approximate by normalized Gaussian profiles $\Psi_{e/h}$ peaked at the center $z_{e/h}$ of

each of the two quantum wells, where the indices 'e' and 'h' refer to the electrons and holes, respectively:

$$\Psi_{\mathrm{e/h}}(z) = \frac{1}{2\sqrt{2\pi}R_{\mathrm{qw}}} e^{-\frac{(z-z_{\mathrm{e/h}})^2}{2R_{\mathrm{qw}}^2}}. \tag{3.8}$$

Here the FWHM $R_{\mathrm{qw}} = 2\,\mathrm{nm}$ corresponds to the confinement radius of the well. In the x- and y-direction the density of EHPs is described by the distribution $n_{\mathrm{I}}(x, y, \Omega)$ so that Equation (3.9) is modified as follows:

$$\sigma_{\mathrm{dp}}(x, y, z, \Omega) = n_{\mathrm{I}}(x, y, \Omega)\,(d_{\mathrm{c}}\Psi_{\mathrm{e}}(z) - d_{\mathrm{v}}\Psi_{\mathrm{h}}(z))\,. \tag{3.9}$$

We see that the stress is proportional to $n_{\mathrm{I}}(x, y, \Omega)$ and thereby directly follows the dynamics derived in Sections 3.2.2.3 and 3.2.2.4. As will be shown later the deformation potential contributes a sizeable bending force in our device, owing to the fact the CQWs are located off-center near the bottom layer of the membrane heterostructure.

3.3.1.2 Photothermal force

Figure 3.13 depicts a scenario, in which an EHP is excited by a photon whose energy $\hbar\omega_{\mathrm{l}}$ is larger than the band gap E_{g}. The excited electron quickly dissipates energy until it reaches the band gap edge. This intraband relaxation process is mediated by acoustic phonons and causes local heating in the material. The increase in temperature per EHP is given by

$$dT = \frac{\hbar\omega_{\mathrm{l}} - E'_{\mathrm{g}}}{C_{\mathrm{h}}}, \tag{3.10}$$

where C_{h} is the heat capacitance and $E'_{\mathrm{g}} = E_{\mathrm{g}} + dE_{\mathrm{c}} + dE_{\mathrm{v}}$. The numerator describes the total energy of the phonons created by the relaxation process. If the EHP undergoes non-radiative instead of radiative recombination[9], an additional heating occurs and we have to add the term $E'_{\mathrm{g}}/C_{\mathrm{h}}$ to Equation (3.10). In any case, the local heating causes hydrostatic stress in the material:

$$\sigma_{\mathrm{pt}} = -3B\beta dT. \tag{3.11}$$

Here B denotes the bulk modulus and β is the coefficient of linear thermal expansion. The phenomenon is generally known as the bolometric or photothermal force.

As previously mentioned, our group has demonstrated optical cooling of a GaAs membrane based on the photothermal force in [132]. An important detail here is the fact that the membrane was kept at a temperature of $T = 300\,\mathrm{K}$, where $\beta \approx 5 \times 10^{-6}\,\mathrm{K}^{-1}$ for GaAs [152]. In comparison, in the range of 0...15 K the linear expansion is more than two orders of magnitude smaller and vanishes at $T = 12\,\mathrm{K}$ (see Section 3.2.1.2), where we perform measurements in this work. Since σ_{pt} is proportional to β according to Equation (3.11) we expect the photothermal force in our device to be negligible.

[9]Non-radiative recombination can prevail in the prescence of surfaces and defects in the crystal.

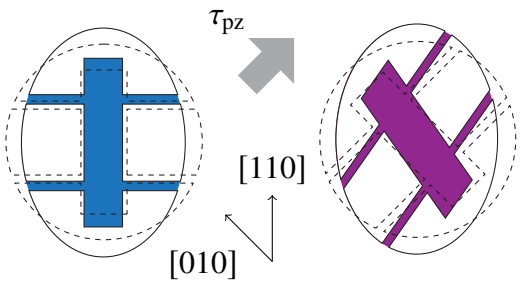

Figure 3.14: Deformation of a free-free nanomembrane due to the piezoelectric effect. We illustrate the top-view of a nanomembrane for two different orientations in purple and blue with respect to the crystallographic axes (denoted by Miller indices) when a shear stress τ_{pz} is applied. The dashed lines show the membrane outline without the stress. The deformations are exaggerated for illustration purpose.

3.3.1.3 Piezoelectric effect

The piezoelectric effect describes the coupling between mechanical stress and an electric field, initiated from electric dipoles within the material that align upon application of the stress. The reverse process in which an electric field causes a deformation of the material is also possible and the mechanism of interest here. The piezoelectric effect can be expressed by the following linear relation between the stress tensor $\tilde{\sigma}_{pz}$ and the electric field vector $\vec{E}$:

$$\tilde{\sigma}_{pz} = \tilde{e}\vec{E}, \tag{3.12}$$

where $\tilde{e}$ is the piezoelectric tensor. The latter depends on the material and has considerable components in certain crystals, ceramics, and semiconductors.

In the context of optomechanics, the effect is often used to actuate mechanical motion. An example is presented in [134], where a GHz-frequency voltage drive is applied to electrodes surrounding an aluminium nitride cavity optomechanical resonator and the excited mechanical modes are probed via optical readout. In our device a piezoelectric stress occurs upon carrier generation in the CQWs because the electrons and holes are spatially separated in the indirect state, resulting in an electric field E_{eh} applied in the z-direction across the thin GaAs barrier:

$$E_{eh}(x, y, \Omega) = \frac{q}{\epsilon_0 \epsilon_r} n_1(x, y, \Omega), \tag{3.13}$$

where q is the elementary charge, ϵ_0 is the vacuum permittivity, and $\epsilon_r \approx 13$ is the relative permittivity. To translate $E_{eh}(x, y, \Omega)$ into a frequency-dependent stress (per unit area) via Equation (3.12), we employ the piezoelectric tensor of GaAs, known to have only off-diagonal elements that result in a shear stress τ_{pz} directed along a certain crystallographic axis. Accordingly, the free-free nanomembrane is deformed as illustrated in Figure 3.14, where we consider two orientations of the membrane with respect to the crystal axes. The latter are denoted by Miller indices. It should be noted that the in-plane deformation can translate into the z-direction (out-of-plane) because it only occurs in the CQWs. Similar to the hydrostatic stress due to the deformation potential, this means that the piezoelectric force gives rise to a bending force.

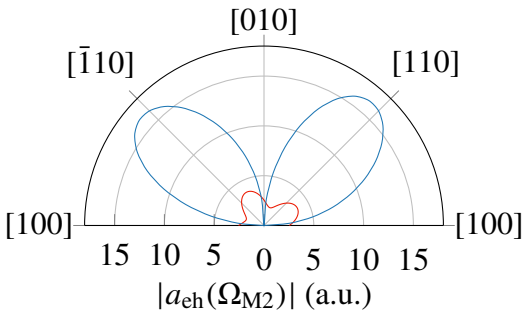

Figure 3.15: Dependence of carrier-mediated forces on the membrane orientation. Simulated magnitude of acceleration as a function of membrane orientation (indicated by the Miller indices) for the piezoelectric force (blue) and deformation potential force (red). The diffusion of carriers was neglected by assuming a short carrier lifetime, i.e., $\Gamma_I \gg \Omega_{M2}$.

3.3.2 Distinction of the forces

3.3.2.1 Simulations

How do the deformation potential and the piezoelectric effect translate into forces that drive the out-of-plane motion of our membrane? We address this question by carrying out finite-element simulations[10] using a three-dimensional geometry that consists of the free-free nanomembrane, reshaped according to the buckling and deformation characterized in Section 3.2.3.2. Furthermore, we assume a 5 µm undercut ring, whose outer ring constitutes a fixed boundary condition. Eigenfrequency analysis of the geometry reveals the mode shapes (see Section 3.2.1.1) and frequencies.[11] The latter agree to within 10 % with the measured frequencies. By multiplying the distribution of the material density ρ and the mode shape, normalized to the maximum displacement of the mode, and integrating over the entire computational domain, we determine the effective mass m_{eff} of each mode. For M2 we get $m_{eff} = 340$ pg.

The next step is to include the stresses in Equations (3.9) and (3.12), and for each calculate the overlap with M2. This gives us effective forces $F_{eh}(\Omega_{M2})$, or rather accelerations $a_{eh}(\Omega_{M2}) = F_{eh}(\Omega_{M2})/m_{eff}$. As before we are interested in the frequency component at Ω_{M2} since we want to resonantly drive M2 using amplitude-modulated light. Notice that F_{eh} and a_{eh} are derived from the complex carrier density $n_I(x, y, \Omega_{M2})$ and, in general, constitute complex quantities whose real and imaginary parts reveal the in-phase and out-of-phase components of the drive, respectively.

Our strategy to distinguish the two forces in the experiment is based on the anisotropic character to the piezoelectric tensor and the resulting behavior when the membrane orientation with respect to the crystallographic axes is changed. An intuitive understanding of this can be obtained from Figure 3.15. Here we rotate the reference frame of the geometry and plot the absolute value of $a_{eh}(\Omega_{M2})$ due to each force as a function of rotation angle. The angle is referred to the different crystal axes, again denoted by Miller

[10]The finite-element simulations were carried out by L. Midolo.

[11]All material parameters used are listed in the Supplementary Information of [4].

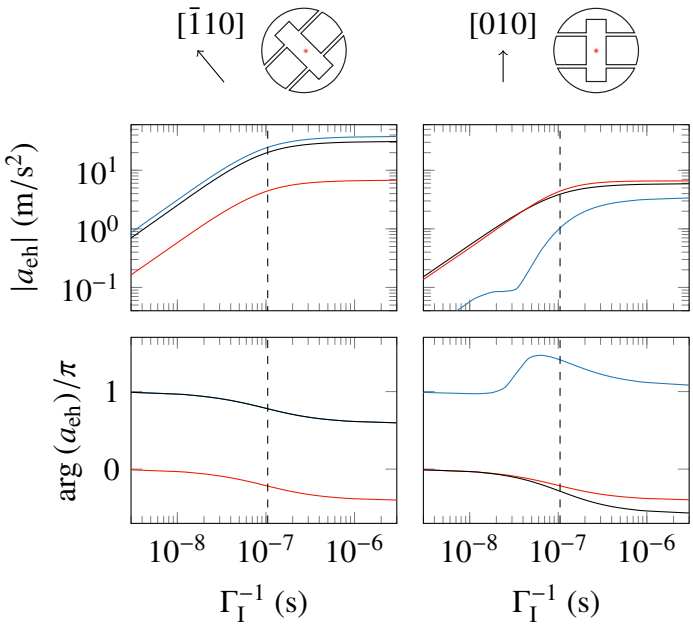

Figure 3.16: Simulated carrier-mediated forces versus lifetime in the indirect EHP state. Magnitude (top) and phase (bottom) of acceleration impressed on the symmetric bending mode M2 at a frequency of Ω_{M2} as a function of carrier lifetime Γ_I^{-1}. The red and blue lines show the behavior of the deformation potential force and the piezoelectric force, respectively, while the black solid lines are the sum of the two. Dashed lines indicate where $\Gamma_I = \Omega_{M2}$. Each column corresponds to a different membrane orientation that is sketched above the plots. Here the red shaded areas in the membrane's center depict the Gaussian excitation spots with radii $R_s = 1\,\mu m$ used in the simulation. Redrawn from [4].

indices. As can be seen, the piezoelectric force is highly dependent on the membrane orientation and maximal if the long edges of the rectangular membrane are parallel to either $[\bar{1}10]$ or $[110]$. On the other hand, the force vanishes when the membrane is rotated by $\pm 45°$, aligned to either $[010]$ or $[100]$. This is in contrast to the deformation potential force, which is smaller on average and varies less as a function of the membrane orientation. Note that in Figure 3.15, the carrier diffusion was discarded ($D = 0$) so that $n_I(x, y, \Omega_{M2})$ is a simply Gaussian distribution with variance equal to the spot radius $R_s = 1\,\mu m$. This description is valid as long as the decay dynamics of the indirect state are fast, i.e., $\Gamma_I \gg \Omega_{M2}$.

We now include the full diffusion model presented in Section 3.2.2.4 and set the input power to be $P_0 = 0.5\,\mu W$, as well as $D = 2\,cm^2\,s^{-1}$. Moreover, we focus on only two membrane orientations along $[\bar{1}10]$ and $[010]$. For each force the amplitude and the phase of $a_{eh}(\Omega_{M2})$ is shown as a function of lifetime Γ_I^{-1} in Figure 3.16. We see that all curves follow a similar trend as $n_I(x, y, \Omega_{M2})$, in particular exhibiting a large amplitude and phase shift for $\Gamma_I < \Omega_{M2}$. Other than that, two important features are immediately apparent: First, the piezoelectric force is not entirely suppressed for a membrane aligned along $[010]$. In fact, if $\Gamma_I < \Omega_{M2}$ and the carriers diffuse further away from the center, the piezoelectric force is only about a factor of two smaller than the deformation potential force. Second, the two forces have opposite signs as revealed

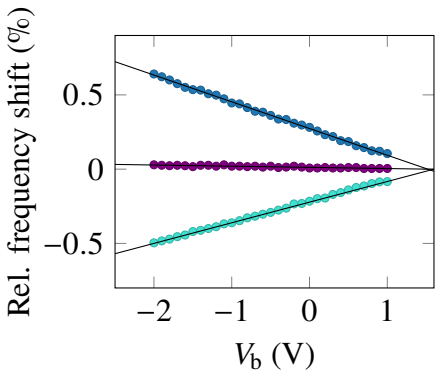

Figure 3.17: Identification of the membrane orientation. Piezoelectrically induced frequency shift of mode M1 relative to $\Omega_{M1}/2\pi$ at $V_b = 1.52\,V$ as a function of bias voltage. By evaluating the slope of linear fits (black lines), three different membranes are identified to be orientated along $[\bar{1}10]$ (blue), [010] (purple) and [110] (cyan). Redrawn from [4].

by the phase differences of π. Crucially, this phase difference is also expected when comparing the total forces between the membrane orientations, which can be directly measured using our Michelson interferometer.

3.3.2.2 Identification of the membrane orientation

In order to correctly identify the membrane orientation with respect to the crystal axes in the experiment, we use the cleavage plane of the GaAs wafer, parallel to the axis [100], as a reference. We also utilize a technique based on the static piezoelectric effect induced by the bias voltage V_b. As described in Section 3.3.1.3, the piezoelectric stress is proportional to an applied electric field and can cause a length change in the four beams that depends on the membrane orientation. Consequently, the frequency Ω_{M1} of the drum mode M1 (see Section 3.2.1.1) linearly shifts as a function of V_b. As shown in Figure 3.17, large frequency shifts with negative and positive slopes are found when the membrane is oriented along the axes $[\bar{1}10]$ and [110], respectively, while Ω_{M1} is nearly constant if the membrane is aligned along [010]. Notice that in the figure we show all frequency shifts relative to their corresponding mode frequency and set them to zero for $V_b = 1.52\,V$, where the applied field cancels the built-in electric field due to the doped GaAs layers in our device and the piezoelectric effect vanishes.

3.3.3 Driven response measurements

Having established a theoretical understanding of the carrier-mediated forces in our device, we now return to the experiment and present our main findings of this chapter. The findings are based on a series of driven response measurements, in which we determine how the membrane mode M2 responds to optical excitation with above-bandgap laser light as a function of V_b.

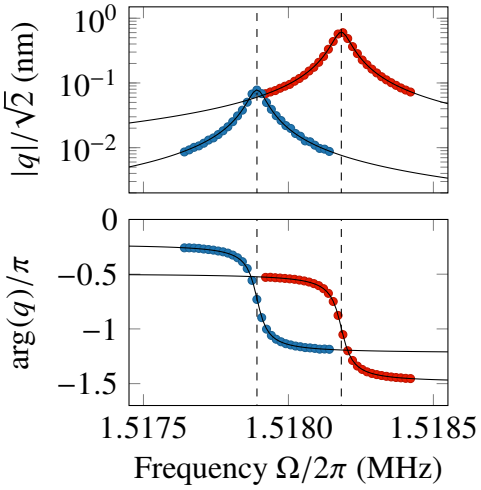

Figure 3.18: Driven response of the mechanical resonance. rms amplitude (top) and phase response (bottom) of mechanical mode M2 when optically excited with amplitude-modulated light at a wavelength of $\lambda = 880\,\text{nm}$. Blue and red dots are data for bias voltages V_b of 0 V and −1 V, respectively, and black solid lines are fits. We extract the peak amplitude and phase at resonance $\Omega = \Omega_{\text{M2}}$, as indicated by dashed lines. The membrane is oriented along the crystal axis [010]. Redrawn from [4].

3.3.3.1 Method and results

We place our device in a cryostat at a temperature of $T = 12\,\text{K}$ and continuously monitor the displacement of mode M2 using our Michelson Interferometer (see Section 1.2.1) at a wavelength of 1064 nm with the probe beam focused to the center of the membrane. A second laser beam at $\lambda = 880\,\text{nm}$ is incident at the same location with an optical power of $2P_0 = 1\,\mu\text{W}$ and generates carriers in the CQWs. We amplitude-modulate the second laser beam using an AOM so that the time-dependence of the optical power at the membrane surface is $P(t) = P_0(\text{sgn}(\sin(\Omega t)) + 1)$. The modulation frequency Ω is swept in a narrow window across the frequency $\Omega_{\text{M2}} \approx 1.5\,\text{MHz}$ while we record the signal from the interferometer with a lock-in amplifier. This way, we fully determine the mechanical response, i.e., the displacement

$$q(\Omega) = \chi_\text{m}(\Omega) F_\text{eh}(\Omega), \tag{3.14}$$

where $F_\text{eh}(\Omega)$ is the total optical force and $\chi_\text{m}(\Omega)$ is the susceptibility defined in Equation (A.14). From a fit to the data we extract the peak rms amplitude $q_0 = |q(\Omega_{\text{M2}})|/\sqrt{2}$ as well as the phase $\phi_0 = \arg(q(\Omega_{\text{M2}}))$. Examples of such a measurement are shown in Figure 3.18.

The next step is to measure q_0 and ϕ_0 for different values of the bias voltage V_b, with which we tune the carrier lifetime and consequently the magnitude and phase of the carrier-mediated forces F_eh. In doing so, it is necessary to compensate for the fact that the mechanical quality factor Q and thus $\chi_\text{m}(\Omega_{\text{M2}}) = -iQ/m_\text{eff}\Omega_{\text{M2}}^2$ varies by $\sim 10\,\%$ as a function of V_b.[12] After each sweep we perform 10 ringdown measurements to

[12]The mode frequency Ω_{M2} is constant to within 0.06 %.

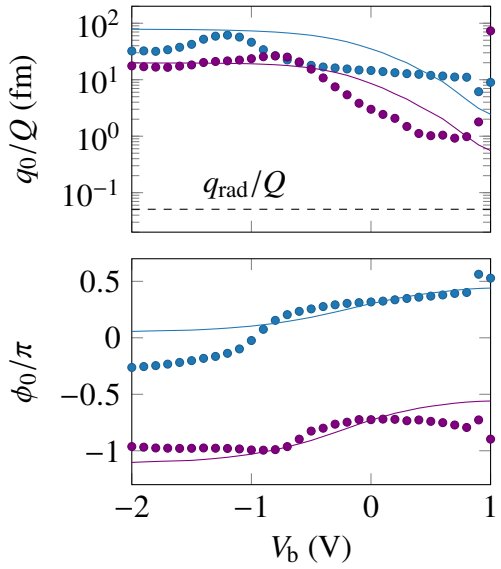

Figure 3.19: Driven response measurements versus bias voltage. Peak rms amplitude q_0 normalized by the quality factor (top) and phase ϕ_0 (bottom) of mode M2 as a function of bias voltage V_{b} measured for membranes orientated along $[\bar{1}10]$ (blue) and [010] (purple). The colored dots are data points and the solid lines are theoretical curves based on finite-element simulations. The dashed line indicates the normalized rms amplitude A_{rad}/Q expected from a radiation pressure drive of the mode. Relative errors on the data points are < 10 % and are not shown. Redrawn from [4].

determine Q and use it to normalized q_0. In Figure 3.19 we compose data from our driven response measurements acquired in the range $V_{\mathrm{b}} = -2\,\mathrm{V} \ldots +1\,\mathrm{V}$ for two different membrane orientations along the crystal axes $[\bar{1}10]$ and [010].

3.3.3.2 Discussion

The simulated total acceleration $a_{\mathrm{eh}}(\Omega_{\mathrm{M2}})$ presented in the previous section is readily compared to the data by employing the following equations for the amplitude and phase, derived directly from Equation (3.14):

$$\frac{q_0}{Q} = \frac{|\xi|}{\sqrt{2}\Omega_{\mathrm{M2}}^2}|a_{\mathrm{eh}}(\Omega_{\mathrm{M2}})|, \tag{3.15}$$

$$\phi_0 = -\pi + \arg(\xi) + \arg(a_{\mathrm{eh}}(\Omega_{\mathrm{M2}})). \tag{3.16}$$

Here the complex number ξ is a free parameter, determined via a fit to the data from the membrane oriented along the crystal axis [010], where we use the simulations of $a_{\mathrm{eh}}(\Omega_{\mathrm{M2}})$ shown in Figure 3.16 as well as the theoretical curve of the lifetime in Figure 3.8. We get $|\xi| = 0.39(7)$ and $\arg(\xi)/\pi = -0.55(2)$, and use these values to plot both theoretical curves in Figure 3.19. Fitting to only one of the two datasets is crucial since we want to distinguish the strength and sign of $a_{\mathrm{eh}}(\Omega_{\mathrm{M2}})$ in the two orientations. It lets us contrast the piezoelectric force, prevailing in the membrane aligned to the axis

[$\bar{1}$10], with the deformation potential force, dominant if the membrane is rotated by 45° and oriented along [010]. This analysis constitutes a major aspect of our work.

Our model captures the overall behavior observed in the data, loosely separated into three different regimes: For $V_\mathrm{b} \gtrsim 0\,\mathrm{V}$ the response is characterized by short lifetimes Γ_I^{-1} and low carrier densities resulting in relatively small amplitudes q_0. An abrupt change appears in the range $V_\mathrm{b} \approx -1 \ldots 0\,\mathrm{V}$, where $\Gamma_\mathrm{I} \approx \Omega_\mathrm{M2}$ and q_0 significantly increases. The phase ϕ_0 drops as explained by the delay of the motion due to the prolonged carrier lifetime. For $V_\mathrm{b} \lesssim -0.5\,\mathrm{V}$ the amplitude and phase are almost constant in the theory curves, while the data feature a small decrease of q_0 near $V_\mathrm{b} = -2\,\mathrm{V}$. Comparing the two different membrane orientations along [$\bar{1}$10] and [010], we see that q_0 of the former is larger by approximately a factor of four, meaning that the piezoelectric force is significantly stronger in our device as expected from the simulations presented in Figure 3.16. Most importantly, the predicted phase difference of π, indicating opposite signs of the two carrier-mediated forces, is found in the data.

With regard to the obvious discrepancies between data and theory, we consider several sources of systematic errors: The first concerns screening of V_b due to the electric field E_eh from the separation of electrons and holdes in the indirect state I, as has been studied before in CQWs [153, 154]. According to Equation (3.13), E_eh is proportional to the area density of EHPs n_I which we estimate in the steady-state by setting $\dot{n}_\mathrm{D} = \dot{n}_\mathrm{I} = 0$ in Equations (3.1) and (3.2). Moreover, the density is assumed to be homogenous across an area of a circle with radius R_s and yields

$$\bar{n}_\mathrm{I} = \frac{\alpha_\mathrm{D} \bar{P}}{\hbar \omega_\mathrm{l} \Gamma_\mathrm{I} \pi R_\mathrm{s}^2}. \tag{3.17}$$

Here $\bar{P} = P_0 = 0.5\,\mu\mathrm{W}$ is the average power of the modulated light, $\omega_\mathrm{l} = 2\pi c/\lambda$, and R_s is the spot radius under continuos illumination, shown in Figure 3.9. We find a maximal value of $\bar{n}_\mathrm{I} \approx 4 \times 10^9\,\mathrm{cm}^{-2}$ for $V_\mathrm{b} = -2\,\mathrm{V}$, $\Gamma_\mathrm{I}^{-1} = 750\,\mathrm{ns}$, and $R_\mathrm{s} = 16.7\,\mu\mathrm{m}$. This means that the average electric field is $\bar{E}_\mathrm{eh} = q\bar{n}_\mathrm{I}/\epsilon_0\epsilon_r \approx 56\,\mathrm{kV\,m}^{-1}$, nearly two orders of magitude smaller than the field provided by the applied voltage $V_\mathrm{b} = -2\,\mathrm{V}$. We are lead to conclude that screening due to optically generated EHPs is negligible and does not explain the mismatches in Figure 3.19.

Another problem could be that photothermal forces, proportional to the expansion coefficient β (see Section 3.3.1.2), are not accounted for in our model. The assumption that β vanishes in our device for $T = 12\,\mathrm{K}$ may not be fully justified when considering the small differences in β for the various III-V compounds used in the heterostructure. On top of that, the temperature could be marginally different from 12 K. Now, if for any of these reasons photothermal forces play a role in the driven response measurements we expect to see a significant temperature dependence of the normalized amplitude q_0/Q, similar to that measured in β. However, this is not the case as shown in Figure 3.20, where we set $V_\mathrm{b} = -1.5\,\mathrm{V}$ and plot q_0/Q versus T. Indeed, the amplitude is rather constant in the range from 10 K to $\sim$ 70 K, where two zero-crossings of β occur in GaAs and consequently we observe maximal quality factors Q as discussed in Section 3.2.1.2. For $T \gtrsim 70\,\mathrm{K}$ we see a drop of q_0/Q likely due to thermal escape of carriers out of

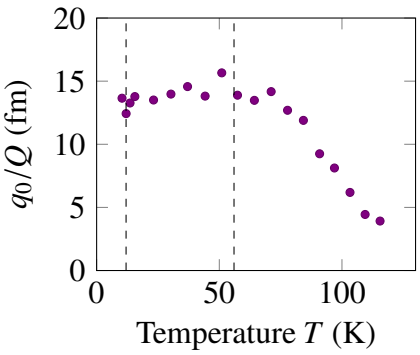

Figure 3.20: Driven response measurement versus temperature. Peak rms amplitude q_0 normalized by the quality factor as a function of temperature T for a membrane orientation of [010] and $V_\mathrm{b} = -1.5\,\mathrm{V}$. Dashed lines at 12 K and 56 K indicated zero crossings of the thermal expansion coefficient β of GaAs.

the CQWs [155]. The data shown in Figure 3.20 confirms that photothermal forces are insignificant in our device.

Lastly, we suspect that our description of the EHP generation and recombination in the CQWs is oversimplified. In particular, the three-level scheme in Section 3.2.2.3 could be inaccurate since higher-order EHP states, such as those formed by the wavefunctions e3 and h3, might be occupied and may influence the carrier dynamics. Another plausible source of error in our model is non-radiative surface recombination of carriers at the membrane's edges. The diffusion measurements in Section 3.2.2.4 evidence that the EHPs indeed reach the edges, if the excitation beam is placed in the center of the membrane. Since surface recombination effectively decreases the lifetime Γ_I, especially for large negative bias voltages, it could explain the reduced amplitude seen in the data for $V_\mathrm{b} \lesssim -1.5\,\mathrm{V}$. Outliers near $V_\mathrm{b} = 1\,\mathrm{V}$ are likely due to diode forward current, introducing additional charges in the CQWs.

Remarkably, the carrier-mediated forces studied here are much stronger than radiation pressure. For the latter we estimate the rms displacement q_rad using Equation (1.10), where the amplitude of the incident power is $P_0 = 0.5\,\mu\mathrm{W}$, the membrane reflectivity is $|r_\mathrm{m}|^2 \approx 66\,\%$, $\lambda = 880\,\mathrm{nm}$, and $m_\mathrm{eff} = 340\,\mathrm{pg}$. This yields $q_\mathrm{rad}/Q \approx 0.051\,\mathrm{fm}$, which is more than three orders of magnitude smaller than the maximum value measured in the experiment, namely $\max(q_0/Q) = 61.6(3)\,\mathrm{fm}$ at $V_\mathrm{b} = -1.2\,\mathrm{V}$ (see Figure 3.19), corresponding to the case where the membrane is predominantly driven by the piezoelectric force. It should be noted that the membrane heterostructure could be optimized to make for even larger displacements, for example, by decreasing the thickness and placing the CQWs further away from the center to promote greater bending forces.

3.4 Use in optomechanics

Let us now discuss the prospects of utilizing the carrier-induced forces in a cavity optomechanical system. The idea is that the retardation necessary to realize dynamical backaction is given by the carrier lifetime instead of the photon lifetime in the cavity; the

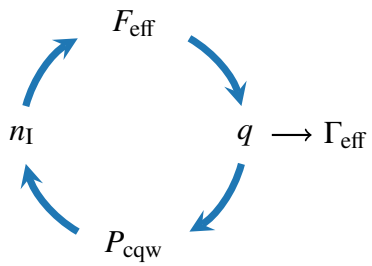

Figure 3.21: Schematic of the optomechanical coupling mechanism. We consider four interrelated quantities in our system: the displacement q of the mechanical mode M2, the optical power P_{cqw} at the CQWs, the carrier density n_{I} in the indirect state I, and the total carrier-induced force F_{eh}. The optical damping due to dynamical backaction is described by the effective damping rate Γ_{eff}.

latter is the case if the coupling is mediated by radiation pressure. This novel approach can in principle be implemented using the integrated Fabry-Pérot cavity in our device (see Section 3.2.3) as will be detailed in the following.

3.4.1 Coupling via the integrated cavity

Figure 3.21 shows a schematic diagram of the mechanism for the optomechanical coupling, where we assume that the cavity is driven by above-bandgap laser light with a constant input power P_0. A small displacement q of the membrane due to thermal motion results in a change in the intra-cavity optical power and, accordingly, the power P_{cqw} at the CQWs. As the laser light generates EHPs, the change in power translates into the density of carriers occupying the indirect state n_{I}. As discussed before, this process is subject to a delay given by the finite carrier lifetime Γ_{I}^{-1}. We now get a change in the total force $F_{\mathrm{eh}} \propto n_{\mathrm{I}}$ which drives the membrane motion and again results in a displacement q. This feedback mechanism gives rise to optical damping and an effective mode temperature $T_{\mathrm{eff}} = T\Gamma_{\mathrm{m}}/\Gamma_{\mathrm{eff}}$ (see Appendix A.3.2). The effective damping rate reads [138, 156]

$$\Gamma_{\mathrm{eff}} = \Gamma_{\mathrm{m}} + \frac{\Gamma_{\mathrm{I}}^{-1}}{1 + \Omega_{\mathrm{M2}}^2 \Gamma_{\mathrm{I}}^{-2}} \frac{\nabla F_{\mathrm{eh}}}{m_{\mathrm{eff}}}, \tag{3.18}$$

where $\Gamma_{\mathrm{m}} = \Omega_{\mathrm{M2}}/Q \approx 2\pi \times 59\,\mathrm{Hz}$ is the mechanical damping rate of mode M2. ∇F_{eh} is the photo-induced rigidity, i.e., the gradient of F_{eh} with respect to q or equivalently the cavity length L. It may be written as follows:[13]

$$\nabla F_{\mathrm{eh}} = -|\xi| m_{\mathrm{eff}} \frac{d|a_{\mathrm{eh}}|}{dP_{\mathrm{cqw}}} \frac{dP_{\mathrm{cqw}}}{dL}. \tag{3.19}$$

Here we need take into account the correction factor $|\xi| \approx 0.39$ which we have extracted from the driven response measurements in Section 3.3.3.2.

To estimate the optical damping in our system, we first employ the TMM (see Appendix A.4) to model the electric fields propagating in the cavity and calculate P_{cqw}

[13]The negative sign in Equation (3.19) is due to the definition of a_{eh} in our simulation.

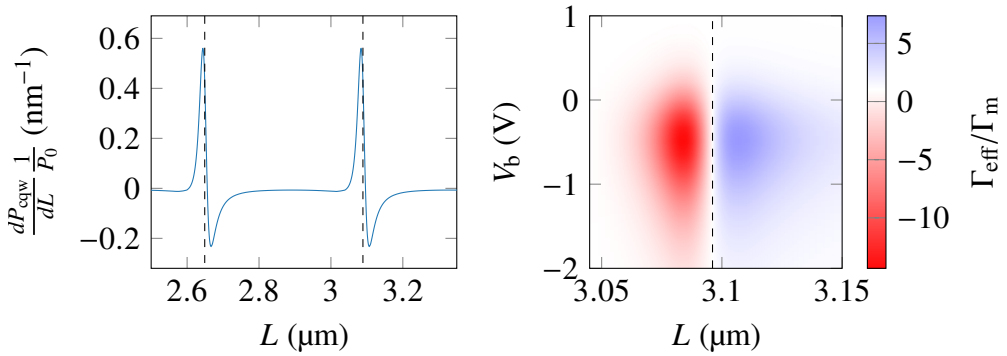

Figure 3.22: Calculation of optical cooling and amplification with the integrated cavity. Left: Derivative of the optical power P_{cqw} at the CQWs with respect to the cavity length L normalized by the input power P_0. The dashed lines indicate where the detuning from the cavity is zero at a wavelength of $\lambda = 880\,\text{nm}$. Right: Cooling factor Γ_{eff}/Γ_m as a function of L and bias voltage V_b for a membrane oriented along [010]. The dashed line is a contour at $\Gamma_{eff}/\Gamma_m = 1$.

normalized to P_0 assuming $\lambda = 880\,\text{nm}$ and $T = 12\,\text{K}$. The derivate reveals dP_{cqw}/dLP_0 exhibiting positive and negative values on either side of the cavity resonance, as shown in Figure 3.22. Next, we use the force simulations (see Figure 3.16) to calculate $d|a_{eh}|/dP_{cqw}$, where $d|a_{eh}|$ is the magnitude of the acceleration and $dP_{cqw} = 0.5\,\mu\text{W}$ is the amplitude to the modulated optical drive. Combining Equations (3.18) and (3.19) we then determine the cooling rate Γ_{eff}/Γ_m for a membrane oriented along the crystal axis [010], and plot it as a function of V_b and L on the right hand side of Figure 3.22. We assume an input power of $P_0 = 50\,\mu\text{W}$ and find that both cooling ($\Gamma_{eff}/\Gamma_m > 1$) and amplification ($\Gamma_{eff}/\Gamma_m < 1$) are expected. To get maximum cooling, the parameters need to be adjusted to $V_b \approx -0.5\,\text{V}$ and $L \approx 3.084\,\mu\text{m}$, resulting in a reduction of the temperature by a factor of $T/T_{eff} = \Gamma_{eff}/\Gamma_m \approx 7.4$. On the other hand, an instability due to the amplification occurs if $\Gamma_{eff}/\Gamma_m < 0$, giving rise to self-oscillations.

To see these effects in our experiment, we probe the displacement of mode M2 with the interferometer while driving the cavity resonance in the center of the membrane with laser light at a wavelength of 880 nm and a constant input power P_0. For a few devices and at relatively large values of $P_0 \gtrsim 100\,\mu\text{W}$ we observe amplification and self-oscillations of the mode showing a dependence on the bias voltage, yet no optical cooling or broadening of the linewidth can be seen. It is not clear why this is the case. We suspect that addressing the correct cavity detuning for the cooling by selecting a membrane with a specific buckling is too inaccurate (see Section 3.2.3.2). Indeed, we could only find three out of 26 devices with different beam lengths in which the cavity resonance was found near the center of the membrane. Tuning the laser frequency to fine-adjust the detuning is ineffective because of the $\sim 10\,\text{THz}$ cavity linewidth.

3.4.2 Other implementations

It is possible to enable better control over the detuning by implementing a MiM system (see Section 2.2.1). In that case the free-free nanomembrane no longer serves as an end-

mirror, but instead as a dielectric film inside the optical cavity formed by the DBR and a curved, high-reflective mirror that is placed above the membrane. Such an arrangement could have a significantly larger cavity length and thus a reduced linewidth, allowing us to precisely target any detuning by simply adjusting the laser frequency in a more accessible range. A challenge regarding this implementation concerns the required spot size of the cavity mode. In order to avoid scattering of the light at the edges of the membrane, the spot should not be larger than a few µm. Using the relatively large mirrors[14] normally employed in our lab, whose radii of curvature are $R_c \gtrsim 8\,\mathrm{mm}$, such a small spot size aligned to a specific position of the membrane is technically difficult to realize. An easier solution is to incorporate a curved miniaturized mirror [157] or a mirror fiber tip [158] each with typical values of $R_c = 10\,\mu\mathrm{m}...100\,\mu\mathrm{m}$. We have attempted to realize the latter in collaboration with the Quantum photonics group at ETH. Due to time-constraints on this project we could not complete the fiber cavity setup and can therefore not report on any relevant findings at this point. Resuming the project in the future could reveal interesting insights about the usage of carrier-mediated forces in a MiM configuration.

Apart from the Fabry-Pérot cavities discussed so far, we envision another system that could benefit from the carrier-mediated forces, namely GaAs-based disk resonators [159], in which light travels in whispering-gallery modes and couples to mechanical breathing modes via photoelastic coupling [160]. Typically driven at telecom-wavelengths ($\lambda = 1.3\,\mu\mathrm{m}$) where the optical absorption is low, these resonators have remarkably large single-photon coupling rates of $g_0/2\pi \sim 1\,\mathrm{MHz}$ and higher, mediated by radiation pressure and electrostriction. A possible route to enhance the interaction even further could be to embed quantum wells or quantum dots in the disc, generate carriers with above-bandgap laser light and drive the breathing modes via the deformation potential. Due to the $\Omega_m/2\pi \sim 1\mathrm{GHz}$ frequencies, the carrier lifetime does not have to be prolonged to several 100 ns, as is demonstrated in our work, but could be in the range of $1...10\,\mathrm{ns}$ to match the period $1/\Omega_m$. Now, it should be noted that a drawback in the suggested approach would be the absorption of light reducing the finesse of the cavity. In fact, this is true for any system implementing our method.

In general, GaAs-based optomechanical resonators are interesting platforms because of the many possibilities to realize novel electro-optomechanical hybrid systems. Examples are nanowires coupled to quantum dots [161], beams coupled to superconducting circuits [162], and optomechanical crystal cavities acting as transducers between radio-frequency signals and light [163]. We hope that our work will stimulate even more research involving, for instance, polaritons [164–166] or active cavities of semiconductor lasers [167, 168].

[14] The mirrors have diameters and heights of a few mm.

3.5 Conclusion

In summary, we have used GaAs nanomembranes with CQWs to study forces induced by optically generated charge carriers. The forces are due to the deformation potential and the piezoelectric effect, controlled by means of a bias voltage across the CQWs that alters the carrier lifetime. In comparison to radiation pressure the carrier-mediated forces are measured to be about three orders of magnitude larger and could be used in cavity optomechanical systems to enhance the interaction. Our work opens up a new route for electro-optomechanical hybrid systems, exploiting the rich physics of quantum-confined semiconductor structures.

Appendix A

Theoretical framework

A.1 Spectral analysis

In the following section, we briefly introduce the means of analyzing the frequency content of a time signal. For a more thorough description than presented here the reader is referred to [169]. To begin with, we define an important mathematical tool, the Fourier transform $\mathcal{F}$, as follows:

$$\mathcal{F}[x(t)] \coloneqq \int_{-\infty}^{\infty} x(t)e^{-i\Omega t}dt. \tag{A.1}$$

Here $x(t)$ is a time signal and $x(\Omega) \coloneqq \mathcal{F}[x(t)]$ denotes the complex distribution of its frequency components.

Let us assume that $x(t)$ is a single realization of a random process with constant statistical properties over time (stationary), as is often the case in our work. An important identity is the Wiener-Khinchin theorem, showing that the (real) spectrum, or more precisely the double-sided power spectral density (PSD) $S_{xx}(\Omega)$ of $x(t)$, is equal to the Fourier transform of the autocorrelation function:

$$S_{xx}(\Omega) \coloneqq \mathcal{F}[\langle x^*(t)x(t+t')\rangle]. \tag{A.2}$$

If $x(t)$ is real, it follows that $S_{xx}(\Omega) = S_{xx}(-\Omega)$ and a single-sided PSD $S_x(\Omega)$ can be used, which is a factor of two larger and zero for $\Omega < 0$. From Equation (A.2), we also find that $x(\Omega)$ and $x^*(-\Omega) \coloneqq \mathcal{F}[x(t)]^*$ can be used to find the PSD:

$$S_{xx}(\Omega) = \int_{-\infty}^{\infty} \langle x^*(-\Omega)x(\Omega')\rangle d\Omega'. \tag{A.3}$$

In the quantum description we have the same definitions as mentioned above, but we substitute the signal with an operator $x(t) \to \hat{x}(t)$ and $x(\Omega) \to \hat{x}(\Omega)$. Furthermore, the ensemble averages in Equation (A.2) and Equation (A.3) are replaced by the expectation

value. Notice that the quantum PSD for an hermitian operator is not necessarily symmetric since in this case calculating $S_{xx}(-\Omega)$ involves the potentially complex commutator $[\hat{x}(t), \hat{x}(t+t')] \neq 0$ in Equation (A.2). We will come back to this feature in Appendix A.2.3, where we also refer to the classical part of the spectrum using the symmetrized PSD

$$\bar{S}_{xx} \coloneqq \frac{S_{xx}(\Omega) + S_{xx}(-\Omega)}{2}. \tag{A.4}$$

In the experiment, time signals are typically acquired digitally with a sampling rate f_s and a number of samples N_s. The PSD is then estimated via the periodogram, i.e., the absolute square of the Fast Fourier Transform normalized by $f_\mathrm{s}N_\mathrm{s}$ [170], revealing the power within each frequency bin up to the Nyquist frequency $f_\mathrm{s}/2$. The interval between two frequency bins is the resolution bandwidth

$$\mathrm{RBW} = \frac{1}{f_\mathrm{s}N_\mathrm{s}} = \frac{1}{T}, \tag{A.5}$$

where T is the length of the signal in units of time. We often acquire many periodograms and average them together to reduce the variance on the spectral estimate.

A.2 Mechanical resonators

We now summarize the theory of nanomechanical resonators relevant for our discussions above. Appendices A.2.1 and A.2.2 deal with classical models of membrane motion and thermally excited harmonic oscillators, respectively, detailed in [24, 38]. In Appendix A.2.3, we introduce the quantum description, closely following [11].

A.2.1 Out-of-plane membrane modes

The out-of-plane motion of a thin membrane is readily described by the theory of elasticity [171]. As an example, we examine the case of a square SiN membrane under uniform tensile stress σ with side length l and thickness $h \ll l$, as illustrated in Figure A.1. We start with the two-dimensional wave equation [172]

$$\frac{D}{h}\nabla^4 w(x,y,t) - \sigma\nabla^2 w(x,y,t) = -\rho\frac{\partial^2}{\partial t^2}w(x,y,t), \tag{A.6}$$

where $w(x, y, t)$ is the displacement at a given point (x, y) on the membrane evolving in time t. Furthermore, ρ is the material density and D the flexural rigidity:

$$D = \frac{Eh^3}{12(1-\nu^2)}, \tag{A.7}$$

where E is Young's modulus and ν is Poission's ratio. The wave equation is solved by separation of variables under the boundary conditions that $w(x, y, t)$ and its derivatives

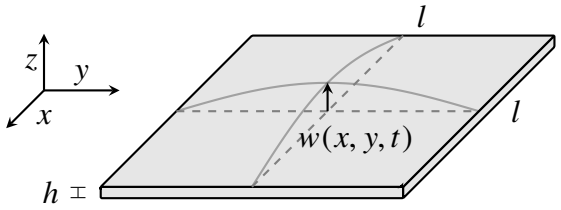

Figure A.1: Illustration of a square SiN membrane. The out-of-plane motion of a membrane with thickness h and side length l, fixed to the frame is described by the displacement $w(x, y, t)$.

with respect to x and y vanish at the membrane edges. The solutions are approximated by sinusoidal transverse mode shapes of the form:

$$w(x, y, t) \approx q(t) \sin(nkx) \sin(mky), \tag{A.8}$$

where $k = \pi/l$ and the integers n and m denote the number of antinodes along the x and y direction, respectively. A small exponential correction near the edges has been neglected, which is due to the first term on the left hand side of Equation (A.6) referring to the bending of the membrane. This approximation is valid when identifying the modes of highly-stressed SiN membranes, as is done in Section 1.2. However, when calculating internal dissipation of such membranes the correction contributes the majority of bending loss and needs to be included (see Section 1.4.2).

The membrane displacement follows one-dimensional harmonic motion, at an antinode of a mode we can write $q(t) = q_0 \cos(\Omega_m t + \phi)$, where q_0 is the amplitude and ϕ a phase that depends on the initial condition. The mechanical angular frequency Ω_m is given by the following relation:

$$\Omega_m^2 = \frac{\pi^2 \sigma}{\rho l^2} \left(n^2 + m^2\right). \tag{A.9}$$

For the harmonic motion $q(t)$ we can find an effective mass by spatially integrating the square of the mode shape [38]:

$$m_{\text{eff}} = \rho h \int_0^l \int_0^l \sin^2(nkx) \sin^2(mky)\, dx\, dy = \frac{m_0}{4}, \tag{A.10}$$

where $m_0 = \rho l^2 h$ is the physical mass of the membrane. Notice that the effective mass is independent of the mode (n, m), which is unique for square and rectangular membranes.

A.2.2 Thermally excited harmonic motion

A mechanical resonator, such as the membrane discussed above, coupled to a thermal environment is subject to a fluctuating force $F_{\text{th}}(t)$. This force excites the one-dimensional displacement $q(t)$ as described for a single mode by the equation of motion for a damped harmonic oscillator:

$$\ddot{q}(t) + \Gamma_m \dot{q}(t) + \Omega_m^2 q(t) = \frac{F_{\text{th}}(t)}{m_{\text{eff}}}. \tag{A.11}$$

Here the inverse of the damping rate Γ_m^{-1} is the time constant characterizing the exponential decay of the amplitude, also referred to as the ringdown time. The number of oscillations before the amplitude decays to $1/e$ of its initial value is the quality factor

$$Q = \frac{\Omega_\mathrm{m}}{\Gamma_\mathrm{m}}, \tag{A.12}$$

valid for the case of underdamped motion, i.e., $\Gamma_\mathrm{m} \ll \Omega_\mathrm{m}$. The damping relates to the fluctuating force $F_\mathrm{th}(t)$ via the fluctuation dissipation theorem [173]. Indeed, the PSD of the force reads

$$S_{FF}^\mathrm{th}(\Omega) = 2\Gamma_\mathrm{m} m_\mathrm{eff} k_\mathrm{B} T, \tag{A.13}$$

where k_B is the Boltzmann constant and T is the temperature of the environment. Notice that this is independent of Ω (white noise). We can solve Equation (A.11) in the Fourier domain, where the time derivative $d/dt \to i\Omega$, and get the algebraic expression $q(\Omega) = \chi_\mathrm{m}(\Omega) F_\mathrm{th}(\Omega)$ in which the mechanical susceptibility is defined as follows:

$$\chi_\mathrm{m}(\Omega)^{-1} = m_\mathrm{eff}\left(\Omega_\mathrm{m}^2 - \Omega^2 + i\Omega\Gamma_\mathrm{m}\right) \tag{A.14}$$

$$\approx 2m_\mathrm{eff}\Omega_\mathrm{m}\left(\Omega_\mathrm{m} - \Omega + i\frac{\Gamma_\mathrm{m}}{2}\right). \tag{A.15}$$

In the last line, we approximate the susceptibility close to the resonance frequency $|\Omega_\mathrm{m} - \Omega| \ll \Omega_\mathrm{m}$ revealing that its absolute square $|\chi_\mathrm{m}(\Omega)|^2$ is a Lorentzian function with a peak at $\Omega = \Omega_\mathrm{m}$ and a FWHM of Γ_m. The PSD is now found via Equation (A.3):

$$S_{qq}(\Omega) = |\chi_\mathrm{m}(\,\Omega)|^2 S_{FF}^\mathrm{th}(\Omega). \tag{A.16}$$

Finally, we can integrate the PSD and thereby reveal the variance of the mode displacement to be the following:

$$\langle q^2 \rangle = \int_{-\infty}^{\infty} S_{qq}(\Omega)\,\frac{d\Omega}{2\pi} = \frac{k_\mathrm{B} T}{m_\mathrm{eff}\Omega_\mathrm{m}^2}. \tag{A.17}$$

Evidently, this result is in agreement with the equipartition theorem stating that the resonator's average energy, i.e., twice the average potential energy, is equal to $k_\mathrm{B}T$.

A.2.3 Quantum description

The quantum description of a single mode of a mechanical resonator is characterized by discrete energy levels, equidistantly separated by the energy $\hbar\Omega_\mathrm{m}$. This is found by solving the Schrödinger equation with the Hamiltonian

$$\hat{H} = \hbar\Omega_\mathrm{m}\left(\hat{b}^\dagger\hat{b} + \frac{1}{2}\right), \tag{A.18}$$

where $\hat{n} = \hat{b}^\dagger \hat{b}$ is the number operator. $\hat{b}$ and $\hat{b}^\dagger$ are the annihilation and the creation operator, respectively, which are related to the position operator $\hat{q}$ and the momentum operator $\hat{p}$ in the following way:

$$\hat{q} = q_{\mathrm{zp}} \left(\hat{b}^\dagger + \hat{b} \right), \tag{A.19}$$

$$\hat{p} = i p_{\mathrm{zp}} \left(\hat{b}^\dagger - \hat{b} \right), \tag{A.20}$$

Here q_{zp} and $p_{\mathrm{zp}} = \hbar / 2 q_{\mathrm{zp}}$ describe the zero-point motion due to the finite energy of the ground state with $\langle \hat{n} \rangle = 0$, and the rms displacement yields

$$q_{\mathrm{zp}} \coloneqq \sqrt{\langle \hat{q}^2 \rangle - \langle \hat{q} \rangle^2} = \sqrt{\frac{\hbar}{2 m_{\mathrm{eff}} \Omega_{\mathrm{m}}}}. \tag{A.21}$$

When coupled to thermal phonons from the environment at a temperature T, the harmonic oscillator must be written as a mixed state which, in equilibrium, is governed by Bose-Einstein statistics. The mean occupancy of this state is given by

$$\bar{n}_{\mathrm{th}} \coloneqq \langle \hat{n} \rangle = \left(e^{\frac{\hbar \Omega_{\mathrm{m}}}{k_{\mathrm{B}} T}} - 1 \right)^{-1} \tag{A.22}$$

$$\approx \frac{k_{\mathrm{B}} T}{\hbar \Omega_{\mathrm{m}}}. \tag{A.23}$$

For the parameters used in our experiments $T > 4.2\,\mathrm{K}$ and $\Omega_{\mathrm{m}}/2\pi \approx 1\,\mathrm{MHz}$ it is reasonable to assume the high temperature classical limit $k_{\mathrm{B}} T \gg \hbar \Omega_{\mathrm{m}}$ and use the approximation in Equation (A.23).

If we prepare our mechanical resonator in a pure state, such as the ground state, it will be out of equilibrium. The mean occupancy as a function of time then follows the equation [11]:

$$\dot{\bar{n}}(t) = \Gamma_{\mathrm{m}} \bar{n}_{\mathrm{th}} - \Gamma_{\mathrm{m}} \bar{n}(t). \tag{A.24}$$

With the occupancy of the mechanical resonator initially given by $\bar{n}(0) = 0$, we find the solution of Equation (A.24) to be

$$\bar{n}(t) = \bar{n}_{\mathrm{th}} \left(1 - e^{-\Gamma_{\mathrm{m}} t} \right), \tag{A.25}$$

converging towards the steady-state solution $\bar{n}_{\mathrm{th}}$ as shown in Figure A.2. From Equation (A.25) we evaluate the time for an average of one quanta from the thermal environment to enter our resonator, i.e., the thermal coherence time

$$\tau = -\frac{\ln\left(1 - \frac{1}{\bar{n}_{\mathrm{th}}}\right)}{\Gamma_{\mathrm{m}}} \approx \frac{1}{\Gamma_{\mathrm{m}} \bar{n}_{\mathrm{th}}}, \tag{A.26}$$

where we again assume the high temperature limit $\bar{n}_{\mathrm{th}} \gg 1$ in the last identity. Notice that this approach to quantify the coherence is only valid for the ground state. For

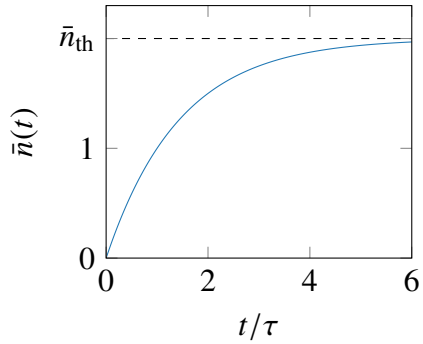

Figure A.2: Time evolution of the mean occupancy. The harmonic oscillator, initially in the ground state, converges to the thermal equilibrium with the decoherence rate $1/\tau$. Here we set $\bar{n}_{\mathrm{th}} = 2$.

a mechanical Fock state with a phonon number n, the decoherence rate τ_n^{-1} must be calculated as the sum of upwards and downwards going transition rates, as detailed in [11], and thus yields the following:

$$\tau_n^{-1} = \Gamma_{\mathrm{m}} \left(\bar{n}_{\mathrm{th}}(n+1) + (\bar{n}_{\mathrm{th}}+1)n\right). \tag{A.27}$$

This means that the coherence time decreases with n as $\tau/\tau_n \approx 2n+1$ for $\bar{n}_{\mathrm{th}} \gg 1$.

In complete analogy to the classical description in Appendix A.2.2, we now evaluate the thermally excited displacement starting with the equation of motion

$$\ddot{\hat{q}}(t) + \Gamma_{\mathrm{m}}\dot{\hat{q}}(t) + \Omega_{\mathrm{m}}^2\hat{q}(t) = \frac{\hat{F}_{\mathrm{th}}(t)}{m_{\mathrm{eff}}}. \tag{A.28}$$

Here the operator $\hat{F}_{\mathrm{th}}(t)$ denotes the random force exerted onto the oscillator due to the thermal bath. The quantum version of the fluctuation-dissipation theorem is given by [11]

$$S_{FF}^{\mathrm{th}}(\Omega_{\mathrm{m}}) = 2\Gamma_{\mathrm{m}} m_{\mathrm{eff}} \hbar \Omega_{\mathrm{m}} (\bar{n}_{\mathrm{th}} + 1), \tag{A.29}$$

$$S_{FF}^{\mathrm{th}}(-\Omega_{\mathrm{m}}) = 2\Gamma_{\mathrm{m}} m_{\mathrm{eff}} \hbar \Omega_{\mathrm{m}} \bar{n}_{\mathrm{th}}. \tag{A.30}$$

A striking difference between these expressions and the classical fluctuation dissipation theorem in Equation (A.13) is the fact that $S_{FF}^{\mathrm{th}}(\Omega_{\mathrm{m}}) \neq S_{FF}^{\mathrm{th}}(-\Omega_{\mathrm{m}})$, carrying further onto the spectrum of the displacement. The latter is extracted by solving Equation (A.28) and assuming the force PSD to be constant across the bandwidth of the mechanical mode. Then, we use the approximate susceptibility in Equation (A.15) and get [52]

$$S_{qq}(\Omega) = q_{\mathrm{zp}}^2 \Gamma_{\mathrm{m}} \left(\frac{\bar{n}_{\mathrm{th}}}{(\Omega_{\mathrm{m}} - \Omega)^2 + \Gamma_{\mathrm{m}}^2/4} + \frac{\bar{n}_{\mathrm{th}} + 1}{(\Omega_{\mathrm{m}} + \Omega)^2 + \Gamma_{\mathrm{m}}^2/4} \right). \tag{A.31}$$

Notice that both the fluctuation dissipation theorem and the mechanical spectrum are reduced to their classical counterparts in Equation (A.13) and Equation (A.16), respectively, by using the approximation of $\bar{n}_{\mathrm{th}}$ in Equation (A.23) and the symmetrized PSD

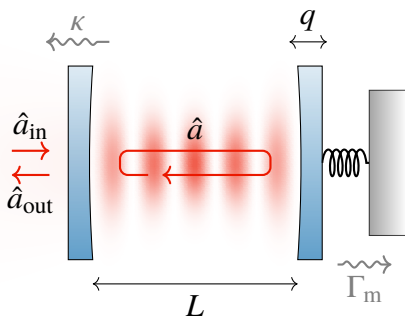

Figure A.3: Illustration of a canonical optomechanical system. A single mode of a light field $\hat{a}$ inside a FP cavity of length L couples parametrically to the motion of a mirror described by $q = \langle q_{\mathrm{zp}}(\hat{b}^\dagger + \hat{b})\rangle$. Optical and mechanical losses are denoted κ and Γ_{m}, respectively.

defined in Equation (A.4). On the other hand, for low occupancies $S_{qq}(\Omega)$ behaves very differently compared to the classical case; it constitutes a large asymmetry between the two Lorentzian peaks at $\pm\Omega_{\mathrm{m}}$. In Section 2.3, this feature is exploited to determine the phonon occupancy, a method known as Raman sideband thermometry.

A.3 Optomechanical dynamics

We will now turn our attention to the basic theory of cavity optomechanics which has been developed thoroughly in the literature. We refer the reader to [11] for a particularly comprehensive review and also follow this reference in our remarks. After introducing the dynamic equations of motion in Appendix A.3.1, we describe the most relevant effects for the topic of this thesis, namely dynamical backaction in Appendix A.3.2 and the standard quantum limit in Appendix A.3.3.

A.3.1 Equations of motion

Consider a Fabry-Pérot cavity with a movable mirror as illustrated in Figure A.3. Mechanical displacement q of the mirror changes the cavity length L and thus the resonance frequency $\omega_{\mathrm{c}} = n\pi c/L$, where n is an integer denoting the longitudinal mode number and c is the speed of light. For small displacements $q \ll L$ this parametric coupling is expressed in the last term of the following Hamiltonian:

$$\hat{H} = \hbar\omega_{\mathrm{c}}\hat{a}^\dagger\hat{a} + \hbar\Omega_{\mathrm{m}}\hat{b}^\dagger\hat{b} + \hbar g_0\hat{a}^\dagger\hat{a}\left(\hat{b}^\dagger + \hat{b}\right), \tag{A.32}$$

where $\hat{a}$ and $\hat{a}^\dagger$ are the annihilation and creation operators of the intra-cavity field, respectively. Furthermore, we introduce the single-photon coupling rate

$$g_0 = q_{\mathrm{zp}}\frac{d\omega_{\mathrm{c}}}{dq}, \tag{A.33}$$

which yields $g_0 = q_{\mathrm{zp}}\omega_{\mathrm{c}}/L$ for this canonical optomechanical system. Notice that in Equation (A.32) both the (single) cavity mode and the mechanical mode are described

as quantum harmonic oscillators, for which we neglected the respective constant ground state energy terms $\hbar\omega_c/2$ and $\hbar\Omega_m/2$, since these will not contribute to the dynamics of the system discussed here. The same is true for a driving term proportional to $\hat{a}^\dagger + \hat{a}$ that is often introduced at this point, but cancels out when assuming a constant coherent drive and linearizing the equations of motion, as is shown below.

The next step is to consider the coupling of the system to a thermal environment. In Appendix A.2.2 this has already been done for the mechanical resonator by introducing the disspation rate Γ_m. On the other hand, we will denote the rate at which the cavity field leaks through one mirror with $\sqrt{\kappa}$, establishing a connection with the drive field $\hat{a}_{in}$. With this, we are in a position to formulate the quantum Markovian Langevin equations [11] which are of the form

$$\dot{\hat{O}} = \frac{1}{i\hbar}[\hat{O}, \hat{H}] + \hat{\xi}, \tag{A.34}$$

where $\hat{O}$ is an operator and $\hat{\xi}$ is the corresponding noise operator. This yields the dynamics of the cavity field $\hat{a}$ as well as the position $\hat{q}$ and momentum $\hat{p}$ of the mechanical resonator:

$$\dot{\hat{a}} = -\frac{\kappa}{2}\hat{a} + i\left(\Delta - \frac{g_0}{q_{zp}}\hat{q}\right)\hat{a} + \sqrt{\kappa}\hat{a}_{in}, \tag{A.35}$$

$$\dot{\hat{q}} = \frac{\hat{p}}{m_{eff}}, \tag{A.36}$$

$$\dot{\hat{p}} = -m_{eff}\Omega_m^2\hat{q} - \Gamma_m\hat{p} + \hat{F}_{th} - \frac{\hbar g_0}{q_{zp}}\hat{a}^\dagger\hat{a}. \tag{A.37}$$

Here we transform $\hat{a}$ into a rotating frame, defining the detuning between laser frequency ω_l and cavity resonance $\Delta := \omega_l - \omega_c$. Counter-rotating terms including $\hat{a}\hat{a}$ or $\hat{a}^\dagger\hat{a}^\dagger$ are neglected (rotating wave approximation). As can be seen, the equations are linked via the optomechanical coupling rate g_0, and setting $g_0 = 0$ recovers Equation (A.28) describing only the evolution of the mechanical resonator. In this general form, the Langevin equations are difficult to solve due to the quadratic terms and it is common to linearize them via the transformations

$$\hat{a} \to \alpha + \delta\hat{a}, \tag{A.38}$$

$$\hat{a}_{in} \to \alpha_{in} + \delta\hat{a}_{in}, \tag{A.39}$$

where α and α_{in} refer to the amplitudes and $\delta\hat{a}$ and $\delta\hat{a}_{in}$ are small fluctuations of the strong coherent cavity field and the drive field, respectively. Without loss of generality, we set α to be real. The interaction term of the Hamiltonian in Equation (A.32) now simplifies to

$$\hat{H}_{int} = \hbar g\left(\delta\hat{a}^\dagger + \delta\hat{a}\right)\left(\hat{b}^\dagger + \hat{b}\right), \tag{A.40}$$

where $g := g_0\alpha$ is the cavity-enhanced coupling rate. Notice that we omit a constant term proportional to α^2 describing a static force, as well as the second order term

including $\delta\hat{a}^\dagger\delta\hat{a}$. Furthermore, let us introduce the amplitude and phase quadrature fluctuations of the intra-cavity field, which are

$$\delta\hat{X} = \frac{\delta\hat{a}^\dagger + \delta\hat{a}}{\sqrt{2}}, \tag{A.41}$$

$$\delta\hat{Y} = \frac{i(\delta\hat{a}^\dagger - \delta\hat{a})}{\sqrt{2}}, \tag{A.42}$$

respectively. The quadratures of the drive, $\delta\hat{X}_{\mathrm{in}}$ and $\delta\hat{Y}_{\mathrm{in}}$, are defined in the same way with respect to $\delta\hat{a}_{\mathrm{in}}$. The Langevin equations are now linear and read

$$\delta\dot{\hat{X}} = -\frac{\kappa}{2}\delta\hat{X} - \Delta\delta\hat{Y} + \sqrt{\kappa}\delta\hat{X}_{\mathrm{in}}, \tag{A.43}$$

$$\delta\dot{\hat{Y}} = -\frac{\kappa}{2}\delta\hat{Y} + \Delta\delta\hat{X} - \frac{\sqrt{2}g}{q_{\mathrm{zp}}}\hat{q} + \sqrt{\kappa}\delta\hat{Y}_{\mathrm{in}}, \tag{A.44}$$

$$\dot{\hat{q}} = \frac{\hat{p}}{m_{\mathrm{eff}}}, \tag{A.45}$$

$$\dot{\hat{p}} = -m_{\mathrm{eff}}\Omega_{\mathrm{m}}^2\hat{q} - \Gamma_{\mathrm{m}}\hat{p} + \hat{F}_{\mathrm{th}} - \frac{\sqrt{2}\hbar g}{q_{\mathrm{zp}}}\delta\hat{X}. \tag{A.46}$$

As described in Section 2.2.3.3, the constant term neglected here give rise to a mean displacement and shifted detuning, both of which we can simply set to zero when investigating the dynamics of the system in the following discussion.

A.3.2 Dynamical backaction

The most important consequences of the optomechanical coupling, when using a strong optical drive as is the case in all of our experiments, can directly be inferred from the linearized Langevin equations above. Combining all Equations (A.43–46) we solve for the displacement $\hat{q}(\Omega)$ in Fourier domain and get

$$\hat{q}(\Omega) = \chi_{\mathrm{eff}}(\Omega)\left(\hat{F}_{\mathrm{th}}(\Omega) + \hat{F}_{\mathrm{ba}}(\Omega)\right), \tag{A.47}$$

which has a similar form as Equation (A.28) but with a fluctuating force due to radiation pressure back-action. This important feature will be discussed later. For the time being, consider that we have replaced $\chi_{\mathrm{m}}(\Omega)$ by an effective susceptibility:

$$\chi_{\mathrm{eff}}(\Omega)^{-1} \coloneqq \chi_{\mathrm{m}}(\Omega)^{-1} + \frac{i\hbar g^2}{q_{\mathrm{zp}}^2}\left(\chi_{\mathrm{c}}^*(-\Omega) - \chi_{\mathrm{c}}(\Omega)\right), \tag{A.48}$$

where the susceptibility $\chi_{\mathrm{c}}(\Omega)$ of the optical cavity has been introduced in analogy to Equation (A.15), whose squared magnitude is a Lorentzian function peaked at $\Omega = \Delta$ and with κ being the FWHM:

$$\chi_{\mathrm{c}}(\Omega)^{-1} \coloneqq \frac{\kappa}{2} - i(\Delta - \Omega). \tag{A.49}$$

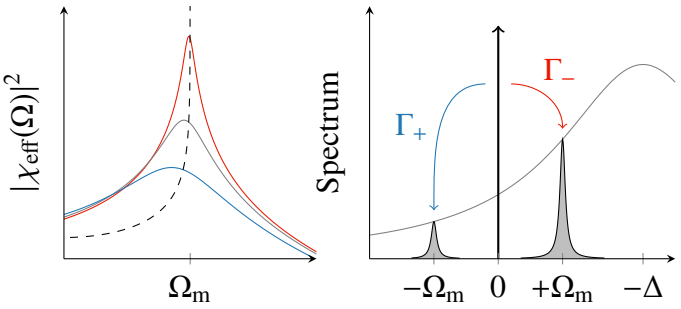

Figure A.4: Dynamical backaction for negative detuning. Left: Absolute square of mechanical susceptibility versus frequency, where we set $\kappa = -\Delta = \Omega_{\mathrm{m}}$. For g/Ω_{m} we used 0.1 (red), 0.2 (gray), and 0.3 (blue). The dashed line shows the maximum curve $|\chi_{\mathrm{eff}}(\Omega_{\mathrm{eff}})|^2$. Right: Scattering picture of optomechanical cooling. The cavity susceptibility $|\chi_{\mathrm{c}}(\Omega)|^2$ (gray line) weights the mechanical sidebands (gray shaded areas) around the optical carrier (black arrow) and thereby modifies the scattering rates Γ_- and Γ_+.

Defining $\chi_{\mathrm{eff}}(\Omega)^{-1} := m_{\mathrm{eff}}\left(\Omega_{\mathrm{eff}}^2 - \Omega^2 + i\Omega\Gamma_{\mathrm{eff}}\right)$ we find that the coupling changes the mechanical linewidth $\Gamma_{\mathrm{eff}} := \Gamma_{\mathrm{m}} + \Gamma_{\mathrm{opt}}$ (optical damping) and shifts the frequency $\Omega_{\mathrm{eff}}^2 := \Omega_{\mathrm{m}}^2 + \Omega_{\mathrm{opt}}^2$ (optical spring effect). With $\Omega = \Omega_{\mathrm{m}}$ we get

$$\Gamma_{\mathrm{opt}} = \kappa g^2 \left(|\chi_{\mathrm{c}}(\Omega_{\mathrm{m}})|^2 - |\chi_{\mathrm{c}}(-\Omega_{\mathrm{m}})|^2\right), \tag{A.50}$$

$$\Omega_{\mathrm{opt}}^2 = 2\Omega_{\mathrm{m}} g^2 \left((\Delta + \Omega_{\mathrm{m}})\,|\chi_{\mathrm{c}}(\Omega_{\mathrm{m}})|^2 + (\Delta - \Omega_{\mathrm{m}})\,|\chi_{\mathrm{c}}(-\Omega_{\mathrm{m}})|^2\right). \tag{A.51}$$

In Figure A.4 we show the absolute square of the effective susceptibility as a function of frequency for different values of g. Besides optical damping and the optical spring effect, we see that for $\Delta < 0$ the area underneath the curve decreases with g. Indeed, this is also true for the displacement PSD $S_{qq}(\Omega)$ calculated via Equation (A.47), if we discard the backaction force $\hat{F}_{\mathrm{ba}}$. Integrating $S_{qq}(\Omega)$, which is akin to Equation (A.31), we get the variance:

$$\langle \hat{q}^2 \rangle = \frac{\Gamma_{\mathrm{m}}}{\Gamma_{\mathrm{eff}}} \frac{\hbar(\bar{n}_{\mathrm{th}} + 1/2)}{m_{\mathrm{eff}}\Omega_{\mathrm{eff}}}. \tag{A.52}$$

In the classical limit $\bar{n}_{\mathrm{th}} \gg 1$ this result can be compared to the case without optomechanical coupling, i.e., Equation (A.52), suggesting an effective temperature of the mechanical resonator:

$$T_{\mathrm{eff}} = \frac{\Gamma_{\mathrm{m}}}{\Gamma_{\mathrm{m}} + \Gamma_{\mathrm{opt}}} T. \tag{A.53}$$

We thus see that the motion can be optically cooled ($T_{\mathrm{eff}} < T$) if $\Delta < 0$ and amplified ($T_{\mathrm{eff}} > T$) if $\Delta > 0$. The latter reaches an instability when $\Gamma_{\mathrm{eff}} < 0$, resulting in large coherent oscillations of the resonator.

The effects described above are referred to as 'dynamical backaction' and can be understood in two different ways: firstly, we recall that for $\Delta \neq 0$ the harmonic motion of the mechanical resonator modulates the amplitude quadrature of the intra-cavity field

and thus the radiation pressure force at the frequency Ω_m. If the force is delayed by the photon lifetime in the cavity $1/\kappa$, it is out-of-phase with the motion, creating a feedback which alters the energy stored in the mechanical resonator. The second picture to describe dynamical backaction is equivalent to Raman scattering of photons from atoms or molecules. Consider the two sidebands generated by the mechanical motion of the resonator illustrated in Figure A.4, which correspond to photons with energies $\hbar(\omega_\mathrm{l} + \Omega_\mathrm{m})$ (anti-Stokes scattering) and $\hbar(\omega_\mathrm{l} - \Omega_\mathrm{m})$ (Stokes scattering). If the cavity is detuned such that it enhances scattering of photons with higher energy and suppresses those with lower energy, phonons will be removed from the mechanical resonator, thus lowering the effective temperature. This is deduced from Equation (A.50), where the damping rate $\Gamma_\mathrm{opt} = \Gamma_- - \Gamma_+$ is given by the asymmetry of the downward (Γ_-) and upward (Γ_+) transition rates [10]. The two rates are proportional to the magnitude of the cavity susceptibility evaluated at different sideband frequencies:

$$\Gamma_- = g^2\kappa\,|\chi_\mathrm{c}(+\Omega_\mathrm{m})|^2, \tag{A.54}$$

$$\Gamma_+ = g^2\kappa\,|\chi_\mathrm{c}(-\Omega_\mathrm{m})|^2\,. \tag{A.55}$$

The theoretical description of dynamical backaction above is sufficient for many optomechanical systems, but it is not complete. We have so far discarded the backaction force in Equation (A.47):

$$\hat{F}_\mathrm{ba}(\Omega) = \frac{\sqrt{2\kappa}\hbar g}{q_\mathrm{zp}}\frac{\Delta\delta\hat{Y}_\mathrm{in} - (\kappa/2 + i\Omega)\delta\hat{X}_\mathrm{in}}{(\kappa/2 + i\Omega)^2 + \Delta^2}. \tag{A.56}$$

To incorporate this force into the model we want to find the backaction force PSD $S_{FF}^\mathrm{ba}(\Omega_\mathrm{m})$ using Equation (A.3) and assume that the input noise quadratures correspond to a coherent drive, so that in the rotating frame [11]

$$\langle\delta\hat{Y}_\mathrm{in}^\dagger(-\Omega)\delta\hat{Y}_\mathrm{in}(\Omega')\rangle = \langle\delta\hat{X}_\mathrm{in}^\dagger(-\Omega)\delta\hat{X}_\mathrm{in}(\Omega')\rangle = \frac{1}{2}\delta(\Omega + \Omega'), \tag{A.57}$$

$$\langle\delta\hat{Y}_\mathrm{in}^\dagger(-\Omega)\delta\hat{X}_\mathrm{in}(\Omega')\rangle = -\langle\delta\hat{X}_\mathrm{in}^\dagger(-\Omega)\delta\hat{Y}_\mathrm{in}(\Omega')\rangle = \frac{i}{2}\delta(\Omega + \Omega'). \tag{A.58}$$

The result is simply the Lorentzian cavity response which we evaluate at the mechanical resonance frequency:

$$S_{FF}^\mathrm{ba}(\Omega_\mathrm{m}) = \frac{\hbar^2 g^2\kappa}{q_\mathrm{zp}^2}\,|\chi_\mathrm{c}(\Omega_\mathrm{m})|^2\,. \tag{A.59}$$

$$= 2\hbar m_\mathrm{eff}\Omega_\mathrm{m}\Gamma_\mathrm{opt}\bar{n}_\mathrm{min}. \tag{A.60}$$

In the last line we used Equation (A.21) and Equation (A.50) to show that the backaction force behaves the same way as the thermal force described by the fluctuation dissipation theorem in Equation (A.29). As a matter of fact, we can say that the mechanical resonator couples with a rate Γ_opt to an optical bath whose occupancy is

$$\bar{n}_\mathrm{min} = -\frac{\kappa^2/4 + (\Delta + \Omega_\mathrm{m})^2}{4\Delta\Omega_\mathrm{m}}. \tag{A.61}$$

Integrating $S_{qq}(\Omega) = |\chi_{\mathrm{eff}}(\Omega)|^2(S_{FF}^{\mathrm{th}}(\Omega_{\mathrm{m}}) + S_{FF}^{\mathrm{ba}}(\Omega_{\mathrm{m}}))$, where both force PSDs are assumed to be constant across the mechanical linewidth Γ_{m}, we find that the variance of the displacement features an additional term compared to Equation (A.52). The effective temperature, or here the corresponding mean phonon occupancy $\bar{n}$, of the mechanical resonator is now given by

$$\bar{n} = \frac{\Gamma_{\mathrm{m}}\bar{n}_{\mathrm{th}} + \Gamma_{\mathrm{opt}}\bar{n}_{\mathrm{min}}}{\Gamma_{\mathrm{m}} + \Gamma_{\mathrm{opt}}}, \tag{A.62}$$

where we again assumed $\bar{n}_{\mathrm{th}} \gg 1$. In most cases $\Gamma_{\mathrm{m}} \ll \Gamma_{\mathrm{opt}}$, meaning that $\bar{n}_{\mathrm{min}}$ denotes the minimum occupancy achievable through optical cooling (backaction limit).

A.3.3 Standard quantum limit

Let us now turn our attention to the weak, continuous measurement of the mechanical displacement $\hat{q}$ using the reflected light from the cavity $\hat{a}_{\mathrm{out}}$ (see Figure A.3). We are interested in the precision achievable without altering the mechanical response, i.e., $\chi_{\mathrm{eff}}(\Omega) = \chi_{\mathrm{m}}(\Omega)$, and therefore choose the frequency of the input laser light $\hat{a}_{\mathrm{in}}$ such that $\Delta = 0$. In this case, the linearized Langevin equations reveal that $\hat{q}$ only couples to the phase quadrature of the intra-cavity field $\delta\hat{Y}$, as can be seen in Equation (A.44). The output field with $\hat{a}_{\mathrm{out}} = \alpha_{\mathrm{out}} + \delta\hat{a}_{\mathrm{out}}$, where α_{out} is the coherent amplitude and $\delta\hat{a}_{\mathrm{out}}$ denotes small fluctuations, allows us to access $\hat{q}$ and is given by the following input-output relation

$$\delta\hat{Y}_{\mathrm{out}} = \delta\hat{Y}_{\mathrm{in}} - \sqrt{\kappa}\delta\hat{Y}, \tag{A.63}$$

where $\delta\hat{Y}_{\mathrm{out}} = i(\delta\hat{a}_{\mathrm{out}}^{\dagger} - \delta\hat{a}_{\mathrm{out}})/\sqrt{2}$. In Fourier domain, the solution of Equation (A.44) is inserted in Equation (A.63), resulting in

$$\delta\hat{Y}_{\mathrm{out}}(\Omega) = \frac{\sqrt{2\kappa}g}{q_{\mathrm{zp}}(\kappa/2 + i\Omega)}\hat{q}(\Omega) - \frac{\kappa/2 - i\Omega}{\kappa/2 + i\Omega}\delta\hat{Y}_{\mathrm{in}}(\Omega). \tag{A.64}$$

Next, we want to calculate the PSD of the output phase fluctuations $S_{YY}^{\mathrm{out}}(\Omega)$ and transform it into units of $\mathrm{m}^2\,\mathrm{Hz}^{-1}$ dividing by the absolute square of the prefactor in the first term of Equation (A.64). The transformed PSD is

$$S_{qq}^{\mathrm{out}}(\Omega) \coloneqq \frac{2\Gamma_{\mathrm{meas}}}{q_{\mathrm{zp}}^2}S_{YY}^{\mathrm{out}}(\Omega), \tag{A.65}$$

where we use the measurement rate $\Gamma_{\mathrm{meas}} = 4g^2/\kappa$. Now, the PSD is found using Equation (A.3) and by considering the quadrature correlations in Equations (A.57) and (A.58):

$$S_{qq}^{\mathrm{out}}(\Omega) = |\chi_{\mathrm{m}}(\Omega)|^2\left(S_{FF}^{\mathrm{th}}(\Omega) + S_{FF}^{\mathrm{ba}}(\Omega)\right) + S_{qq}^{\mathrm{imp}}(\Omega) + \hbar\mathrm{Im}\left(\chi_{\mathrm{m}}(-\Omega)\right). \tag{A.66}$$

The expression consists of four terms: the first two describe the mechanical motion excited by the thermal force and the backaction force, both of which we have already

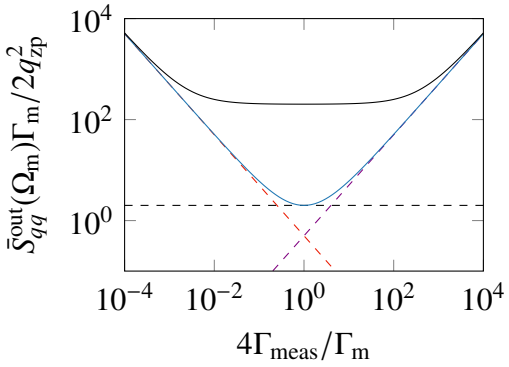

Figure A.5: Standard quantum limit of weak, continuous position measurements. Calculated displacement PSD $\bar{S}^{\mathrm{out}}_{qq}(\Omega_\mathrm{m})$ if measured using laser light reflected from an optomechanical cavity with $\Delta = 0$. The values are normalized to the peak displacement of the mechanical resonator in the ground state and plotted as a function of probing strength $4\Gamma_\mathrm{meas}/\Gamma_\mathrm{m} \propto g^2$ for $\bar{n} = 0$ (solid blue line) and $\bar{n} = 100$ (solid black line). The red and purple dashed lines are $S^{\mathrm{imp}}_{qq}(\Omega_\mathrm{m})$ and $|\chi_\mathrm{m}(\Omega_\mathrm{m})|^2 S^{\mathrm{ba}}_{FF}(\Omega_\mathrm{m})$, respectively. The black, horizontal dashed line at $\bar{S}^{\mathrm{out}}_{qq}(\Omega_\mathrm{m})\Gamma_\mathrm{m}/2q^2_\mathrm{zp} = 2$ indicates the standard quantum limit.

encountered in the previous sections. The third term denotes the imprecision due to the SN of the probe beam and is given by

$$S^{\mathrm{imp}}_{qq}(\Omega) = \frac{q^2_\mathrm{zp}}{4\Gamma_\mathrm{meas}}. \tag{A.67}$$

The last term in Equation (A.66) describes correlations between the imprecision noise and the backaction noise, both derived from the vacuum fluctuations of the probe beam. It vanishes in the case of homodyne detection, where the symmetrized spectrum $\bar{S}^{\mathrm{out}}_{qq}(\Omega)$ is measured, and cancels in the case of heterodyne detection with a cross-term in the amplitude quadrature $\delta\hat{X}_\mathrm{out}$, which needs to be taken into account (see Section 2.3.1). In Figure A.5 we evaluate the symmetrized spectrum at the mechanical resonance and plot it as a function of $4\Gamma_\mathrm{meas}/\Gamma_\mathrm{m} \propto g^2 \propto \alpha^2$, where the latter is the number of photons in the cavity. If the mechanical resonator is in the ground state with $\bar{n} = 0$, we see that the imprecision noise $\bar{S}^{\mathrm{imp}}_{qq}(\Omega_\mathrm{m})$ dominates for $4\Gamma_\mathrm{meas}/\Gamma_\mathrm{m} < 1$. On the other hand, if $4\Gamma_\mathrm{meas}/\Gamma_\mathrm{m} > 1$, noise due to the backaction $|\chi_\mathrm{m}(\Omega_\mathrm{m})|^2 \bar{S}^{\mathrm{ba}}_{FF}(\Omega_\mathrm{m})$ is prevalent. At $4\Gamma_\mathrm{meas}/\Gamma_\mathrm{m} = 1$ the PSD reaches a minimum that is known as the standard quantum limit. Here the imprecision and the backaction are the same, while their sum is equal to the noise of the mechanical resonator in the ground state. In essence, the added noise is a consequence of the Heisenberg uncertainty principle, prohibiting arbitrary precision on the displacement measurement via backaction. Indeed, in this context we can express the uncertainty principle in the following way:

$$S^{\mathrm{imp}}_{qq}(\Omega) S^{\mathrm{ba}}_{FF}(\Omega) \geq \frac{\hbar^2}{4}. \tag{A.68}$$

The equality is realized in our case of a perfectly coherent laser drive, as is readily deduced from Equation (A.59) and Equation (A.67).

Finally, let us consider the case where the resonator is thermally excited and $\bar{n}_{\mathrm{th}} \gg 1$. For very large values of $4\Gamma_{\mathrm{meas}}/\Gamma_{\mathrm{m}}$ the backaction force can exceed the thermal force. In order to quantify this regime we define the quantum cooperativity

$$C_{\mathrm{q}} \coloneqq \frac{S_{FF}^{\mathrm{ba}}(\Omega_{\mathrm{m}})}{S_{FF}^{\mathrm{th}}(\Omega_{\mathrm{m}})} = \frac{\Gamma_{\mathrm{meas}}}{\Gamma_{\mathrm{m}}\bar{n}_{\mathrm{th}}}. \tag{A.69}$$

We note that the measurement rate Γ_{meas} may be interpreted as the rate at which information about $\hat{q}$ is extracted. C_{q} compares this rate to the decoherence rate $\Gamma_{\mathrm{m}}\bar{n}_{\mathrm{th}}$ (see Equation (A.26)), describing how fast a given quantum state degrades. In other words, quantum coherent interaction between the mechanical resonator and the light is enabled if $C_{\mathrm{q}} > 1$.

A.4 Transfer-matrix method

We will now outline the transfer-matrix method for optical multilayer used in this thesis. For a thorough derivation of the method the reader is referred to [174] whose notation we adapt in the following.

Consider a beam of light at a wavelength λ with an electric field E_{in} impinging on a stack of N optical layers. The reflected field E_{refl} and transmitted field E_{trans} are found by the linear equation

$$\begin{pmatrix} E_{\mathrm{in}} \\ E_{\mathrm{refl}} \end{pmatrix} = \mathbf{M}_{0,1} \prod_{j=1}^{N} \mathbf{P}_j \mathbf{M}_{j,j+1} \begin{pmatrix} E_{\mathrm{trans}} \\ 0 \end{pmatrix} \tag{A.70}$$

$$= \begin{pmatrix} T_{11} & T_{12} \\ T_{21} & T_{22} \end{pmatrix} \begin{pmatrix} E_{\mathrm{trans}} \\ 0 \end{pmatrix}. \tag{A.71}$$

The 2×2 matrix in Equation (A.71) is the transfer matrix and gives the amplitude reflection and transmission coefficients of the optical multilayer as $r = T_{21}/T_{11}$ and $t = 1/T_{11}$, respectively. The propagation matrix $\mathbf{P}_j$ and refraction matrix $\mathbf{M}_{j,j+1}$ describe the relation between electric fields at each layer j and are defined as follows:

$$\mathbf{P}_j = \begin{pmatrix} e^{ikn_j d_j} & 0 \\ 0 & e^{-ikn_j d_j} \end{pmatrix}, \tag{A.72}$$

$$\mathbf{M}_{j,j+1} = \frac{1}{t_{j,j+1}} \begin{pmatrix} 1 & r_{j,j+1} \\ r_{j,j+1} & 1 \end{pmatrix}. \tag{A.73}$$

Here n_j is the (complex) refractive index and d_j the thickness of layer j, while $k = 2\pi/\lambda$. At the interface between layer j and $j+1$ the reflection and transmission coefficients are denoted $r_{j,j+1}$ and $t_{j,j+1}$, respectively. These can be specified directly, for instance, to include a mirror with known reflectance and transmittance. Alternatively, they are

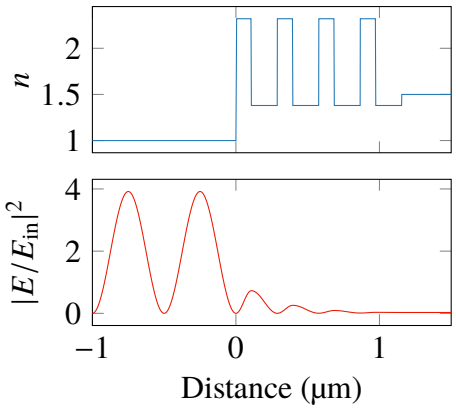

Figure A.6: Transfer-matrix method for a dielectric mirror. Given the refractive indices n of alternating layers (top), we calculate the normalized squared electric field $|E/E_{\text{in}}|^2$ of an incident plane wave (bottom) as a function of distance from the mirror surface.

given by the Fresnel relations (at normal incidence) [98]

$$r_{j,j+1} = \frac{n_j - n_{j+1}}{n_j + n_{j+1}}, \tag{A.74}$$

$$t_{j,j+1} = \frac{2n_j}{n_j + n_{j+1}}. \tag{A.75}$$

To demonstrate this method, we take a lossless dielectric mirror on a glass substrate, where the coating materials are magnesium fluoride ($n_{\text{MgF}_2} = 1.38$) and zinc sulfide ($n_{\text{ZnS}} = 2.32$). Figure A.6 shows the arrangement of $N = 8$ alternating layers, each with a thickness of $n_j d_j = \lambda/4$, where $\lambda = 1\,\mu\text{m}$. We find the coefficients $r \approx -0.979$ and $t \approx 0.165$. The electric field of an incident plane wave penetrates the mirror stack with a depth of $\sim \lambda/2$ as also described in [88].

A.5 Jones calculus

Jones calculus is used to model the polarization state of light as it travels through different optical elements. We will now briefly sketch this method and introduce the identities used in this thesis. A more detailed introduction can be found in [175].

The electric field of a polarized plane wave is orthogonal to the direction of propagation and can be described by a two-dimensional vector z in the $xy-$plane:

$$\vec{E} = \frac{1}{\sqrt{E_x^2 + E_y^2}} \begin{pmatrix} E_x e^{i\phi_x} \\ E_y e^{i\phi_y} \end{pmatrix}, \tag{A.76}$$

where we omit the complex exponential including the time and position dependence of the wave. $\vec{E}$ is known as the normalized Jones vector and describes linear horizontal

and vertical polarization if the components $E_y = 0$ and $E_x = 0$, respectively. For right-circularly polarized light we set $E_x = E_y$, $\phi_x = 0$ and $\phi_y = -\pi/2$ such that:

$$\vec{E}_{\mathrm{RH}} = \frac{1}{\sqrt{2}} \begin{pmatrix} 1 \\ -i \end{pmatrix}. \tag{A.77}$$

Optical elements that change the polarization of light are represented by Jones matrices of dimension 2×2 which are simply multiplied with the Jones vector. The most general phase retarder is given by

$$\mathbf{J}_{\delta,\theta} = \mathbf{R}_\theta^{-1} \begin{pmatrix} e^{-i\delta} & 0 \\ 0 & e^{i\delta} \end{pmatrix} \mathbf{R}_\theta, \tag{A.78}$$

where δ denotes the relative phase between the fast and slow axis. The azimuth angle θ between x and the fast axis accommodates for any rotation of the element with respect to the basis, which we express by the rotation matrix

$$\mathbf{R}_\theta = \begin{pmatrix} \cos\theta & -\sin\theta \\ \sin\theta & \cos\theta \end{pmatrix}. \tag{A.79}$$

As an example, an arbitrarily-rotated half-wave plate with $\delta = \pi$ yields a rotation of the polarization state by -2θ and reads

$$\mathbf{J}_{\pi,\theta} = e^{-i\pi/2} \begin{pmatrix} \cos 2\theta & -\sin 2\theta \\ -\sin 2\theta & -\cos 2\theta \end{pmatrix}. \tag{A.80}$$

Finally, a horizontal linear polarizer selects the $x-$component of the Jones vector and is therefore given by

$$\mathbf{P} = \begin{pmatrix} 1 & 0 \\ 0 & 0 \end{pmatrix}. \tag{A.81}$$

Bibliography

[1] A. Barg, Y. Tsaturyan, E. Belhage, W. H. P. Nielsen, C. B. Møller, A. Schliesser. Measuring and imaging nanomechanical motion with laser light. Applied Physics B, 123, 8 (2016).

[2] T. Capelle, Y. Tsaturyan, A. Barg, A. Schliesser. Polarimetric analysis of stress anisotropy in nanomechanical silicon nitride resonators. Applied Physics Letters, 110, 181106 (2017).

[3] Y. Tsaturyan, A. Barg, E. S. Polzik, A. Schliesser. Ultracoherent nanomechanical resonators via soft clamping and dissipation dilution. Nature Nanotechnology, 12, 776–783 (2017).

[4] A. Barg, L. Midolo, G. Kiršanskė, P. Tighineanu, T. Pregnolato, A. İmamoğlu, P. Lodahl, A. Schliesser, S. Stobbe, E. S. Polzik. Carrier-mediated optomechanical forces in semiconductor nanomembranes with coupled quantum wells. Physical Review B, 98, 155316 (2018).

[5] A. Schliesser, Y. Tsaturyan, E. S. Polzik, A. Barg. Mechanical resonator device. World Intellectual Property Organization, WO 2018/024713 A1 (2018).

[6] M. Planck. Über das Gesetz der Energieverteilung im Normalspectrum. Annalen der Physik, 4, 1 (1901).

[7] A. Einstein. Über einen die Erzeugung und Verwandlung des Lichtes betreffenden heuristischen Gesichtspunkt. Annalen der Physik, 322, 132–148 (1905).

[8] J. P. Dowling, G. J. Milburn. Quantum technology: The second quantum revolution. Philosophical Transactions of the Royal Society of London A, 361, 1655–1674 (2003).

[9] J. L. O'brien, A. Furusawa, J. Vučković. Photonic quantum technologies. Nature Photonics, 3, 687–695 (2009).

[10] M. Aspelmeyer, T. J. Kippenberg, F. Marquardt. Cavity optomechanics. Reviews of Modern Physics, 86, 1391 (2014).

[11] W. Bowen, G. J. Milburn: Quantum optomechanics, CRC Press (2015).

[12] J. Chan, T. M. Alegre, A. H. Safavi-Naeini, J. T. Hill, A. Krause, S. Gröblacher, M. Aspelmeyer, O. Painter. Laser cooling of a nanomechanical oscillator into its quantum ground state. Nature, 478, 89–92 (2011).

[13] J. D. Teufel, T. Donner, D. Li, J. W. Harlow, M. S. Allman, K. Cicak, A. J. Sirois, J. D. Whittaker, K. W. Lehnert, R. W. Simmonds. Sideband cooling of micromechanical motion to the quantum ground state. Nature, 475, 359–363 (2011).

[14] K. L. Ekinci, M. L. Roukes. Nanoelectromechanical systems. Review of Scientific Instruments, 76, 061101 (2005).

[15] M. Imboden, P. Mohanty. Dissipation in nanoelectromechanical systems. Physics Reports, 534, 89–146 (2014).

[16] G. I. González, P. R. Saulson. Brownian motion of a mass suspended by an anelastic wire. The Journal of the Acoustical Society of America, 96, 207–212 (1994).

[17] S. S. Verbridge, H. G. Craighead, J. M. Parpia. A megahertz nanomechanical resonator with room temperature quality factor over a million. Applied Physics Letters, 92, 013112 (2008).

[18] B. M. Zwickl, W. E. Shanks, A. M. Jayich, C. Yang, A. C. Bleszynski Jayich, J. D. Thompson, J. G. E. Harris. High quality mechanical and optical properties of commercial silicon nitride membranes. Applied Physics Letters, 92, 103125 (2008).

[19] C. Reinhardt, T. Müller, A. Bourassa, J. C. Sankey. Ultralow-noise SiN trampoline resonators for sensing and optomechanics. Physical Review X, 6, 021001 (2016).

[20] R. A. Norte, J. P. Moura, S. Gröblacher. Mechanical resonators for quantum optomechanics experiments at room temperature. Physical Review Letters, 116, 147202 (2016).

[21] I. Wilson-Rae. Intrinsic dissipation in nanomechanical resonators due to phonon tunneling. Physical Review B, 77, 245418 (2008).

[22] P.-L. Yu, K. Cicak, N. S. Kampel, Y. Tsaturyan, T. P. Purdy, R. W. Simmonds, C. A. Regal. A phononic bandgap shield for high-Q membrane microresonators. Applied Physics Letters, 104, 023510 (2014).

[23] Y. Tsaturyan, A. Barg, A. Simonsen, L. G. Villanueva, S. Schmid, A. Schliesser, E. S. Polzik. Demonstration of suppressed phonon tunneling losses in phononic bandgap shielded membrane resonators for high-Q optomechanics. Optics Express, 22, 6810–6821 (2014).

[24] A. Barg: Optical characterization of micromechanical membranes, Master's thesis, University of Copenhagen (2014).

[25] U. Leonhardt: Measuring the quantum state of light, vol. 22, Cambridge University Press (1997).

[26] S. Steinlechner, B. W. Barr, A. S. Bell, S. L. Danilishin, A. Gläfke, C. Gräf, J.-S. Hennig, E. A. Houston, S. H. Huttner, S. S. Leavey, D. Pascucci, B. Sorazu, A. Spencer, K. A. Strain, J. Wright, S. Hild. Local-oscillator noise coupling in balanced homodyne readout for advanced gravitational wave detectors. Physical Review D, 92, 072009 (2015).

[27] S. Chakram, Y. S. Patil, L. Chang, M. Vengalattore. Dissipation in ultrahigh quality factor SiN membrane resonators. Physical Review Letters, 112, 127201 (2014).

[28] W. Lauterborn, T. Kurz: Coherent optics: Fundamentals and Applications, Springer Science & Business Media (2013).

[29] A. Ajovalasit, G. Petrucci, M. Scafidi. A critical assessment of automatic photoelastic methods for the analysis of edge residual stresses in glass. The Journal of Strain Analysis for Engineering Design, 49, 361–375 (2014).

[30] R. Priestley. Birefringence dispersion in fused silica for DUV lithography. Proc.SPIE, 4346, 1300–1306 (2001).

[31] A. L. Campillo, J. W. P. Hsu. Near-field scanning optical microscope studies of the anisotropic stress variations in patterned SiN membranes. Journal of Applied Physics, 91, 646–651 (2002).

[32] P. A. Deymier: Acoustic metamaterials and phononic crystals, vol. 173, Springer Science & Business Media (2013).

[33] M. Eichenfield, J. Chan, R. M. Camacho, K. J. Vahala, O. Painter. Optomechanical crystals. Nature, 462, 78–82 (2009).

[34] W. H. P. Nielsen, Y. Tsaturyan, C. B. Møller, E. S. Polzik, A. Schliesser. Multimode optomechanical system in the quantum regime. Proceedings of the National Academy of Sciences, 114, 62–66 (2017).

[35] C. B. Møller, R. A. Thomas, G. Vasilakis, E. Zeuthen, Y. Tsaturyan, M. Balabas, K. Jensen, A. Schliesser, K. Hammerer, E. S. Polzik. Quantum back-action-evading measurement of motion in a negative mass reference frame. Nature, 547, 191–195 (2017).

[36] J. E.-Y. Lee, A. A. Seshia. 5.4-MHz single-crystal silicon wine glass mode disk resonator with quality factor of 2 million. Sensors and Actuators A: Physical, 156, 28–35 (2009).

[37] A. V. Cumming, A. S. Bell, L. Barsotti, M. A. Barton, G. Cagnoli, D. Cook, L. Cunningham, M. Evans, G. D. Hammond, G. M. Harry, A. Heptonstall, J. Hough, R. Jones, R. Kumar, R. Mittleman, N. A. Robertson, S. Rowan, B. Shapiro, K. A. Strain, K. Tokmakov, C. Torrie, A. A. van Veggel. Design and development of the advanced LIGO monolithic fused silica suspension. Classical and Quantum Gravity, 29, 035003 (2012).

[38] S. Schmid, L. G. Villanueva, M. L. Roukes: Fundamentals of nanomechanical resonators, Springer (2016).

[39] M. Bao, H. Yang, H. Yin, Y. Sun. Energy transfer model for squeeze-film air damping in low vacuum. Journal of Micromechanics and Microengineering, 12, 341 (2002).

[40] A. Jöckel, M. T. Rakher, M. Korppi, S. Camerer, D. Hunger, M. Mader, P. Treutlein. Spectroscopy of mechanical dissipation in micro-mechanical membranes. Applied Physics Letters, 99, 143109 (2011).

[41] R. Lifshitz, M. L. Roukes. Thermoelastic damping in micro-and nanomechanical systems. Physical Review B, 61, 5600 (2000).

[42] R. Tabrizian, M. Rais-Zadeh, F. Ayazi. Effect of phonon interactions on limiting the f.Q product of micromechanical resonators. Solid-State Sensors, Actuators and Microsystems Conference, 2009. TRANSDUCERS 2009. International, pp. 2131–2134 (2009).

[43] S. Ghaffari, S. A. Chandorkar, S. Wang, E. J. Ng, C. H. Ahn, V. Hong, Y. Yang, T. W. Kenny. Quantum limit of quality factor in silicon micro and nano mechanical resonators. Scientific Reports, 3, 3244 (2013).

[44] R. Vacher, E. Courtens, M. Foret. Anharmonic versus relaxational sound damping in glasses. II. Vitreous silica. Physical Review B, 72, 214205 (2005).

[45] T. Faust, J. Rieger, M. J. Seitner, J. P. Kotthaus, E. M. Weig. Signatures of two-level defects in the temperature-dependent damping of nanomechanical silicon nitride resonators. Physical Review B, 89, 100102 (2014).

[46] Q. P. Unterreithmeier, T. Faust, J. P. Kotthaus. Damping of nanomechanical resonators. Physical Review Letters, 105, 027205 (2010).

[47] S. Schmid, K. Jensen, K. Nielsen, A. Boisen. Damping mechanisms in high-Q micro and nanomechanical string resonators. Physical Review B, 84, 165307 (2011).

[48] P.-L. Yu, T. P. Purdy, C. A. Regal. Control of material damping in high-Q membrane microresonators. Physical Review Letters, 108, 083603 (2012).

[49] A. N. Cleland: Foundations of Nanomechanics: From Solid-State Theory to Device Applications, Springer Science & Business Media (2013).

[50] L. G. Villanueva, S. Schmid. Evidence of surface loss as ubiquitous limiting damping mechanism in SiN micro-and nanomechanical resonators. Physical Review Letters, 113, 227201 (2014).

[51] Q. A. Turchette, Kielpinski, B. E. King, D. Leibfried, D. M. Meekhof, C. J. Myatt, M. A. Rowe, C. A. Sackett, C. S. Wood, W. M. Itano, C. Monroe, D. J. Wineland. Heating of trapped ions from the quantum ground state. Physical Review A, 61, 063418 (2000).

[52] A. A. Clerk, M. H. Devoret, S. M. Girvin, F. Marquardt, R. J. Schoelkopf. Introduction to quantum noise, measurement, and amplification. Reviews of Modern Physics, 82, 1155 (2010).

[53] C. L. Degen, F. Reinhard, P. Cappellaro. Quantum sensing. Reviews of Modern Physics, 89, 035002 (2017).

[54] J. Moser, J. Güttinger, A. Eichler, M. J. Esplandiu, D. Liu, M. Dykman, A. Bachtold. Ultrasensitive force detection with a nanotube mechanical resonator. Nature Nanotechnology, 8, 493–496 (2013).

[55] M. S. Hanay, S. Kelber, A. K. Naik, D. Chi, S. Hentz, E. C. Bullard, E. Colinet, L. Duraffourg, M. L. Roukes. Single-protein nanomechanical mass spectrometry in real time. Nature Nanotechnology, 7, 602–608 (2012).

[56] T. Bagci, A. Simonsen, S. Schmid, L. G. Villanueva, E. Zeuthen, J. Appel, J. M. Taylor, A. Sørensen, K. Usami, A. Schliesser, E. S. Polzik. Optical detection of radio waves through a nanomechanical transducer. Nature, 507, 81–85 (2014).

[57] M. Poggio, C. Degen. Force-detected nuclear magnetic resonance: Recent advances and future challenges. Nanotechnology, 21, 342001 (2010).

[58] Y. Tsaturyan, M. B. Kristensen, A. Schliesser. Manuscript in preparation.

[59] Y. Tsaturyan: Ultra-high Q micromechanical resonators for cavity optomechanics, Master's thesis, University of Copenhagen (2016).

[60] A. Ghadimi, S. Fedorov, N. Engelsen, M. Bereyhi, R. Schilling, D. Wilson, T. Kippenberg. Elastic strain engineering for ultralow mechanical dissipation. Science, 360, 764–768 (2018).

[61] P. Lebedew. Untersuchungen über die Druckkräfte des Lichtes. Annalen der Physik, 311, 433–458 (1901).

[62] E. F. Nichols, G. F. Hull. A preliminary communication on the pressure of heat and light radiation. Physical Review (Series I), 13, 307 (1901).

[63] V. Braginski, A. Manukin. Ponderomotive effects of electromagnetic radiation. Soviet physics, JETP, 25, 653–655 (1967).

[64] V. B. Braginskii, A. B. Manukin, M. Y. Tikhonov. Investigation of dissipative ponderomotive effects of electromagnetic radiation. Soviet Journal of Experimental and Theoretical Physics, 31, 829 (1970).

[65] S. Gigan, H. Böhm, M. Paternostro, F. Blaser, G. Langer, J. Hertzberg, K. C. Schwab, D. Bäuerle, M. Aspelmeyer, A. Zeilinger. Self-cooling of a micromirror by radiation pressure. Nature, 444, 67–70 (2006).

[66] A. Schliesser, P. Del'Haye, N. Nooshi, K. J. Vahala, T. J. Kippenberg. Radiation pressure cooling of a micromechanical oscillator using dynamical backaction. Physical Review Letters, 97, 243905 (2006).

[67] S. Gröblacher, J. B. Hertzberg, M. R. Vanner, G. D. Cole, S. Gigan, K. C. Schwab, M. Aspelmeyer. Demonstration of an ultracold micro-optomechanical oscillator in a cryogenic cavity. Nature Physics, 5, 485–488 (2009).

[68] A. D. O'Connell, M. Hofheinz, M. Ansmann, R. C. Bialczak, M. Lenander, E. Lucero, M. Neeley, D. Sank, H. Wang, M. Weides, J. Wenner, J. M. Martinis, A. N. Cleland. Quantum ground state and single-phonon control of a mechanical resonator. Nature, 464, 697–703 (2010).

[69] D. J. Wineland, R. E. Drullinger, F. L. Walls. Radiation-pressure cooling of bound resonant absorbers. Physical Review Letters, 40, 1639 (1978).

[70] K. W. Murch, K. L. Moore, S. Gupta, D. M. Stamper-Kurn. Observation of quantum-measurement backaction with an ultracold atomic gas. Nature Physics, 4, 561–564 (2008).

[71] T. P. Purdy, R. W. Peterson, C. A. Regal. Observation of radiation pressure shot noise on a macroscopic object. Science, 339, 801–804 (2013).

[72] J. Hertzberg, T. Rocheleau, T. Ndukum, M. Savva, A. Clerk, K. Schwab. Back-action-evading measurements of nanomechanical motion. Nature Physics, 6, 213–217 (2010).

[73] I. Shomroni, L. Qiu, D. Malz, A. Nunnenkamp, T. J. Kippenberg. Optical backaction-evading measurement of a mechanical oscillator. arXiv:1809.01007 (2018).

[74] C. Ockeloen-Korppi, E. Damskägg, J.-M. Pirkkalainen, A. Clerk, M. Woolley, M. Sillanpää. Quantum backaction evading measurement of collective mechanical modes. Physical Review Letters, 117, 140401 (2016).

[75] J. Thompson, B. Zwickl, A. Jayich, F. Marquardt, S. Girvin, J. Harris. Strong dispersive coupling of a high-finesse cavity to a micromechanical membrane. Nature, 452, 72–75 (2008).

[76] D. J. Wilson, C. A. Regal, S. B. Papp, H. J. Kimble. Cavity optomechanics with stoichiometric SiN films. Physical Review Letters, 103, 207204 (2009).

[77] M. Underwood, D. Mason, D. Lee, H. Xu, L. Jiang, A. Shkarin, K. Børkje, S. Girvin, J. Harris. Measurement of the motional sidebands of a nanogram-scale oscillator in the quantum regime. Physical Review A, 92, 061801 (2015).

[78] R. W. Peterson, T. P. Purdy, N. S. Kampel, R. W. Andrews, P.-L. Yu, K. W. Lehnert, C. A. Regal. Laser cooling of a micromechanical membrane to the quantum backaction limit. Physical Review Letters, 116, 063601 (2016).

[79] T. P. Purdy, P.-L. Yu, R. W. Peterson, N. S. Kampel, C. A. Regal. Strong optomechanical squeezing of light. Physical Review X, 3, 031012 (2013).

[80] D. Lee, M. Underwood, D. Mason, A. B. Shkarin, S. W. Hoch, J. G. E. Harris. Multimode optomechanical dynamics in a cavity with avoided crossings. Nature Communications, 6, 6232 (2015).

[81] P. Piergentili, L. Catalini, M. Bawaj, S. Zippilli, N. Malossi, R. Natali, D. Vitali, G. D. Giuseppe. Two-membrane cavity optomechanics. New Journal of Physics, 20, 083024 (2018).

[82] C. Gärtner, J. P. Moura, W. Haaxman, R. A. Norte, S. Gröblacher. Integrated optomechanical arrays of two high reflectivity SiN membranes. Nano Letters (2018).

[83] C. Stambaugh, H. Xu, U. Kemiktarak, J. Taylor, J. Lawall. From membrane-in-the-middle to mirror-in-the-middle with a high-reflectivity sub-wavelength grating. Annalen der Physik, 527, 81–88 (2015).

[84] M. D'Agostino. Focus: Schrödinger's Drum. Physical Review Focus, 22, 16 (2008).

[85] F. Y. Khalili, E. S. Polzik. Overcoming the standard quantum limit in gravitational wave detectors using spin systems with a negative effective mass. Physical Review Letters, 121, 031101 (2018).

[86] X. Huang, E. Zeuthen, D. V. Vasilyev, Q. He, K. Hammerer, E. S. Polzik. Unconditional steady-state entanglement in macroscopic hybrid systems by coherent noise cancellation. Physical Review Letters, 121, 103602 (2018).

[87] M. Rossi, D. Mason, J. Chen, Y. Tsaturyan, A. Schliesser. Measurement-based quantum control of mechanical motion. Nature, 563, 53–58 (2018).

[88] D. J. Wilson: Cavity optomechanics with high-stress silicon nitride films, Ph.D. thesis, California Institute of Technology (2012).

[89] M. J. Underwood III: Cryogenic optomechanics with a silicon nitride membrane, Ph.D. thesis, Yale University (2016).

[90] H. Miao, S. Danilishin, T. Corbitt, Y. Chen. Standard quantum limit for probing mechanical energy quantization. Physical Review Letters, 103, 100402 (2009).

[91] A. M. Jayich, J. C. Sankey, B. M. Zwickl, C. Yang, J. D. Thompson, S. M. Girvin, A. A. Clerk, F. Marquardt, J. G. E. Harris. Dispersive optomechanics: a membrane inside a cavity. New Journal of Physics, 10, 095008 (2008).

[92] D. Kleckner, D. Bouwmeester. Sub-kelvin optical cooling of a micromechanical resonator. Nature, 444, 75–78 (2006).

[93] S. Gröblacher, K. Hammerer, M. R. Vanner, M. Aspelmeyer. Observation of strong coupling between a micromechanical resonator and an optical cavity field. Nature, 460, 724–727 (2009).

[94] U. Kemiktarak, M. Durand, M. Metcalfe, J. Lawall. Cavity optomechanics with sub-wavelength grating mirrors. New Journal of Physics, 14, 125010 (2012).

[95] C. H. Bui, J. Zheng, S. Hoch, L. Y. T. Lee, J. G. E. Harris, C. Wei Wong. High-reflectivity, high-Q micromechanical membranes via guided resonances for enhanced optomechanical coupling. Applied Physics Letters, 100, 021110 (2012).

[96] K. Makles, T. Antoni, A. G. Kuhn, S. Deléglise, T. Briant, P.-F. Cohadon, R. Braive, G. Beaudoin, L. Pinard, C. Michel, V. Dolique, R. Flaminio, G. Cagnoli, I. Robert-Philip, A. Heidmann. 2D photonic-crystal optomechanical nanoresonator. Optics letters, 40, 174–177 (2015).

[97] P. W. Milonni, J. H. Eberly: Laser Physics, Wiley (2010).

[98] E. Hecht: Optics, Fourth Edition, Addison-Wesley, San Francisco (2002).

[99] W. H. P. Nielsen: Quantum cavity optomechanics with phononic bandgap shielded silicon nitride membranes, Ph.D. thesis, University of Copenhagen (2016).

[100] E. D. Black. An introduction to Pound-Drever-Hall laser frequency stabilization. American Journal of Physics, 69, 79–87 (2001).

[101] S. Weis, R. Rivière, S. Deléglise, E. Gavartin, O. Arcizet, A. Schliesser, T. J. Kippenberg. Optomechanically induced transparency. Science, 330, 1520–1523 (2010).

[102] C. B. Møller: Quantum back-action evasion in a hybrid spin-optomechanical system, Ph.D. thesis, University of Copenhagen (2018).

[103] A. Schliesser: Cavity optomechanics and optical frequency comb generation with silica whispering-gallery-mode microresonators, Ph.D. thesis, Ludwig-Maximilians-Universität München (2009).

[104] T. P. Purdy, R. W. Peterson, P. L. Yu, C. A. Regal. Cavity optomechanics with Si_3N_4 membranes at cryogenic temperatures. New Journal of Physics, 14, 115021 (2012).

[105] A. E. Siegman. Lasers. Mill Valley, CA, 37, 208 (1986).

[106] A. H. Safavi-Naeini, J. Chan, J. T. Hill, T. P. M. Alegre, A. Krause, O. Painter. Observation of quantum motion of a nanomechanical resonator. Physical Review Letters, 108, 033602 (2012).

[107] T. P. Purdy, P.-L. Yu, N. S. Kampel, R. W. Peterson, K. Cicak, R. W. Simmonds, C. A. Regal. Optomechanical Raman-ratio thermometry. Physical Review A, 92, 031802 (2015).

[108] A. Jayich, J. Sankey, K. Børkje, D. Lee, C. Yang, M. Underwood, L. Childress, A. Petrenko, S. Girvin, J. Harris. Cryogenic optomechanics with a Si_3N_4 membrane and classical laser noise. New Journal of Physics, 14, 115018 (2012).

[109] F. M. Buters, M. J. Weaver, H. J. Eerkens, K. Heeck, S. de Man, D. Bouwmeester. Optomechanics with a polarization nondegenerate cavity. Physical Review A, 94, 063813 (2016).

[110] S. Rips, M. Kiffner, I. Wilson-Rae, M. J. Hartmann. Steady-state negative Wigner functions of nonlinear nanomechanical oscillators. New Journal of Physics, 14, 023042 (2012).

[111] M. M. Khan, M. J. Akram, M. Paternostro, F. Saif. Engineering single-phonon number states of a mechanical oscillator via photon subtraction. Physical Review A, 94, 063830 (2016).

[112] C. Galland, N. Sangouard, N. Piro, N. Gisin, T. J. Kippenberg. Heralded single-phonon preparation, storage, and readout in cavity optomechanics. Physical Review Letters, 112, 143602 (2014).

[113] M. Fox: Quantum optics: an introduction, vol. 15, Oxford University Press (2006).

[114] S. Hong, R. Riedinger, I. Marinković, A. Wallucks, S. G. Hofer, R. A. Norte, M. Aspelmeyer, S. Gröblacher. Hanbury Brown and Twiss interferometry of single phonons from an optomechanical resonator. Science, 358, 203–206 (2017).

[115] U. Sterr, T. Legero, T. Kessler, H. Schnatz, G. Grosche, O. Terra, F. Riehle. Ultrastable lasers: new developments and applications. Proceedings of SPIE, 7431, 74310A (2009).

[116] Y. Zhang, K. Hayasaka, K. Kasai. Efficient noise suppression of an amplified diode-laser by optical filtering and resonant optical feedback. Applied Physics B, 86, 643–646 (2007).

[117] J. D. Cohen, S. M. Meenehan, G. S. MacCabe, S. Gröblacher, A. H. Safavi-Naeini, F. Marsili, M. D. Shaw, O. Painter. Phonon counting and intensity interferometry of a nanomechanical resonator. Nature, 520, 522–525 (2015).

[118] M. R. Vanner, M. Aspelmeyer, M. S. Kim. Quantum state orthogonalization and a toolset for quantum optomechanical phonon control. Physical Review Letters, 110, 010504 (2013).

[119] J. Li, S. Gröblacher, S.-Y. Zhu, G. S. Agarwal. Generation and detection of non-Gaussian phonon-added coherent states in optomechanical systems. arXiv:1803.06767 (2018).

[120] Y. Chu, P. Kharel, T. Yoon, L. Frunzio, P. T. Rakich, R. J. Schoelkopf. Climbing the phonon Fock state ladder. arXiv:1804.07426 (2018).

[121] K. J. Satzinger, Y. P. Zhong, H.-S. Chang, G. A. Peairs, A. Bienfait, M.-H. Chou, A. Y. Cleland, C. R. Conner, E. Dumur, J. Grebel, I. Gutierrez, B. H. November, R. G. Povey, S. J. Whiteley, D. D. Awschalom, D. I. Schuster, A. N. Cleland. Quantum control of surface acoustic wave phonons. arXiv:1804.07308 (2018).

[122] M. R. Vanner, I. Pikovski, G. D. Cole, M. S. Kim, Č. Brukner, K. Hammerer, G. J. Milburn, M. Aspelmeyer. Pulsed quantum optomechanics. Proceedings of the National Academy of Sciences, 108, 16182–16187 (2011).

[123] M. R. Vanner, J. Hofer, G. Cole, M. Aspelmeyer. Cooling-by-measurement and mechanical state tomography via pulsed optomechanics. Nature Communications, 4, 2295 (2013).

[124] L.-M. Duan, M. D. Lukin, J. I. Cirac, P. Zoller. Long-distance quantum communication with atomic ensembles and linear optics. Nature, 414, 413–418 (2001).

[125] K. C. Lee, M. R. Sprague, B. J. Sussman, J. Nunn, N. K. Langford, X.-M. Jin, T. Champion, P. Michelberger, K. F. Reim, D. England, D. Jaksch, I. A. Walmsley. Entangling macroscopic diamonds at room temperature. Science, 334, 1253–1256 (2011).

[126] R. Riedinger, A. Wallucks, I. Marinković, C. Löschnauer, M. Aspelmeyer, S. Hong, S. Gröblacher. Remote quantum entanglement between two micromechanical oscillators. Nature, 556, 473–477 (2018).

[127] M. Zugenmaier, K. B. Dideriksen, A. S. Sørensen, B. Albrecht, E. S. Polzik. Long-lived non-classical correlations for scalable quantum repeaters at room temperature. arXiv:1801.03286 (2018).

[128] K. J. Vahala. Optical microcavities. Nature, 424, 839–846 (2003).

[129] A. A. Savchenkov, A. B. Matsko, V. S. Ilchenko, L. Maleki. Optical resonators with ten million finesse. Optics Express, 15, 6768–6773 (2007).

[130] H. Lee, T. Chen, J. Li, K. Y. Yang, S. Jeon, O. Painter, K. J. Vahala. Chemically etched ultrahigh-Q wedge-resonator on a silicon chip. Nature Photonics, 6, 369–373 (2012).

[131] J. Restrepo, J. Gabelli, C. Ciuti, I. Favero. Classical and quantum theory of photothermal cavity cooling of a mechanical oscillator. Comptes Rendus Physique, 12, 860–870 (2011).

[132] K. Usami, A. Naesby, T. Bagci, B. M. Nielsen, J. Liu, S. Stobbe, P. Lodahl, E. S. Polzik. Optical cavity cooling of mechanical modes of a semiconductor nanomembrane. Nature Physics, 8, 168–172 (2012).

[133] H. Okamoto, D. Ito, K. Onomitsu, H. Sanada, H. Gotoh, T. Sogawa, H. Yamaguchi. Vibration amplification, damping, and self-oscillations in micromechanical resonators induced by optomechanical coupling through carrier excitation. Physical Review Letters, 106, 036801 (2011).

[134] C. Xiong, L. Fan, X. Sun, H. X. Tang. Cavity piezooptomechanics: Piezoelectrically excited, optically transduced optomechanical resonators. Applied Physics Letters, 102, 021110 (2013).

[135] H. Okamoto, T. Watanabe, R. Ohta, K. Onomitsu, H. Gotoh, T. Sogawa, H. Yamaguchi. Cavity-less on-chip optomechanics using excitonic transitions in semiconductor heterostructures. Nature Communications, 6, 8478 (2015).

[136] J. Liu, K. Usami, A. Naesby, T. Bagci, E. S. Polzik, P. Lodahl, S. Stobbe. High-Q optomechanical GaAs nanomembranes. Applied Physics Letters, 99, 243102 (2011).

[137] V. Villafañe, P. Sesin, P. Soubelet, S. Anguiano, A. Bruchhausen, G. Rozas, C. G. Carbonell, A. Lemaître, A. Fainstein. Optoelectronic forces with quantum wells for cavity optomechanics in GaAs/AlAs semiconductor microcavities. Physical Review B, 97, 195306 (2018).

[138] C. Metzger, I. Favero, A. Ortlieb, K. Karrai. Optical self cooling of a deformable Fabry-Perot cavity in the classical limit. Physical Review B, 78, 035309 (2008).

[139] L. Midolo, T. Pregnolato, G. Kiršanskė, S. Stobbe. Soft-mask fabrication of gallium arsenide nanomembranes for integrated quantum photonics. Nanotechnology, 26, 484002 (2015).

[140] G. D. Cole, I. Wilson-Rae, K. Werbach, M. R. Vanner, M. Aspelmeyer. Phonon-tunnelling dissipation in mechanical resonators. Nature Communications, 2, 231 (2011).

[141] P. Sparks, C. Swenson. Thermal expansions from 2 to 40°K of Ge, Si, and four III-V compounds. Physical Review, 163, 779 (1967).

[142] S. Adachi: Physical properties of III-V semiconductor compounds, John Wiley & Sons (1992).

[143] H. Okamoto, D. Ito, K. Onomitsu, H. Yamaguchi. Thermoelastic damping in GaAs micromechanical resonators. Physica Status Solidi (c), 5, 2920–2922 (2008).

[144] M. Hamoumi, P. E. Allain, W. Hease, E. Gil-Santos, L. Morgenroth, B. Gérard, A. Lemaître, G. Leo, I. Favero. Microscopic nanomechanical dissipation in gallium arsenide resonators. Physical Review Letters, 120, 223601 (2018).

[145] G. Kiršanskė, P. Tighineanu, R. S. Daveau, J. Miguel-Sánchez, P. Lodahl, S. Stobbe. Observation of the exciton Mott transition in the photoluminescence of coupled quantum wells. Physical Review B, 94, 155438 (2016).

[146] G. Kiršanskė: Electrical control of excitons in semiconductor nanostructures: from quantum dots in photonic-crystal devices to the exciton Mott transition in coupled quantum wells, Ph.D. thesis, University of Copenhagen (2016).

[147] D. A. B. Miller, D. S. Chemla, T. C. Damen, A. C. Gossard, W. Wiegmann, T. H. Wood, C. A. Burrus. Electric field dependence of optical absorption near the band gap of quantum-well structures. Physical Review B, 32, 1043 (1985).

[148] R. S. Daveau, P. Tighineanu, P. Lodahl, S. Stobbe. Optical refrigeration with coupled quantum wells. Optics Express, 23, 25340–25349 (2015).

[149] Z. Vörös, R. Balili, D. Snoke, L. Pfeiffer, K. West. Long-distance diffusion of excitons in double quantum well structures. Physical Review Letters, 94, 226401 (2005).

[150] P. Ruello, V. E. Gusev. Physical mechanisms of coherent acoustic phonons generation by ultrafast laser action. Ultrasonics, 56, 21–35 (2015).

[151] O. Matsuda, T. Tachizaki, T. Fukui, J. J. Baumberg, O. B. Wright. Acoustic phonon generation and detection in GaAs/$Al_{0.3}Ga_{0.7}As$ quantum wells with picosecond laser pulses. Physical Review B, 71, 115330 (2005).

[152] T. Soma, J. Satoh, H. Matsuo. Thermal expansion coefficient of GaAs and InP. Solid State Communications, 42, 889–892 (1982).

[153] V. Negoita, D. W. Snoke, K. Eberl. Huge density-dependent blueshift of indirect excitons in biased coupled quantum wells. Physical Review B, 61, 2779 (2000).

[154] R. Daveau: Decay dynamics and excitonic effects in solid-state quantum emitters, Master's thesis, University of Copenhagen (2013).

[155] M. Gurioli, J. Martinez-Pastor, M. Colocci, C. Deparis, B. Chastaingt, J. Massies. Thermal escape of carriers out of GaAs/$Al_xGa_{1-x}As$ quantum-well structures. Physical Review B, 46, 6922 (1992).

[156] I. Favero, K. Karrai. Optomechanics of deformable optical cavities. Nature Photonics, 3, 201–205 (2009).

[157] L. Greuter, S. Starosielec, D. Najer, A. Ludwig, L. Duempelmann, D. Rohner, R. J. Warburton. A small mode volume tunable microcavity: Development and characterization. Applied Physics Letters, 105, 121105 (2014).

[158] D. Hunger, T. Steinmetz, Y. Colombe, C. Deutsch, T. W. Hänsch, J. Reichel. A fiber Fabry–Perot cavity with high finesse. New Journal of Physics, 12, 065038 (2010).

[159] L. Ding, C. Baker, P. Senellart, A. Lemaitre, S. Ducci, G. Leo, I. Favero. High frequency GaAs nano-optomechanical disk resonator. Physical Review Letters, 105, 263903 (2010).

[160] C. Baker, W. Hease, D.-T. Nguyen, A. Andronico, S. Ducci, G. Leo, I. Favero. Photoelastic coupling in gallium arsenide optomechanical disk resonators. Optics Express, 22, 14072–14086 (2014).

[161] I. Yeo, P.-L. de Assis, A. Gloppe, E. Dupont-Ferrier, P. Verlot, N. S. Malik, E. Dupuy, J. Claudon, J.-M. Gérard, A. Auffèves, G. Nogues, S. Seidelin, J.-P. Poizat, O. Arcizet, M. Richard. Strain-mediated coupling in a quantum dot–mechanical oscillator hybrid system. Nature Nanotechnology, 9, 106–110 (2014).

[162] S. Etaki, M. Poot, I. Mahboob, K. Onomitsu, H. Yamaguchi, H. S. J. Van der Zant. Motion detection of a micromechanical resonator embedded in a d.c. SQUID. Nature Physics, 4, 785–788 (2008).

[163] K. C. Balram, M. I. Davanço, J. D. Song, K. Srinivasan. Coherent coupling between radiofrequency, optical and acoustic waves in piezo-optomechanical circuits. Nature Photonics, 10, 346–352 (2016).

[164] O. Kyriienko, T. C. H. Liew, I. A. Shelykh. Optomechanics with cavity polaritons: dissipative coupling and unconventional bistability. Physical Review Letters, 112, 076402 (2014).

[165] J. Restrepo, C. Ciuti, I. Favero. Single-polariton optomechanics. Physical Review Letters, 112, 013601 (2014).

[166] B.-y. Zhou, G.-x. Li. Ground-state cooling of a nanomechanical resonator via single-polariton optomechanics in a coupled quantum-dot–cavity system. Physical Review A, 94, 033809 (2016).

[167] T. Czerniuk, C. Brüggemann, J. Tepper, S. Brodbeck, C. Schneider, M. Kamp, S. Höfling, B. A. Glavin, D. R. Yakovlev, A. V. Akimov, M. Bayer. Lasing from active optomechanical resonators. Nature Communications, 5, 4038 (2014).

[168] W. Yang, S. A. Gerke, K. W. Ng, Y. Rao, C. Chase, C. J. Chang-Hasnain. Laser optomechanics. Scientific Reports, 5, 13700 (2015).

[169] M. B. Priestley: Spectral analysis and time series, Academic Press (1981).

[170] P. Stoica, R. L. Moses: Spectral analysis of signals, Pearson Prentice Hall Upper Saddle River, New Jersey (2005).

[171] L. D. Landau, E. Lifshitz. Theory of Elasticity, vol. 7. Course of Theoretical Physics, 3, 109 (1986).

[172] A. W. Leissa: Vibration of plates, NASA, Washington (1969).

[173] R. Kubo. The fluctuation-dissipation theorem. Reports on Progress in Physics, 29, 255 (1966).

[174] C. C. Katsidis, D. I. Siapkas. General transfer-matrix method for optical multilayer systems with coherent, partially coherent, and incoherent interference. Applied Optics, 41, 3978–3987 (2002).

[175] D. H. Goldstein: Polarized Light, Revised and Expanded, CRC press (2003).